

Sister Rod Destructive Examinations (FY23)

Appendix F: Cyclic Integrated Reversible- Bending Fatigue Tests

Spent Fuel and Waste Disposition

*Prepared for
US Department of Energy
Spent Fuel and Waste Science
and Technology*

Oak Ridge National Laboratory

*Paul Cantonwine,
Rose Montgomery,
Jy-An Wang, Hong Wang,
Bruce Bevard, Darren Skitt,
Yadukrishnan Sasikumar,
Oscar Martinez*

January 31, 2024

M2SF-24OR010201024
ORNL/SPR-2023/3145

This report was prepared as an account of work sponsored by an agency of the United States Government. Neither the United States Government nor any agency thereof, nor any of their employees, makes any warranty, express or implied, or assumes any legal liability or responsibility for the accuracy, completeness, or usefulness of any information, apparatus, product, or process disclosed, or represents that its use would not infringe privately owned rights. Reference herein to any specific commercial product, process, or service by trade name, trademark, manufacturer, or otherwise, does not necessarily constitute or imply its endorsement, recommendation, or favoring by the United States Government or any agency thereof. The views and opinions of authors expressed herein do not necessarily state or reflect those of the United States Government or any agency thereof.

SUMMARY

This report documents work performed under the Spent Fuel and Waste Disposition's Spent Fuel and Waste Science and Technology program for the US Department of Energy (DOE) Office of Nuclear Energy (NE). This work was performed to fulfill Level 2 Milestone M2SF-24OR010201024, "FY23 ORNL Testing on Sibling Pins," within work package SF-24OR01020102 and is an update to the work reported in M2SF-23OR010201024, M2SF-22OR010201047, M2SF-21OR010201032, M2SF-19OR010201026, and M2SF-19OR010201028.

As a part of the DOE NE High Burnup Spent Fuel Data Project, Oak Ridge National Laboratory (ORNL) is performing destructive examinations (DEs) of high burnup (HBU) (>45 GWd/MTU) spent nuclear fuel (SNF) rods from the North Anna Nuclear Power Station operated by Dominion Energy. The SNF rods, called *sister rods* or *sibling rods*, are all HBU and include four different kinds of fuel rod cladding: standard Zircaloy-4 (Zirc-4), low-tin (LT) Zirc-4, ZIRLO, and M5. The DEs are being conducted to obtain a baseline of the HBU rods' condition before dry storage and are focused on understanding overall SNF rod strength and durability. Composite fuel and defueled cladding will be tested to derive material properties. Although the data generated can be used for multiple purposes, one primary goal for obtaining the post-irradiation examination data and the associated measured mechanical properties is to support SNF dry storage licensing and relicensing activities by (1) addressing identified knowledge gaps and (2) enhancing the technical basis for poststorage transportation, handling, and subsequent disposition.

This appendix documents the status of the ORNL Phase 1 destructive examination (DE) activities related to tests of the sister rods using the Cyclic Integrated Reversible-Bending Fatigue Tester (CIRFT) in Phase 1 of the sister rod test program.

Table FS-1 provides the status of the CIRFT tests.

Table FS-1. DE.05 Status

Planned DE		P.I.	Phase 1 Status	Comments
DE.05	Perform CIRFT tests to determine static, dynamic, and cumulative effects and fatigue lifetime	Cantonwine	Complete	<p>Thirty-five tests using the CIRFT were completed on 29 specimens. The results are consistent with those for other rods of the same type that were tested in the past, but they fall on the lower side of the database, especially the rods with Zirc-4 and LT Zirc-4 cladding and the samples tested at nonzero mean strain. One dynamic test was removed from the fatigue database because closer examination of the data showed that it failed during the preceding static test. The heat treatments applied to selected rods resulted in a shorter fatigue lifetime, which is suspected to be related to their observed reduced flexural rigidity.</p> <p>The flexural rigidity measured for the baseline sister rods is consistent with (although on the lower side of) previously tested 17×17 specimens for M5-, ZIRLO-,</p>

Planned DE		P.I.	Phase 1 Status	Comments
				<p>and LT Zirc-4 clad specimens. Because of the large uncertainties in the tests at low applied moment and because all the samples at high applied moment were tested statically before dynamic testing, only the samples tested at applied moments between 8 and 14 N-m are used in calculating the average dynamic flexural rigidity, which is 27 N-m².</p> <p>A test on a specimen with a grid-to-rod-fretting mark in the maximum strain location did not result in a reduced fatigue lifetime.</p>
	Comparison of fueled segment CIRFT performance with cladding-only data and O-Donnell Langer historical data	Cantonwine	Complete	<p>CIRFT results were compared with open literature fatigue data on zirconium alloys (specifically Zircaloy-2 and Zirc-4) that used other unfueled material geometries. To determine whether the open literature data are representative of empty cladding and/or fueled rod geometry, a verification study is being performed using CIRFT and unirradiated and irradiated cladding specimens. To date, five CIRFT tests have been performed on unirradiated Zirc-4 tubes for comparison with fuel rod segment and open literature data for alloy tubes and coupons. It was found that the fatigue of the high burnup fuel rods is degraded compared with the cladding-only tube and other specimens described in open literature on zirconium alloys. It is also noted that testing to date is under zero-mean strain conditions, which is likely nonconservative relative to the expected condition of the fuel rod, which includes axial strain from rod internal pressure and bending under gravity. A proposed ORNL Fuel Rod fatigue design limit is compared with the data in hand. Additional testing to quantify the impact of a nonzero mean strain was completed and found to be very close to the ORNL Fuel Rod Design Limit. Testing at nonzero mean strain caused a 40% degradation of the fatigue performance relative to the best estimate correlation.</p>

Planned DE		P.I.	Phase 1 Status	Comments
	Posttest imaging and dogbone characterization	Skitt	Complete	All completed test pairs have been characterized.
	Post-test scanning electron microscope (SEM) characterization of fracture surface	Sasikumar	Complete	A sample preparation procedure was developed, and the fracture surfaces of two failed fuel rods and two failed Zirc-4 tubes have been characterized. Features consistent with fatigue were observed, and the indications are that fatigue failure initiated on the inner diameter (ID) in both the fuel segments and the cladding-only tube samples. It is most likely that the stress concentrations at pellet discontinuities are the source of the ID cracks that initiated fatigue failure in the fuel segments, but ID surface damage was created during testing of unirradiated cladding tubes that caused the initiation of fatigue failures. Initiation on the ID of the cladding tubes was unexpected because the maximum strain is on the outer diameter. Future SEM characterization is planned to explore whether hydride formation is a factor in fatigue initiation.
	Finite element modeling of selected performance characteristics	Martinez	Complete	Modeling of the cumulative impact test to determine the appropriate fixture configuration is complete and indicates that applying an impact to a specimen mounted in a dogbone will yield an impact load that is higher than desired. However, the evaluation of the multimodal transportation test results suggests that cladding strains that occur in a coupling impact event (the event with the largest observed accelerations during shipping) were still well below the ORNL Fuel Rod Design Fatigue Limit, though the effect of nonzero mean strain on the ORNL Fatigue Limit has not been fully considered. Because of these results, no further work is needed.

This page intentionally blank

ACKNOWLEDGMENTS

Many thanks to our US Department of Energy Office of Nuclear Energy sponsor Ned Larson, along with the Spent Fuel and Waste Science and Technology Storage and Transportation Program leadership for their continued support. The sister rod project would not have been possible without the vision and support of the Electric Power Research Institute, Westinghouse, Framatome, and Dominion Energy. We also thank the US Nuclear Regulatory Commission for their vision and support developing the fatigue testing system.

This work would not have been possible without the support and expertise provided by the leadership and staff members of Oak Ridge National Laboratory's Irradiated Fuel Examination Laboratory. Special thanks go to Scott Thurman, who built the dogbones in-cell, tracked the specimens and the tests, and helped perform the testing, and to Bryan Woody and John Hinds for their assistance with in-cell testing activities. Ricardo Muse supported the fabrication jobs associated with the cyclic integrated reversible-bending fatigue tester tests, and we appreciate his continued support. Many thanks to Tracie Lowe for her work on the scanning electron microscope imaging included in this report.

This page intentionally blank

CONTENTS

SUMMARY	iii
ACKNOWLEDGMENTS	vii
CONTENTS.....	ix
LIST OF FIGURES	xi
LIST OF TABLES.....	xv
REVISION HISTORY.....	xvii
ACRONYMS.....	xix
F-1. Introduction	1
F-2. CIRFT Description	1
F-3. Data Acquisition, Data Processing, Basic Information, and Extended Information	4
F-3.1 Basic Calculated Information.....	7
F-3.2 Extended Calculated Information within the Context of CIRFT	7
F-3.2.1 Pellet Bonding Stiffening.....	8
F-3.2.2 Discontinuous Cladding Support	8
F-3.2.3 Cladding Hydride Reorientation Effects.....	9
F-3.2.4 Cladding Irradiation Defect Annealing.....	9
F-3.2.5 Normal Condition Impacts.....	9
F-4. Comparison Data Available from Previous ORNL Tests of Irradiated Rod Segments.....	11
F-5. Comparison Data from Cladding Tests	13
F-5.1 Unirradiated Zirc-4 Cladding Tests	13
F-5.1.1 Calibration Sample (Zr4-W-2).....	14
F-5.1.2 High Cycle Fatigue Response.....	17
F-6. Description of the Sister Rods Tested	19
F-7. Selection of CIRFT Test Conditions	27
F-8. CIRFT Test Results for the Sister Rods Tested.....	30
F-8.1 Static Tests	30
F-8.2 Dynamic Tests.....	32
F-8.2.1 Uncertainty in Strain Amplitude and Flexural Rigidity	32
F-8.2.2 Comparisons Based on Stress Amplitude	33
F-8.2.3 Comparisons Based on Strain Amplitude	33
F-8.2.4 CIRFT-Measured Flexural Rigidity of HBU Fuel Rods	34
F-8.3 Comparisons of Paired Specimens.....	46
F-8.4 Optical Imaging of the Fractured Specimens.....	48
F-8.5 Scanning Electron Microscope Characterization of Selected CIRFT Fractures	74
F-8.5.1 Sample preparation	74
F-8.5.2 Characterization of Fracture in ZIRLO- 17 × 17	75
F-8.5.3 Characterization of Fracture in LT Zirc-4 Fuel Rods	79
F-8.5.4 Fractography of unirradiated Zirc-4 CIRFT specimens.....	83
F-8.5.4.1 Zr4-W-4.....	83

F-8.5.4.2	Zr4-W-3	88
F-8.5.5	Future work	93
F-9.	CIRFT Cumulative Effects Fixture Development	94
F-9.1	Finite Element Modeling of the Cumulative Impactor	95
F-9.1.1	Finite Element Modeling Software	95
F-9.1.2	Finite Element Model	96
F-9.1.3	Material Models	97
F-9.1.4	Initial Conditions, Boundary Conditions, and Load Cases	98
F-9.1.5	Load Cases	98
F-9.2	Results, Discussion, and Conclusions from the Cumulative Effects Fixture Modeling	99
F-9.3	Verification of FEA Results Using the Cumulative Effects Fixture	102
F-9.4	Implication of the Multimodal Transportation Test	103
F-9.5	Summary, Cumulative Effects Fixture Development	103
REFERENCES	104

LIST OF FIGURES

Figure F-1. Two views of the ORNL CIRFT: (a) a surrogate rod specimen undergoing out-of-cell testing with three linear variable differential transducers for curvature measurements and (b) an SNF rod being tested in the hot cell.	2
Figure F-2. Schematic drawings of U-frame setup for reversal bending when rigid arms are (a) closing, (b) neutral, and (c) opening.	3
Figure F-3. Image showing the grip design of CIRFT with one end-block removed.	4
Figure F-4. LVDT measurements for the curvature calculation.	5
Figure F-5. Example of a single cycle from two low-cycle (0.05 Hz) tests used for equipment performance confirmation showing (a) the instantaneous applied bending moment, (b) the calculated curvature, and (c) the moment-curvature hysteresis loop. The example is also representative of the type of data collected in the fatigue performance portion of the test session.	6
Figure F-6. Cladding and pellet stack (a) in the neutral position and (b) in bending. [F-5]	8
Figure F-7. Results for Strain Gauge Sample Zr4-W-2.	15
Figure F-8. CIRFT results of unirradiated Zirc-4 tubes compared with previously reported data on both unirradiated and irradiated Zirc-2 [F-8] and unirradiated Zirc-4 [F-9],[F-10].	18
Figure F-9. Static test data for 30AD05-0697-0850 represent the typical result.	30
Figure F-10. Results of CIRFT tests plotted with reference data, applied moment vs. cycles to failure.	38
Figure F-11. Results of CIRFT tests completed to date, strain amplitude vs. cycles to failure.	39
Figure F-12. Stress amplitude of the composite rod based on Eq. (F-7) as a function of cycles to failure for the sister rods.	40
Figure F-13. Cladding stress amplitude as a function of cycles to failure for the sister rods.	41
Figure F-14. Strain amplitude as a function of cycles to failure for the sister rods compared with the fatigue data on cladding alloys from Figure F-7 and the proposed ORNL fatigue limit for fuel rods. [F-12]	42
Figure F-15. The fraction of the residual to the predicted strain amplitude for the zero mean strain fatigue data as a function of the oxide thickness estimated from the liftoff measurement in Montgomery et al. [F-11].	43
Figure F-16. CIRFT-measured flexural rigidity of the sister rod segments tested as a function of estimated segment burnup plotted with previous CIRFT data.	44
Figure F-17. Trend of CIRFT-measured dynamic flexural rigidity with applied bending moment.	45
Figure F-18. 6U3K09-3353-3506 postfatigue test condition.	50
Figure F-19. 6U3K09-2310-2463 postfatigue test condition.	51
Figure F-20. 6U3K09-3200-3353 postfatigue test condition.	52
Figure F-21. 6U3K09-2635-2788 postfatigue test condition.	53
Figure F-22. 6U3K09-2463-2616 postfatigue test condition.	54
Figure F-23. 3F9N05-2710-2863 postfatigue test condition.	55

Figure F-24. 3F9N05-2329-2482 postfatigue test condition.....	56
Figure F-25. 3F9N05-0719-0872 postfatigue test condition.....	57
Figure F-26. 3D8E14-2963-3116 postfatigue test condition.	58
Figure F-27. 30AD05-2630-2783 postfatigue test condition.....	59
Figure F-28. 30AE14-0672-0825 postfatigue test condition.	60
Figure F-29. F35P17-1855-2008 postfatigue test condition.	61
Figure F-30. F35P17-3159-3312 postfatigue test condition.	62
Figure F-31. 3A1F05-2025-2178 postfatigue test condition.....	63
Figure F-32. 3A1F05-1853-2006 postfatigue test condition.....	64
Figure F-33. 30AD05-0697-0850 postfatigue test condition (broken ends only).....	65
Figure F-34. 30AD05-2050-2203 postfatigue test condition (broken ends only).....	66
Figure F-35. 30AE14-2850-3003 postfatigue test condition (broken ends only).	67
Figure F-36. 30AE14-3156-3309 postfatigue test condition (broken ends only).	68
Figure F-37. 3A1F05-3214-3367 postfatigue test condition.....	69
Figure F-38. 3D8E14-719-872 postfatigue test condition.	70
Figure F-39. 3D8E14-2412-2565 postfatigue test condition.	71
Figure F-40. 3A1F05-3367-3520 postfatigue test condition.....	72
Figure F-41. 3D8E14-1178-1331 postfatigue test condition.	73
Figure F-42. Montage (23×) of the surface of the fatigue failure in sample 3D8E14-2963-3116.....	76
Figure F-43. Images at 330× and 1,000× of quadrant 1 in sample 3D8E14-2963-3116.	77
Figure F-44. Images at 100× and 1,000× of quadrant 3 in sample 3D8E14-2963-3116, ~180° from region in quadrant 1 that is suspected to have failed after fatigue test ended.....	77
Figure F-45. Images at 120× and 500× of quadrant 2 in sample 3D8E14-2963-3116, showing signs of fatigue striations typical of fatigue crack propagation, indicating propagation in the circumferential direction.	78
Figure F-46. Images at 120× and 350× of quadrant 4 in sample 3D8E14-2963-3116 showing signs of fatigue striations typical of fatigue crack propagation.	78
Figure F-47. Montage (100x) of the surface of the fatigue failure in dogbone sample DE50017.....	80
Figure F-48. Ductile regions and wear marks of Q1 in sample 3A1F05-2025-2178.....	81
Figure F-49. Fuel-side brittle regions of Q1 (approaching Q2) in sample 3A1F05-2025-2178.....	81
Figure F-50. Cleavage-like regions, apparent fatigue striations, and flat wear marks on the fuel side of Q2 in sample 3A1F05-2025-2178.....	82
Figure F-51. Ductile fracture regions amidst striations and brittle cracks on Q3 in sample 3A1F05- 2025-2178.....	82
Figure F-52. Flat cleavage-like regions on the fuel side leading to cracks and ductile failure seen on Q4 in sample 3A1F05-2025-2178.	83

Figure F-53. Montage (100×) of the surface of the fatigue failure in dogbone sample Zirc-4-W-4.....	84
Figure F-54. Top (fracture) view and side view of the fatigue failure region in Q2 and Q3 of sample Zirc-4-W-4.....	85
Figure F-55. Fatigue crack initiation region in Q4 of sample Zirc-4-W-4: (A) location of the region in a low-magnification image of the sample, (B) OD side of the fatigue failure initiation site, (C) ID side of the fatigue crack initiation site, and (D) detailed view of C.	85
Figure F-56. Tilted image of Figure F-54 revealing the ID side of the fatigue failure initiation site on sample Zirc-4-W-4: (A) location of the region in a low-magnification image of the sample, (B) ID side of the fatigue failure initiation site, and (C) detailed view of the fatigue failure initiation fracture surface.	86
Figure F-57. Brittle fracture regions and potential wear marks of sample Zirc-4-W-4: (A) location of the region in a low-magnification image of the sample, (B) brittle or cleavage-like regions on Q1, and (C) potential wear marks observed between the brittle regions in Q1.	87
Figure F-58. Montage (100x) of the fatigue failure surface in dogbone sample Zirc-4-W-3.	89
Figure F-59. The top (fracture) view and side view of the fatigue failure region in Q2 and Q3 of sample Zirc-4-W-3.	90
Figure F-60. Fatigue crack initiation region in Q4 of sample Zirc-4-W-3: (A) location of the region in a low-magnification image of the sample, (B) ID side of the fatigue crack initiation site, and (C) detailed view of B.	91
Figure F-61. Optical microscopic image of sample Zirc-4-W-3 showing the fatigue failure initiation site; the peripheral region containing the LVDT marks is not visible.....	91
Figure F-62. Tilted SEM image of Figure F-60 revealing the ID side of the fatigue failure initiation site of sample Zirc-4-W-3: (A) location of the region in a low-magnification image of the sample, (B) OD side of the fatigue failure initiation site, (C) ID side of the fatigue initiation site, and (D) inside of the ID side of sample Zirc-4-W-3 at the fatigue initiation site.	92
Figure F-63. Some striations visible amidst brittle or cleavage fracture-like regions and wear marks of sample Zirc-4-W-3: (A) location of the region in a wide field view of the sample, (B) wear marks observed on the ID with striations on the OD and brittle fracture regions in the middle of Q1, and (C) detailed view of the flat wear-like features between striations.	92
Figure F-64. Fatigue failure in sample 6U3K09-2310-2463 showing the second crack observed in the sample.	93
Figure F-65. Images of the circumferential cut-2 from sample 6U3K09-2310-2463 wrapped around a 3D cylinder to show a realistic image.....	93
Figure F-66. Cumulative shock fixture developed to apply a normal transport condition shock before fatigue testing.	94
Figure F-67. The cumulative impactor CAD model (left) and finite element model (right) include a rod segment with discrete pellets, guide blocks, and a weight with impact geometry.	96
Figure F-68. 304 stainless steel (left) and Zirc-4 (right) true stress-strain curves used compared with corresponding engineering stress-strain curves.....	98
Figure F-69. Impactor end configuration (a) results for g-load cases 1–4.....	99

Figure F-70. Impactor end configuration (a) results for load cases 5–9.	100
Figure F-71. Plastic strain on the dimples for impactor end configuration (a).	101
Figure F-72. CIRFT dogbone.....	101
Figure F-73. Physical test configurations with the cumulative effects fixture.....	102
Figure F-74. Impactors used in the physical tests.	102

LIST OF TABLES

Table FS-1. DE.05 Status.....	iii
Table F-1. Reference Dynamic Dataset [F-4].....	11
Table F-2. Test Conditions for Strain-Gauged Test Sample (Zr4-W-2).....	13
Table F-3. Test Conditions for Fatigue Tests on Cladding-Only Zirc-4 Tubes (no strain gauges)	14
Table F-4. Dynamic Correction Factor as a Function of the Strain Gauge Strain Amplitude for Testing at 0.05 and 5 Hz.....	15
Table F-5. Curvature, Strain Amplitude, Applied Moment, and Cycles to Failure for the Unirradiated Zirc-4 Cladding Tubes.....	17
Table F-6. Maximum Average Stress, Maximum Stress, Dynamic Flexural Rigidity, and Rigidity Standard Deviation for the Unirradiated Zirc-4 Cladding Tubes	18
Table F-7. Sister Rod Segments Selected for CIRFT	20
Table F-8. CIRFT Specimen and Test Pairing.....	28
Table F-9. Non-zero Mean Strain Dynamic Test Conditions	29
Table F-10. Static Test Results	31
Table F-11. Sister Rod CIRFT Test Results at Zero Mean Strain	35
Table F-12. Sister Rod CIRFT Test Results at Non-zero Mean Strain.....	36
Table F-13. Strain Amplitude and Flexural Rigidity with Test and Measurement Variability Used to Calculate Uncertainty.....	37
Table F-14. Results Arranged by Paired Specimens (Baseline Rods vs. Heat-Treated Rods) for Static/Dynamic and Dynamic CIRFT.....	47
Table F-15. Summary of Visual Observations of CIRFT-Fractured Dogbones	49
Table F-16. CIRFT Specimens Identified for Potential SEM Characterization	74
Table F-17. Cumulative Impactor Model Minimum Material Properties.....	97
Table F-18. Cumulative Tester FEA Load Case Summary	98
Table F-19. Summary of Fuel Rod Maximum g-Load During Impact with End Configuration (a).....	100

This page is intentionally left blank.

REVISION HISTORY

Date	Changes
3/29/2019	Initial release
9/27/2019	Revised to include additional data and incorporate comments from the previously released report.
10/29/2020	The CIRFT detailed report was moved to Appendix F and was updated to include the most recent information.
11/30/2020	Comments received on the draft were incorporated, and the document numbering was revised to reflect its M2 status.
10/29/21	Section F-7.6 was added. The results of the uncertainty estimates (Appendix G) were integrated into the data table and plots, and related discussions were modified. One low data point was investigated and removed from the CIRFT dataset, and the supporting information was added to the report (Section F-7.1). Minor clarifications have been made throughout.
3/31/22	Minor formatting changes and clarifications were made in response to comments received on the 10/29/21 report (Section F-2 paragraph 4, Section F-3 paragraph 1, Figure F-5 caption, addition of reference F-19). The document ID number was revised to reflect its M2 status and the issue date was changed.
10/28/22	Sections F-5 and F-8.5 were added. The Summary section and Table FS-1 was updated. Two references were added. Section F-8.2 was revised and incorporates a new section, F-8.2.2, to reflect our most up-to-date understanding of the data, and Figure F-14 was added.
1/13/2023	Comments received from the team were incorporated throughout, document ID number was revised to reflect its M2 status, and the issue date was changed.
10/31/2023	Added results of nonzero mean strain testing; updated the uncertainties in the strain amplitudes and flexural rigidities to reflect more recent evaluations; and added a discussion on why impact loads during transportation are not expected to cause fatigue damage.
1/31/2024	Comments from the Sister Rod review team were incorporated. The document ID # was changed to reflect its M2 status, and the date was changed.

This page is intentionally left blank.

ACRONYMS

ASME	American Society of Mechanical Engineers
BWR	boiling water reactor
CIRFT	cyclic integrated reversible-bending fatigue tester
DE	destructive examination
DOE	US Department of Energy
FEA	finite element analysis
FHT	full-length fuel rod heat treatment
GTRF	grid-to-rod fretting
HBU	high burnup
ID	inner diameter
LSTC	Livermore Software Technology Corporation
LT	low tin
LVDT	linear variable differential transducers
MMTT	multimodal transportation test
NDE	nondestructive examination
NE	Office of Nuclear Energy
NRC	US Nuclear Regulatory Commission
OD	outer diameter
ORNL	Oak Ridge National Laboratory
PWR	pressurized water reactor
SEM	scanning electron microscope
SNF	spent nuclear fuel

This page is intentionally left blank.

F-1. Introduction

Spent nuclear fuel (SNF) assemblies must be shipped to other sites for processing and disposal. During shipment, the fuel is typically oriented horizontally, and the fuel rods are subject to periodic alternating loads related to the movement of the vehicle that results in alternating bending of the SNF fuel rods. The number of bending cycles is related to the length of the shipping route, with longer routes producing more cycles. Because it is well-known that cyclic loads can produce failures, even when the stress and strain imposed are below the material's yield point, investigation of the SNF's fatigue behavior is prudent.

This report discusses the results of fatigue testing conducted at Oak Ridge National Laboratory (ORNL) using the Cyclic Integrated Reversible-Bending Fatigue Tester (CIRFT) created by the US Department of Energy Office of Nuclear Energy for the High Burnup Spent Fuel Data Project and its sister rods [F-1, F-2, F-3]. The results of the tests are compared with results obtained over the last decade using the same CIRFT for the US Nuclear Regulatory Commission (NRC).

F-2. CIRFT Description

The CIRFT, shown in Figure F-1, is hardware developed by ORNL [F-4, F-5] to test the fatigue lifetime of SNF in postulated normal transportation vibration conditions. The machine oscillates 6 in. segments of high burnup (HBU) SNF until fatigue failure occurs. The CIRFT uses a U-frame with two rigid arms that convert the motor's linear motion into a bending moment exerted on the rod segment. The two U-frame arms are driven by two electromagnetic-force-based motors. The motors (Bose model LM2) have a maximum load capacity of $\pm 3,000$ N and a maximum stroke of ± 25.6 mm.

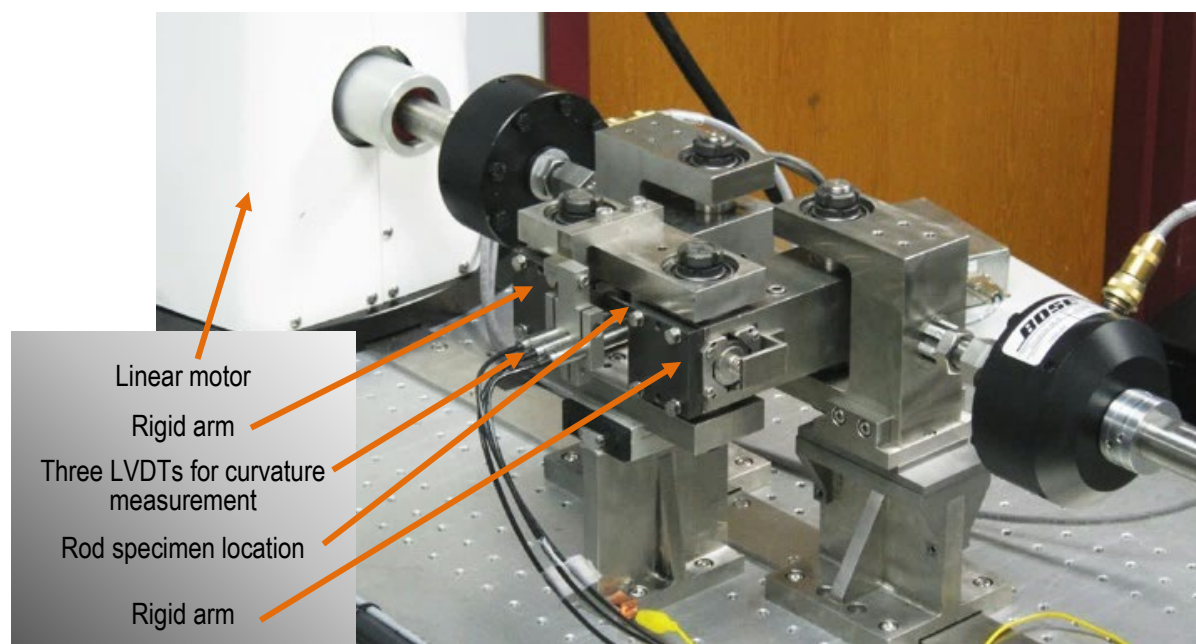
Each tested SNF segment is fitted with special end grips, or *dogbones*, which are epoxied onto both ends of the segment. When prepared this way, the SNF segment is referred to as a *dogbone*. The epoxy provides a compliant layer that is important for ensuring pure bending. The epoxy layer thickness depends on the as-built diameter of dogbone recesses and segment outer diameter. This layer is important for ensuring pure bending. When the dogbone is engaged with the U-frame, bending is imposed by the motor through the U-frame, as illustrated in Figure F-2, with a cycle that progresses as follows: the dogbone (1) begins in the neutral position (i.e., no bending), (2) is flexed laterally away from the front face of the machine, (3) is returned to the neutral position, (4) is flexed laterally toward the front face of the machine, and (5) is returned to the neutral position. The CIRFT can flex the rod specimen at 5–10 Hz during the dynamic test, with the sister rod tests performed at 5 Hz.

To ensure the desired motion, the CIRFT is specifically configured to test SNF rod segments that have diameters ranging from 9.70 to 11.74 mm, with a fixed segment length of 152.40 mm (6 in.). The test's gauge section is the 50.80 mm (2 in.) SNF rod length between the dogbones, where the maximum bending deflection occurs.

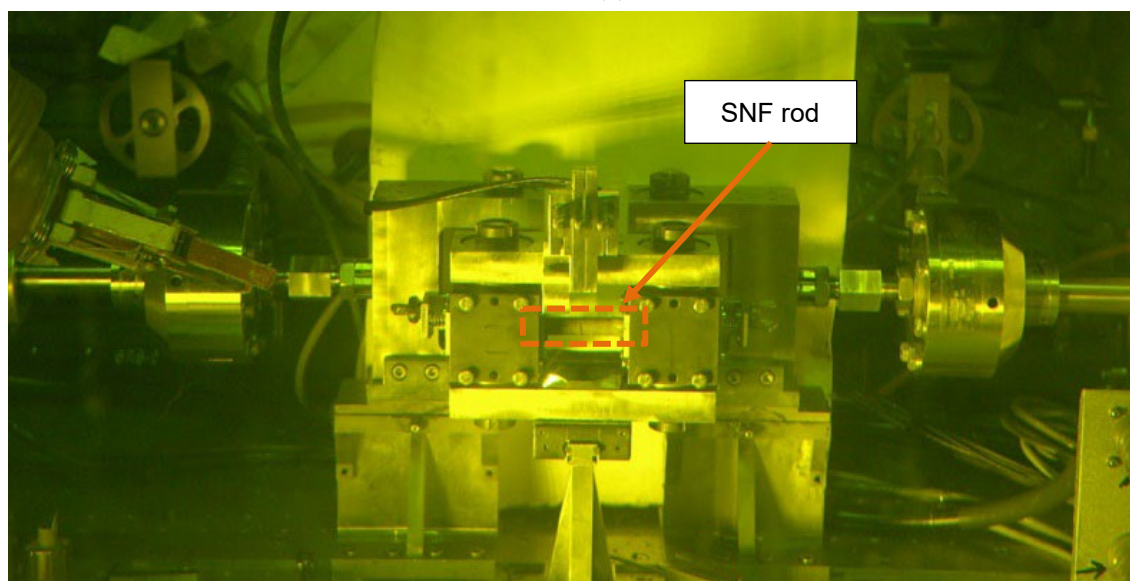
To date, two types of tests have been performed: a *static* test and a *dynamic test*. A third test, the *cumulative effects* test, is still in the equipment development stage. The dynamic test is the standard fatigue test performed on the CIRFT. Dynamic testing is performed in a series of sessions, where a session consists of two displacement-controlled cyclic tests performed at 0.05 Hz for a low number of cycles at loads less than the 5 Hz fatigue test (to confirm equipment performance) and a load-controlled cyclic test at 5 Hz (to test fatigue performance). The number of sessions in a complete dynamic test is dependent on the cycles to failure and varies from 1 session (for low-cycle fatigue conditions) to as many as 7 sessions (for high-cycle fatigue conditions). During the dynamic test, the SNF segment is flexed at a fixed frequency and motor stroke length. For the static test, the segment is flexed slowly to the maximum stroke of the machine and the deflection of the SNF specimen is measured. The static test does not typically result in fracture of the specimen because the largest possible machine stroke usually cannot impose enough deflection on the SNF specimen to exceed the cladding tensile strength and cause a non-fatigue fracture. Although the static test

January 31, 2024

can be followed by a dynamic test, the flexure imposed during the static test is much higher than that imposed during the dynamic test, and the large deflection might reduce the flexural rigidity and fatigue lifetime, even without fracture of the SNF segment, as discussed in later sections of this appendix. The cumulative test will impose impacts on the SNF segment before a dynamic test is performed; the cumulative test is meant to determine whether periodic impacts of the rod with other rods or the packaging during transport are detrimental to the fatigue lifetime.

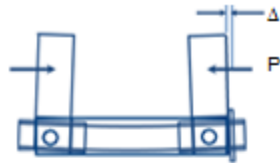


(a)

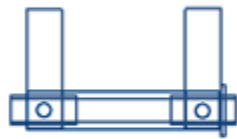


(b)

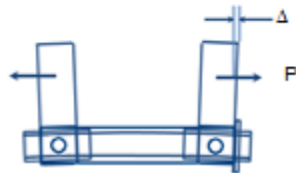
Figure F-1. Two views of the ORNL CIRFT: (a) a surrogate rod specimen undergoing out-of-cell testing with three linear variable differential transducers for curvature measurements and (b) an SNF rod being tested in the hot cell.



(a) Rigid arms are closing. The curvature is concave outward and designated with a negative sign.



(b) Rigid arms are in neutral position.



(c) Rigid arms are opening. The curvature concave inward and designated with a positive sign.

Figure F-2. Schematic drawings of U-frame setup for reversal bending when rigid arms are (a) closing, (b) neutral, and (c) opening.

F-3. Data Acquisition, Data Processing, Basic Information, and Extended Information

This section summarizes the full discussion provided by Wang and Wang [F-4, F-5, F-6]. The key data acquired during the CIRFT test include the number of cycles to failure and the bending moment imposed. The bending moment is calculated based on the motor stroke length applied (set by the user) and the deflection of the SNF rod segment, which is measured using three linear variable differential transducers (LVDTs), as shown in Figure F-3. A view of one end of a test specimen is shown in Figure F-3 with the end-block removed, allowing a view of the LVDTs. Online monitoring of the calculated flexural rigidity is used to shut down the machine at the onset of failure.

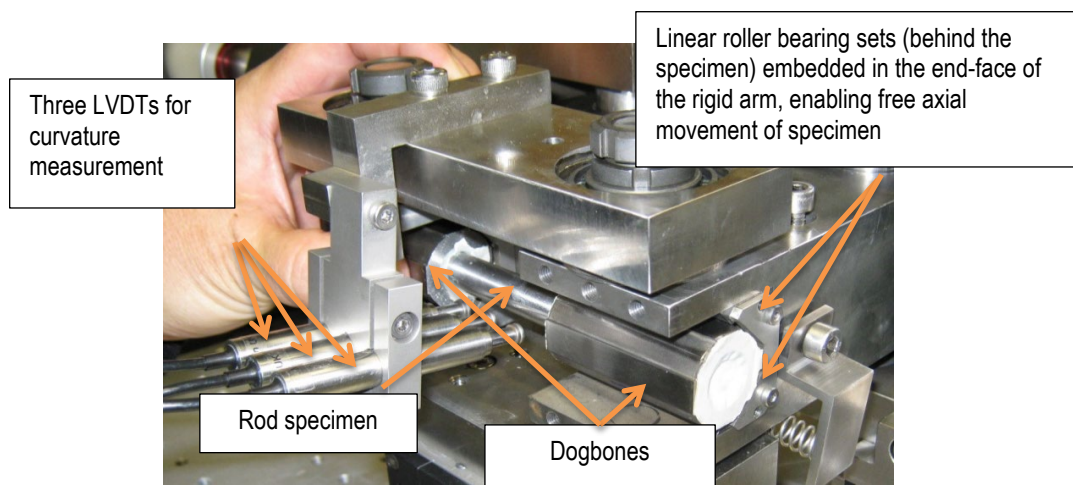


Figure F-3. Image showing the grip design of CIRFT with one end-block removed.

The distances built into the CIRFT machine and the length of the segment dogbone are important because they are used to calculate all load, moment, and curvature values. Important fixed physical distances include the length of the U-frame arms (101.60 mm) and the location and contact geometry of the LVDTs. Also, the motor's recorded stroke length during the test is directly applied in the data reduction, and the SNF rod outer diameter (OD) is used to calculate strain and stress.

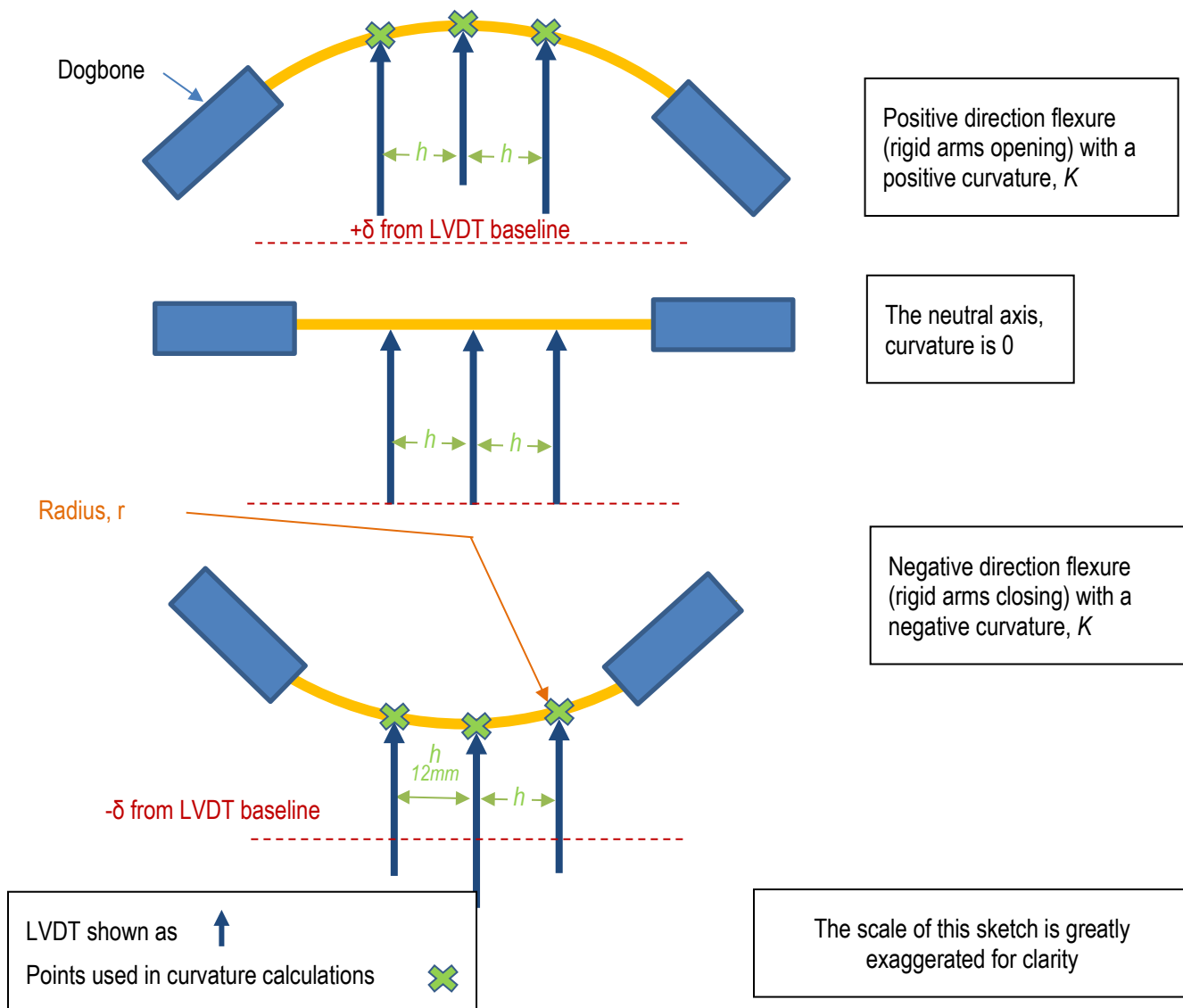


Figure F-4. LVDT measurements for the curvature calculation.

The rod curvature, K , is calculated as the inverse of the radius, assuming the SNF segment forms a short circular arc. As illustrated in Figure F-4, the known spacing between the LVDTs (h , 12 mm) is used with the measured LVDT deflection to determine the instantaneous curvature of the dogbone gauge section during the test. The raw data are denoised and further adjusted based on the type of LVDT used in the test and any bias observed in the LVDT measurements. An example of the processed data is provided in Figure F-5.

January 31, 2024

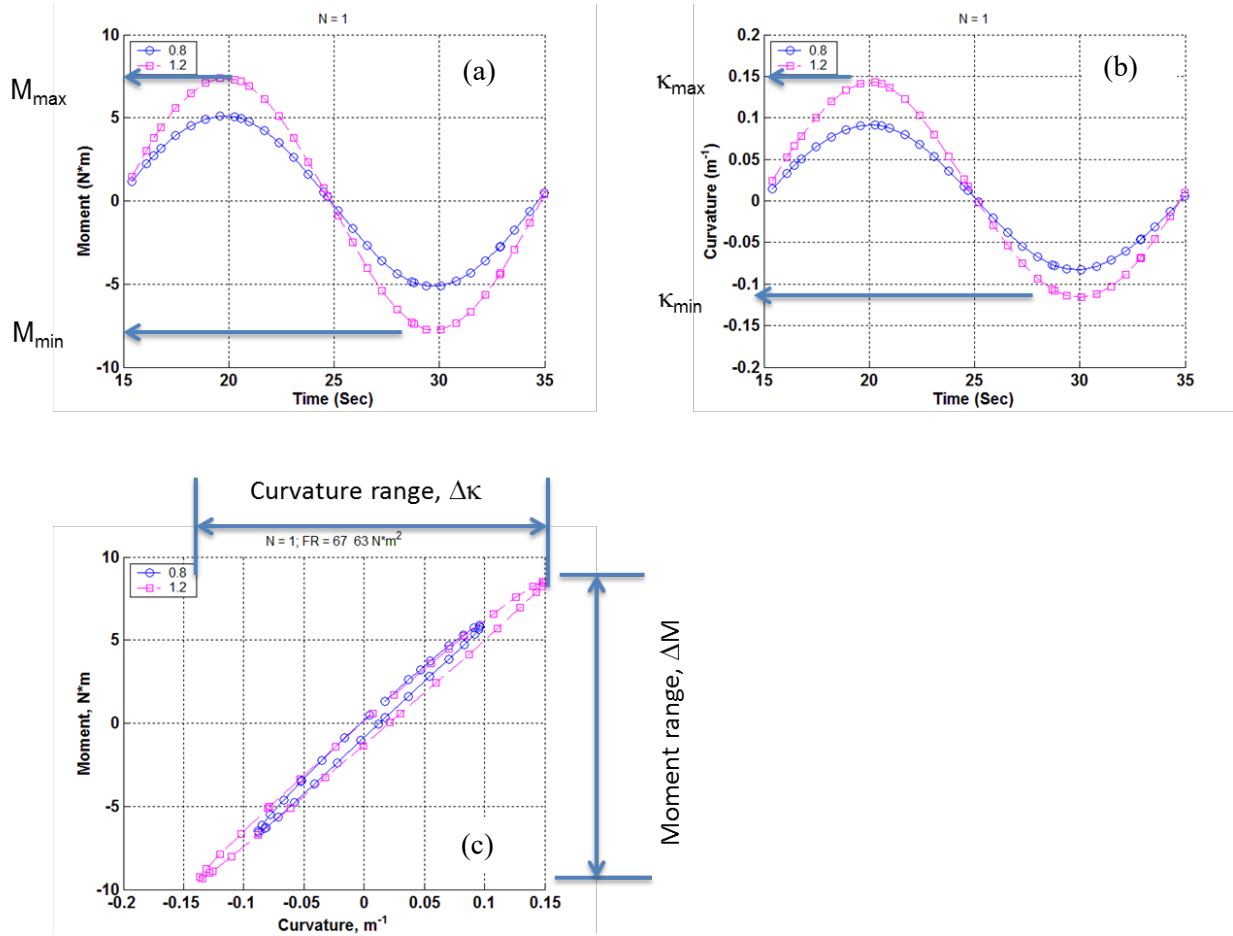


Figure F-5. Example of a single cycle from two low-cycle (0.05 Hz) tests used for equipment performance confirmation showing (a) the instantaneous applied bending moment, (b) the calculated curvature, and (c) the moment-curvature hysteresis loop. The example is also representative of the type of data collected in the fatigue performance portion of the test session.

The radius, r , is calculated by determining the physical coordinates described by the measured LVDT deflections d_1 , d_2 , and d_3 and by scribing them with a circle:

$$\sqrt{(x_0 - d_2)^2 + y_0^2} , \quad (\text{F-1})$$

where

$$x_0 = \frac{-2m_a m_b h - m_a(d_2 + d_3) + m_b(d_1 + d_2)}{2(m_b - m_a)} , \quad (\text{F-2})$$

and

$$y_0 = -\frac{1}{m_a} \left(x_0 - \frac{d_1 + d_2}{2} \right) - \frac{h}{2} , \quad (\text{F-3})$$

where
$$m_a = \frac{h}{d_2 - d_1} \text{ and } m_b = \frac{h}{d_3 - d_2} , \quad (\text{F-4})$$

and h is the sensor distance fixed at 12 mm.

Corrections are made to the LVDT data (d_1 , d_2 , d_3 , and h) as described in the work by Wang and Wang [F-4].

F-3.1 Basic Calculated Information

To provide a basis for comparing the performance of different fuel rod designs, it is necessary to calculate additional parameters such as stress and strain, and they are typically discussed in terms of their maximum amplitude for CIRFT. It is also useful to survey the flexural rigidity, which tends to decrease as the test progresses. Typically, the flexural rigidity at the beginning of the test is discussed as a comparison point among rod types. The strain and stress parameters are calculated based on standard formulae for a circular beam in bending.

The maximum gauge strain, which occurs at the maximum deflections in the cycle and at the outermost radius of the rod, is calculated as the curvature multiplied by the radius of the rod, which is the maximum distance from the neutral axis, y_{max} :

$$\varepsilon = \kappa \times y_{max} . \quad (\text{F-5})$$

The average moment applied to the rod is

$$M = F \times L , \quad (\text{F-6})$$

where F is the averaged value of the load applied at the time span of interest (typically 0.001 s in the dynamic test) by the CIRFT motors, and L is the fixed U-frame loading arm length (101.60 mm).

The maximum rod stress is calculated as

$$\sigma = M \times y_{max} / I , \quad (\text{F-7})$$

where I is the area moment of inertia of the composite SNF rod calculated based on the geometry of cladding and solid pellet section.

The flexural rigidity, EI , provides a means to generate the stress-strain relationship associated with M- κ . The average calculated bending moment (ΔM) and average measured curvature ($\Delta \kappa$) are used to characterize the average flexural rigidity over the time span of interest:

$$EI = \Delta M / \Delta \kappa . \quad (\text{F-8})$$

F-3.2 Extended Calculated Information within the Context of CIRFT

In addition to the basic information discussed in Section F-3.1, other parameters of interest are developed to study the effect of particular rod characteristics on the fatigue.

SNF fuel rods are heterogeneous. Although the geometry of the irradiated rod can be estimated, it varies based on rod type, manufacture, and operation. The irradiated rod contains cracked pellets (some with HBU rims), an inner cladding oxide layer, potentially a layer of pellet bonded with the cladding inner diameter (ID), cladding with radiation-induced flaws, and an outer cladding oxide layer that is potentially discontinuous because of spalling. Axially, the fuel column is not continuous; it is composed of numerous short pellets. Although there could be some bonding between pellet ends as a result of an in-reactor diffusion bonding or galling process, the contacting surface areas are small as a result of the pellet chamfers and

January 31, 2024

dishes, and the pellet-pellet bonding is not expected to be strong. Given these conditions, an SNF rod is far from an ideal homogeneous material, and the idealized treatment described in previous sections is not completely accurate.

To improve understanding of the rod's performance, some of these heterogeneous effects on fatigue lifetime were explored by mining the CIRFT data, including (1) pellet-pellet and pellet-cladding bonding rod stiffening, (2) discontinuities in cladding support conditions at pellet-pellet interfaces, (3) cladding hydride reorientation, and (4) effects of the heat treatment applied to three of the SNF rods tested, as described in the following subsections.

F-3.2.1 Pellet Bonding Stiffening

Although the CIRFT data do not allow for separate effects testing, the measured flexural rigidity data can be trended to look for sudden shifts that could indicate pellet-pellet and pellet-cladding debonding. Results from previous testing [F-4, F-5] indicate that pellet-pellet bonding is relatively weak and likely becomes debonded after only a few CIRFT cycles. However, the pellet-cladding bond is expected to be stronger than the pellet-pellet bond. For cases in which the rod was operated in-reactor at high temperature and power, a chemical bond might be developed between the pellet OD and the cladding ID. Wang and Wang proposed a dual flexural rigidity (i.e., before and after the bond is disrupted) with a bonding efficiency that can be applied in rod mechanical performance modeling.

F-3.2.2 Discontinuous Cladding Support

Although the LVDTs used on the CIRFT device only measure the gross rod deflection within the gauge section, several pellet lengths with several pellet-pellet interfaces are included in the gauge section, and any effects related to the pellet-pellet interfaces are embedded in the CIRFT data. As observed in previous test results, fractures are typically located at the pellet-pellet interfaces, which is consistent with the reduced mechanical cross section and potential interaction between the pellet end and cladding at those locations during bending. This is described by Wang and Wang as a fuel pellet “pinning” effect, as illustrated in Figure F-6.

Wang and Wang investigated the effects on the cladding using finite element analysis (FEA) and found that the localized strain in the cladding at the pellet-pellet-cladding interface region is three to four times higher than that in regions supported by the body of the fuel pellet. This is caused by (1) the interaction of the pellet end with the cladding and (2) the localized axial tension that is applied as the gap is opened.

Wang and Wang further explored the shift in the neutral axis that occurs during pinning. The neutral axis shifts constantly with each cycle, but the maximum strain still occurs at the outer radius of the cladding.

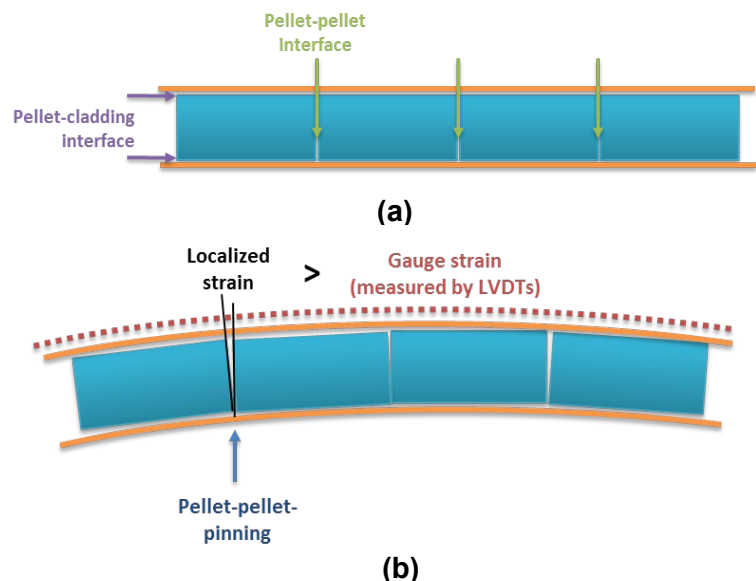


Figure F-6. Cladding and pellet stack (a) in the neutral position and (b) in bending. [F-5]

F-3.2.3 Cladding Hydride Reorientation Effects

Hydrogen taken up by the fuel rod cladding in-reactor can be detrimental to performance when the hydrogen concentration exceeds the alloy's solubility and zirconium hydride platelets are precipitated within the cladding. Wang and Wang completed four CIRFT tests with cladding hydrides that had been purposely reoriented from circumferential to radial; however, a large difference in performance was not observed in fatigue lifetime, and no definitive conclusions could be made.

The sister rod tests provide additional insight with comparisons between heat-treated rods and baseline rods. However, not all sister rod heat treatments resulted in reoriented hydrides because they were treated at more realistic temperature and cladding stress conditions. A description of the heat treatments and the degree of reorientation are provided in Appendices A and B.

F-3.2.4 Cladding Irradiation Defect Annealing

During reactor operation, the cladding is hardened and embrittled through the accumulation of irradiation defects. The baseline sister rods were tested in the as-received condition, and three rods were heat-treated to subject them to the potential for irradiation defect annealing.

F-3.2.5 Normal Condition Impacts

Impacts to the fuel rod are expected to reduce fatigue lifetime because (1) they are expected to disrupt pellet-pellet bonds and pellet-cladding bonds at the impact site, thus leading to a reduced flexural rigidity; (2) the rod's flexural rigidity determines the total deflection of the rod in bending; and (3) a low flexural rigidity results in larger deflections and a corresponding higher stress and strain for a given applied acceleration. Thus, it is postulated that normal condition impacts could reduce the fatigue lifetime of the SNF rods.

Previous testing by Wang and Wang included non-normal impacts from a drop height of 12 in. with indeterminant results that were on the low side of the existing dataset. Future testing is expected to explore this effect with a more controlled impact method.

This page is intentionally blank

F-4. Comparison Data Available from Previous ORNL Tests of Irradiated Rod Segments

The NRC funded the development of the CIRFT and performed testing on HBU SNF with Zircaloy-4 (Zirc-4) and M5 cladding from pressurized water reactors (PWRs) and Zircaloy-2 (Zirc-2) from boiling water reactors (BWRs). Fifty-three cyclic fatigue tests in a range of load amplitudes were performed on PWR rod segments, and 17 tests were performed on BWR rod segments. The burnup of the tested rod segments ranged between 45 and 67 GWd/MTU. The oxide layer thickness on the waterside surface of each segment was not specifically measured but was estimated to be between 20 to 110 μm , with a corresponding estimated hydrogen concentration of 110–800 wppm. Wang and Wang completed four CIRFT tests in which the cladding hydrides were reoriented by pressurizing the segment and applying a thermal transient to determine whether the radial hydrides reduced the fatigue lifetime. The basic data from these tests are directly comparable with the sister rod test results, as summarized in Table F-1 [F-4].

Table F-1. Reference Dynamic Dataset [F-4].

Rod type	Cladding material	Parent rod-average burnup (GWd/MTU)	Test ID	Cycles to failure	Average moment (N-m)	Maximum cladding stress ^a (MPa)	Maximum average stress ^b (MPa)	Maximum average strain (%)	Flexural rigidity (N-m ²)
15×15	Zirc-4	67	Demo1	4.0E+03	28.5	456	233	0.51	30.2
15×15	Zirc-4	67	Dcal ^c	9.6E+03	28.6	366	234	0.41	37.9
15×15	Zirc-4	67	DL2H	1.8E+03	34.1	362	279	0.40	45.6
15×15	Zirc-4	67	S1 ^c	4.6E+03	28.5	327	233	0.36	42.3
15×15	Zirc-4	67	S2 ^c	7.2E+03	28.3	318	231	0.35	43.3
15×15	Zirc-4	67	DH3	7.1E+03	33.7	282	276	0.31	57.9
15×15	Zirc-4	67	R1	5.5E+03	29.0	227	237	0.25	61.9
15×15	Zirc-4	67	S3 ^c	2.5E+04	24.1	214	197	0.24	54.8
15×15	Zirc-4	67	DH2	6.5E+04	18.9	170	155	0.19	53.9
15×15	Zirc-4	67	DL1	1.1E+05	14.1	104	115	0.12	65.6
15×15	Zirc-4	67	DH1	2.5E+05	11.6	99	95	0.11	56.7
15×15	Zirc-4	67	S5	1.8E+05	11.6	84	95	0.09	66.4
15×15	Zirc-4	67	R3	1.3E+05	12.6	73	103	0.08	82.6
15×15	Zirc-4	67	R2	3.9E+05	10.0	70	82	0.08	69.3
15×15	Zirc-4	67	DL3	1.0E+06	9.2	60	75	0.07	73.4
15×15	Zirc-4	67	DM2	2.3E+06	8.2	56	67	0.06	71.9
15×15	Zirc-4	67	R4	2.7E+05	7.8	54	64	0.06	70.0
15×15	Zirc-4	67	HR1 ^d	4.2E+04	15.2	207	124	0.28	29.3
15×15	Zirc-4	67	HR2 ^{c,d}	9.5E+03	14.7	191	120	0.26	31.6
15×15	Zirc-4	67	HR4 ^d	5.5E+04	14.8	158	121	0.21	37.5
15×15	Zirc-4	67	HR3 ^d	2.4E+05	9.0	107	74	0.14	33.6
15×15	Zirc-4	67	DM3	1.3E+07 ^e	7.7	51	63	0.06	73.8
15×15	Zirc-4	67	DM1	1.1E+07 ^e	6.7	44	55	0.05	75.6
15×15	Zirc-4	67	R5	2.2E+07 ^e	6.6	42	54	0.05	76.3
15×15	Zirc-4	67	DL2	6.4E+06 ^e	4.2	22	34	0.03	91.5
17×17	M5	45	TH5	2.8E+04	11.2	312	129	0.32	16.6
17×17	M5	45	TH6	1.3E+04	13.4	308	154	0.32	20.1
17×17	M5	45	MOX17	1.2E+04	11.1	266	128	0.28	19.3

^a Stress calculated using the modified equivalent stress approach [F-4] to represent the cladding surface stress.

^b Stress calculated using the equivalent stress approach per Eq. (F-7) where fuel rod OD for 15 × 15, 17 × 17, and 9 × 9 fuel rods are 10.76, 9.6, and 11.43 mm, respectively [F-7], meaning $I_{15 \times 15} = 6.58\text{E-}10 \text{ m}^4$, $I_{17 \times 17} = 4.2\text{E-}10 \text{ m}^4$, and $I_{9 \times 9} = 8.34\text{E-}10 \text{ m}^4$.

^c Samples were tested statically before dynamic testing.

^d The specimens were pressurized and subjected to a thermal transient to induce cladding hydride reorientation before conducting the unpressurized CIRFT test.

^e The test was discontinued without specimen fracture.

Table F-1. Reference Dynamic Dataset [F-4] (continued).

Rod type	Cladding material	Parent rod-average burnup (GWd/MTU)	Test ID	Cycles to failure	Average moment (N-m)	Maximum cladding stress ^a (MPa)	Maximum average stress ^b (MPa)	Maximum average strain (%)	Flexural rigidity (N-m ²)
17×17	M5	45	TH3	1.5E+04	10.6	264	122	0.27	18.5
17×17	M5	45	TH2	5.7E+04	11.0	255	127	0.14	20.1
17×17	M5	45	MOX14	8.7E+04	6.2	254	71	0.26	11.3
17×17	M5	45	MOX7	1.6E+04	13.9	239	160	0.25	26.9
17×17	M5	52	NA7	1.3E+04	13.5	232	155	0.30	27.1
17×17	M5	45	MOX8	1.3E+04	11.0	206	127	0.21	24.9
17×17	M5	45	TH1	5.7E+04	8.8	204	101	0.21	19.9
17×17	M5	52	NA1	1.6E+04	11.0	194	127	0.25	26.2
17×17	M5	45	MOX13	2.7E+04	8.7	171	100	0.18	23.6
17×17	M5	45	MOX15	2.0E+04	8.5	167	98	0.17	23.5
17×17	M5	45	MOX2	3.7E+04	8.5	161	98	0.17	24.3
17×17	M5	45	MOX12	4.2E+04	8.7	158	100	0.16	25.6
17×17	M5	45	TH4	2.5E+06	6.3	151	73	0.16	19.2
17×17	M5	52	NA2	2.2E+04	8.8	149	101	0.19	27.4
17×17	M5	45	MOX10	3.9E+04	8.7	144	100	0.15	28.2
17×17	M5	45	MOX11	4.2E+04	8.7	142	100	0.15	28.1
17×17	M5	45	MOX9	9.0E+04	6.3	121	73	0.13	24.0
17×17	M5	52	NA4	6.1E+04	6.3	84	73	0.11	35.0
17×17	M5	45	MOX16	3.7E+03	13.2	374	152	0.39	16.3
17×17	M5	45	MOX5	4.5E+05	4.8	68	55	0.07	32.6
17×17	M5	45	MOX6	5.4E+05	3.8	64	44	0.07	27.6
17×17	M5	45	MOX4	2.2E+06	3.9	50	45	0.05	36.1
17×17	M5	52	NA6	4.3E+05	4.0	46	46	0.06	40.3
17×17	M5	45	TH2	3.8E+06 ^e	6.2	134	71	0.14	21.6
17×17	M5	52	NA5	5.1E+06 ^e	4.0	54	46	0.07	34.0
9×9	Zirc-2	57	LM1 ^c	9.4E+03	23.4	386	160	0.42	31.7
9×9	Zirc-2	57	LM17	1.3E+04	28.1	365	192	0.40	40.1
9×9	Zirc-2	57	LM16	1.4E+04	28.6	280	195	0.31	53.3
9×9	Zirc-2	57	LM13	2.1E+04	21.4	228	146	0.25	49.0
9×9	Zirc-2	57	LM10	5.2E+04	18.9	210	129	0.23	47.0
9×9	Zirc-2	57	LM7	1.2E+05	13.9	149	95	0.16	48.9
9×9	Zirc-2	57	LM2	1.7E+05	11.5	114	78	0.12	52.6
9×9	Zirc-2	57	LM3	4.9E+05	9.0	104	61	0.11	45.3
9×9	Zirc-2	57	LM15	4.4E+05	9.0	96	61	0.11	48.6
9×9	Zirc-2	57	LM9	7.3E+05	9.1	92	62	0.10	51.2
9×9	Zirc-2	57	LM14	3.9E+05	9.0	85	61	0.09	55.9
9×9	Zirc-2	57	LM5	2.5E+05	7.6	71	52	0.08	56.1
9×9	Zirc-2	57	LM11	3.6E+05	7.7	69	53	0.08	57.6
9×9	Zirc-2	57	LM6	1.8E+06	6.5	66	44	0.07	51.5
9×9	Zirc-2	57	LM8	4.7E+06	6.6	55	45	0.06	62.9
9×9	Zirc-2	57	LM12	7.6E+06 ^e	6.1	88	42	0.10	36.3
9×9	Zirc-2	57	LM17	3.4E+06 ^e	7.5	87	51	0.10	44.7

^a Stress calculated using the modified equivalent stress approach [F-4] to represent the cladding surface stress.

^b Stress calculated using the equivalent stress approach per Eq. (F-7) where fuel rod OD for 15 × 15, 17 × 17, and 9 × 9 fuel rods are 10.76, 9.6, and 11.43 mm, respectively[F-7], meaning $I_{15 \times 15} = 6.58E-10 \text{ m}^4$, $I_{17 \times 17} = 4.2E-10 \text{ m}^4$, and $I_{9 \times 9} = 8.34E-10 \text{ m}^4$.

^c Samples were tested statically before dynamic testing.

^d The specimens were pressurized and subjected to a thermal transient to induce cladding hydride reorientation before conducting the unpressurized CIRFT test.

^e The test was discontinued without specimen fracture.

F-5. Comparison Data from Cladding Tests

Tests of Zirc-4 cladding tubes are being performed to provide data for comparison with the fuel rod segment tests. The cladding tests can also be used to verify whether previously reported fatigue data [F-8] on zirconium alloys (specifically Zirc-2 and Zirc-4, [F-8],[F-9],[F-10]) are representative of the tube geometry. A comparison of cladding tube fatigue with fuel rod fatigue offers a direct indication of the effect of the pellet on fatigue performance. The discontinuities in the pellet cause stress concentrations on the cladding (Section F-3.2.2), so it is expected that the inclusion of the pellet will have a detrimental effect on the fatigue life of the fuel rod compared with cladding-only performance.

This report discusses the results of tests using unirradiated cladding; irradiated cladding tests will be completed in FY23.

F-5.1 Unirradiated Zirc-4 Cladding Tests

The material used was a 17×17 PWR cladding tube made of standard Zirc-4 from two different lots of material: (1) provided by Framatome and received by ORNL in 2015 and (2) provided by Westinghouse (lot W58H7L8F). Samples from the first lot are labeled *Zr4 2015 Rod 1*, and so on, and samples from the second lot are labeled *Zr4-W-1*, and so on. The dimensions of the cladding tubes are consistent with standard 17×17 PWR fuel rods (OD = 9.5 mm, ID = 8.3 mm).

The tubes were mounted into the endcaps using the normal process, ensuring that the epoxy was applied only to the OD surfaces being bonded with the dogbone. A strain gauge was attached to one sample (Zr4-W-2) to develop LVDT dynamic correction factors for cladding tubes; these correction factors are applied to the subsequent fatigue tests and compared with the previously developed LVDT dynamic correction factors for fuel rods [F-4].

Testing was performed on the out-of-cell CIRFT system rather than the system in the hot-cell that was used to test irradiated fuel rods. Data processing was consistent with the processing used by Wang and Wang [F-6]. The test conditions for the strain-gauged specimen, Zr4-W-2 were used to determine the dynamic corrections factor and were chosen to cover the full range of strain amplitudes in both the fuel rod segment and cladding-only testing (ranging from ~ 0.05 to $\sim 0.5\%$, see Table F-2). The test conditions used to measure fatigue performance are defined to establish a characteristic fatigue limit; thus, the focus of this study was on high-cycle fatigue performance, as listed in Table F-3. Testing on all samples was performed under displacement-controlled (or strain-controlled) conditions rather than load-controlled (or stress-controlled) conditions to be consistent with test conditions of O'Donnell-Langer [F-8][F-1] rather than to be consistent with how the fuel rods were tested. The mean strain for all tests was zero.

Table F-2. Test Conditions for Strain-Gauged Test Sample (Zr4-W-2).

Target Strain Amplitude (%)	Frequency	Cycles
0.06	0.05	3
0.06	5.00	200
0.18	0.05	3
0.18	5.00	200
0.37	0.05	3
0.37	5.00	200
0.47	0.05	3
0.47	5.00	200

Table F-3. Test Conditions for Fatigue Tests on Cladding-Only Zirc-4 Tubes (no strain gauges).

Specimen ID	Displacement Control Condition (mm)	Target Strain Amplitude (%)	Test Frequency (Hz)
Zr4-W-1	4.5	0.55	5
Zr4 2015 Rod 2	1.5	0.20	5
Zr4 2015 Rod 2	4.5	0.55	5
Zr4 2015 Rod 3	3.0	0.37	5
Zr4-W-3	3.8	0.47	5
Zr4-W-4	3.3	0.40	5

During these tests, it was observed that the LVDTs produced wear marks on the OD surface of sample Zr4-W-1. To investigate potential effects related to the wear, Sample Zr4 2015 Rod 2 was tested under two conditions: (1) 2×10^6 cycles at $\sim 0.2\%$ strain amplitude with LVDTs in place and (2) after 2×10^6 cycles, testing at 0.55% strain amplitude without the LVDTs to directly measure strain and determine whether the LVDTs had any impact on failure.

Future testing will be performed at strain amplitudes between 0.4% and 0.35% , and the test of Zr4 2015 Rod 3 will continue until failure occurs or 1×10^7 cycles is reached without failure. Typically, if failure has not occurred by 1×10^7 cycles, fatigue failure is not expected at the test conditions.

F-5.1.1 Calibration Sample (Zr4-W-2)

Because of the larger amount of data generated with performing the fatigue tests at 5 Hz for 200 cycles, only a subset of data was collected. Specifically, 10 samples of data were taken (2.5 cycles in length) rather than collecting the entire dataset. Of these 10 samples, the first 3 were not included in the averages that characterized the test because of startup variations. The reported data include the average calculated curvature, strain amplitude, applied moment, and stress at the peaks/valleys of the fatigue cycles.

The test results for the calibration sample are provided in Figure F-7. The LVDT strain amplitude includes the normal correction for Δh , as described in [F-4], but does not include the dynamic correction factor, which is the ratio of the strain-gauge strain amplitude and the LVDT strain amplitude (after correction for Δh). This ratio is provided in Table F-4, and the average is plotted in Figure F-7 for testing at both 0.05 Hz and 5 Hz. The correction factor increases with strain amplitude: from 0.83 below 0.2% to 0.87 and 0.91 at 0.37% and 0.47% , respectively. When performing fatigue tests without a strain gauge, the dynamic correction factor is applied after the normal correction for Δh . As a comparison, the correction factor used for evaluating the sister rod test data was 0.82, which compares well to the cladding-only data given that most of the sister rod tests were also performed at strain amplitudes less than 0.2% .

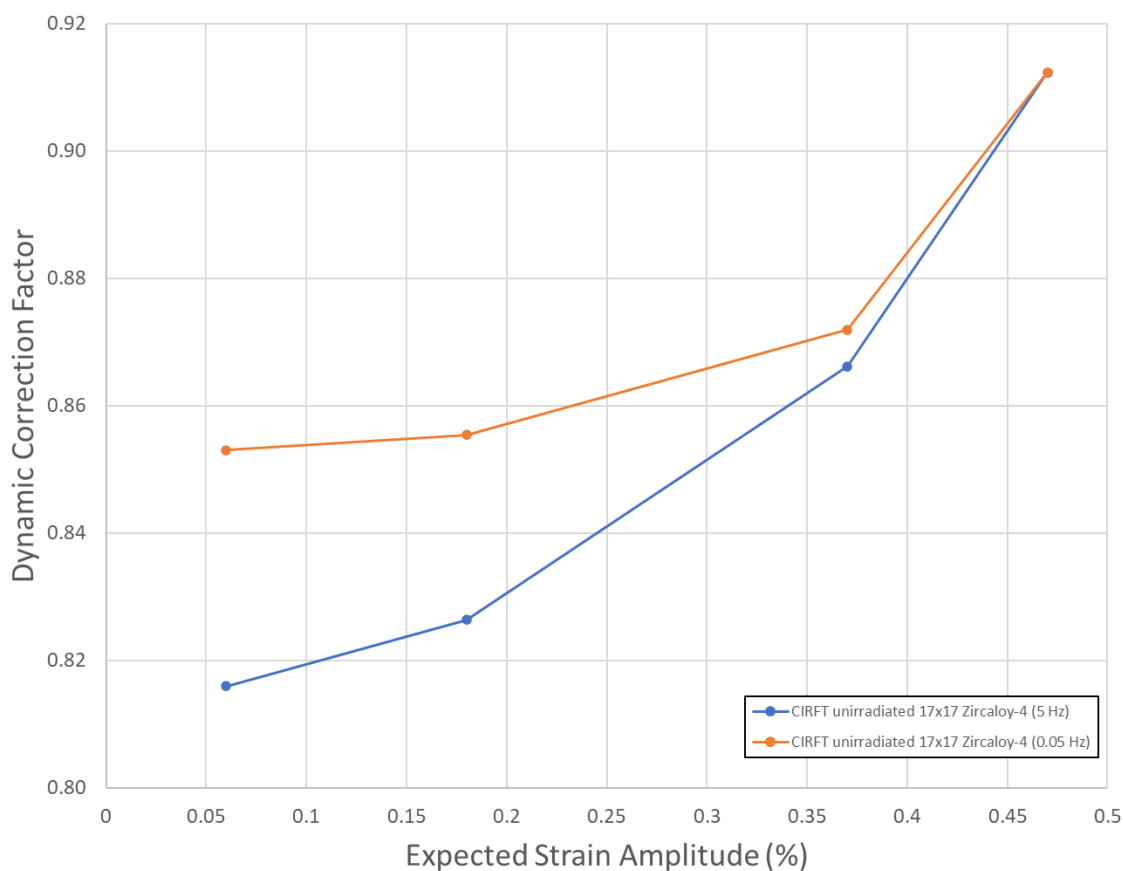


Figure F-7. Results for Strain Gauge Sample Zr4-W-2.

Table F-4. Dynamic Correction Factor as a Function of the Strain Gauge Strain Amplitude for Testing at 0.05 and 5 Hz.

Test ID	Test Conditions (strain amplitude- %/frequency-Hz)	LVDT Strain Amplitude (%)	Strain Gauge Strain Amplitude (%)	Dynamic Correction Factor	Corrected LVDT Curvature (1/m)	Applied Moment (N-M)	Dynamic flexural rigidity (N-m ²)
Zr4-W-2-05-05-1	0.06/0.05	0.075	0.062	0.83	0.13	2.43	18.58
Zr4-W-2-05-05-2	0.06/0.05	0.070	0.062	0.89	0.13	2.53	19.34
Zr4-W-2-05-05-3	0.06/0.05	0.074	0.062	0.84	0.13	2.52	19.21
	Mean	0.073	0.062	0.85	0.13	2.49	19.05
	St.Dev	0.0026	0.0001	0.0304	0.0047	0.0559	0.4106
Zr4-W-2-05-5-1	0.06/5	0.078	0.064	0.82	0.13	2.35	17.45
Zr4-W-2-05-5-2	0.06/5	0.082	0.064	0.78	0.14	2.36	17.43
Zr4-W-2-05-5-3	0.06/5	0.076	0.064	0.84	0.13	2.34	17.41
	Mean	0.079	0.064	0.82	0.14	2.35	17.43
	St.Dev	0.0033	0.0002	0.0323	0.0057	0.0069	0.0207

Table F-4. Dynamic Correction Factor as a Function of the Strain Gauge Strain Amplitude for Testing at 0.05 and 5 Hz (continued).

Test ID	Test Conditions (strain amplitude- %/frequency-Hz)	LVDT Strain Amplitude (%)	Strain Gauge Strain Amplitude (%)	Dynamic Correction Factor	Corrected LVDT Curvature (1/m)	Applied Moment (N-M)	Dynamic flexural rigidity (N- m ²)
Zr4-W-2-15-05-1	0.18/0.05	0.219	0.185	0.85	0.39	6.59	16.90
Zr4-W-2-15-05-2	0.18/0.05	0.221	0.185	0.84	0.40	6.65	17.07
Zr4-W-2-15-05-3	0.18/0.05	0.210	0.186	0.88	0.38	6.62	16.92
	Mean	0.217	0.185	0.86	0.39	6.62	16.96
	St.Dev	0.0056	0.0004	0.0245	0.0101	0.0286	0.0909
Zr4-W-2-15-5-1	0.18/5	0.228	0.185	0.81	0.40	5.27	13.53
Zr4-W-2-15-5-2	0.18/5	0.231	0.185	0.80	0.40	5.34	13.72
Zr4-W-2-15-5-3	0.18/5	0.215	0.186	0.86	0.37	5.38	13.78
	Mean	0.224	0.185	0.83	0.39	5.33	13.68
	St.Dev	0.0084	0.0004	0.0336	0.0147	0.0593	0.1282
Zr4-W-2-30-05-1	0.37/0.05	0.432	0.372	0.86	0.79	12.75	16.27
Zr4-W-2-30-05-2	0.37/0.05	0.426	0.375	0.88	0.78	12.72	16.14
Zr4-W-2-30-05-3	0.37/0.05	0.428	0.375	0.87	0.79	12.74	16.16
	Mean	0.429	0.374	0.87	0.79	12.74	16.19
	St.Dev	0.0029	0.0012	0.0086	0.0053	0.0143	0.0676
Zr4-W-2-30-5-1	0.37/5	0.433	0.375	0.86	0.79	11.11	14.10
Zr4-W-2-30-5-2	0.37/5	0.433	0.376	0.87	0.79	11.20	14.17
Zr4-W-2-30-5-3	0.37/5	0.434	0.376	0.87	0.79	11.10	14.04
	Mean	0.433	0.375	0.87	0.79	11.14	14.10
	St.Dev	0.0008	0.0007	0.0016	0.0015	0.0516	0.0666
Zr4-W-2-38-05-1	0.47/0.05	0.519	0.476	0.92	1.00	16.14	16.11
Zr4-W-2-38-05-2	0.47/0.05	0.524	0.477	0.91	1.01	16.03	15.98
Zr4-W-2-38-05-3	0.47/0.05	0.527	0.479	0.91	1.01	16.07	15.95
	Mean	0.523	0.477	0.91	1.00	16.08	16.01
	St.Dev	0.0040	0.0014	0.0050	0.0076	0.0585	0.0843
Zr4-W-2-38-5-1	0.47/5	0.524	0.479	0.92	1.01	14.32	14.20
Zr4-W-2-38-5-2	0.47/5	0.523	0.480	0.92	1.01	14.17	14.04
Zr4-W-2-38-5-3	0.47/5	0.530	0.481	0.91	1.02	14.11	13.94
	Mean	0.526	0.480	0.91	1.01	14.20	14.06
	St.Dev	0.0036	0.0008	0.0050	0.0070	0.1068	0.1265

F-5.1.2 High Cycle Fatigue Response

Like the testing performed at 5 Hz on the calibration sample, the fatigue data reported for the cladding-only samples are averages of a subset of the data. Because the number of cycles varied during the test, the total number of datasets included in the average also varied. The reported data provided in Table F-5 and Table F-6 include the average calculated curvature, strain amplitude, applied moment, dynamic flexural rigidity, and stress at the peaks/valleys of a fatigue cycle with the number of cycles to failure. Two stress values are reported in Table F-6. The first is the average stress based on beam theory assuming a homogeneous rod with the flexural rigidity of the tube; this value is reported to be compared directly with the fuel rod data in Section F-8. The second is the cladding stress, which is calculated as the product of the Young's modulus and strain amplitude. The strain amplitude is plotted in Figure F-8 as a function of fatigue cycles, and the results are compared with data on unirradiated and irradiated Zirc-2 from O'Donnell-Langer [F-8] and open literature data on Zirc-4 [F-9],[F-10]. The cladding-only data indicate fatigue performance similar to other Zirc-4 data and are consistent with a higher fatigue limit than represented by the best estimate correlation of O'Donnell-Langer for Zirc-2. The results support the conclusion that the tube geometry does not alter the expected fatigue behavior based on O'Donnell-Langer (and other open literature) data on zirconium alloys and the conclusion that the O'Donnell-Langer design curve is applicable for Zirc-4 in a tube geometry.

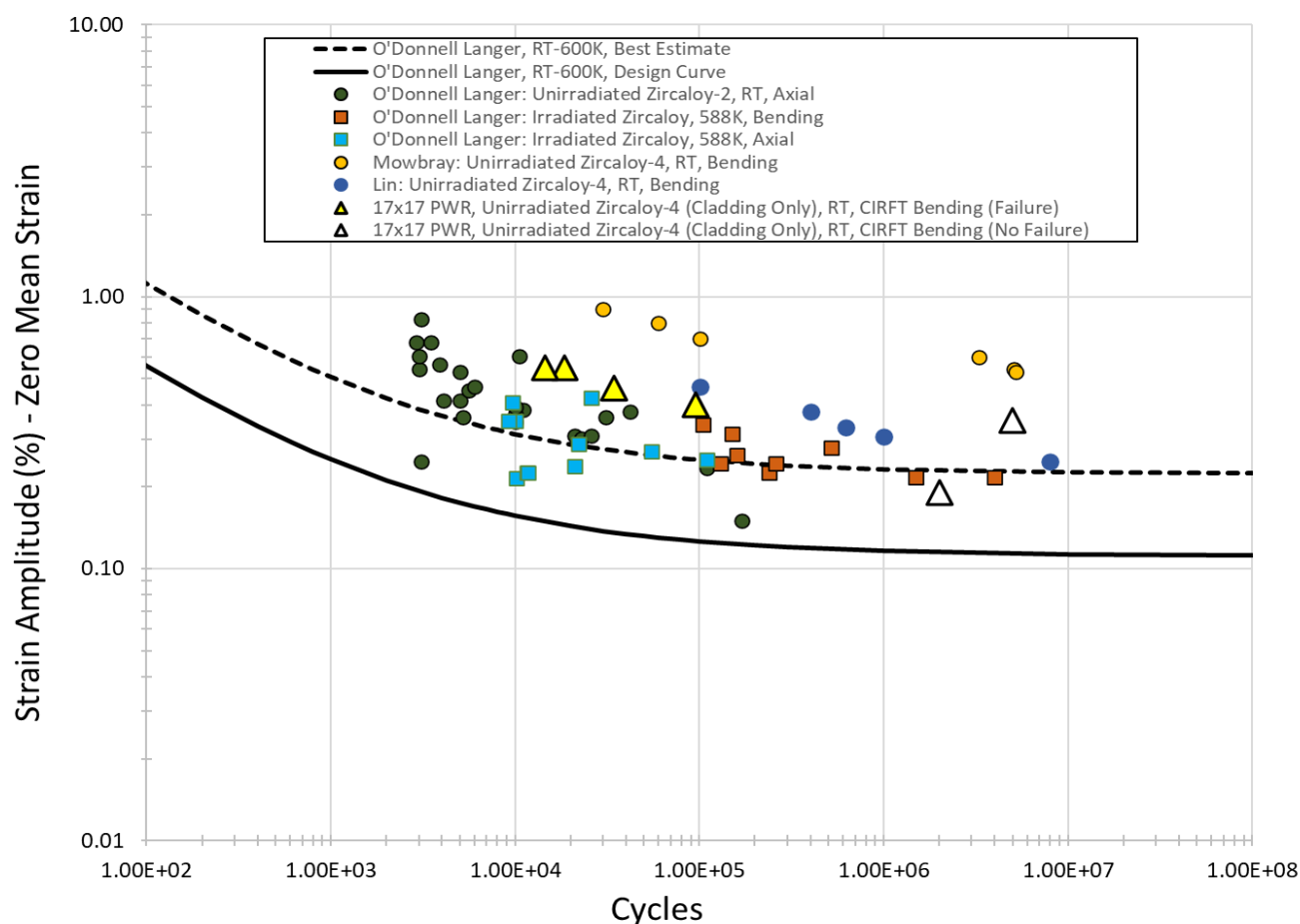
Table F-5. Curvature, Strain Amplitude, Applied Moment, and Cycles to Failure for the Unirradiated Zirc-4 Cladding Tubes.

Specimen Material	Specimen ID	Target Displacement and Strain Amplitude (1/m)	LVDT Curvature (1/m)	St. Dev. LVDT Curvature (1/m)	LVDT Strain Amplitude (%)	St. Dev LVDT Strain Amplitude (%)	Applied Moment Amplitude (N-m)	St. Dev. Applied Moment Amplitude (N-m)	Fatigue Cycles (N)	Failed (Yes/No)
Zirc-4	Zr4-W-1	4.5/0.55	1.12	0.17	0.53	0.08	14.25	0.66	14,500	Yes
Zirc-4	Zr4 2015 Rod 2	1.5/0.20	0.43	0.01	0.21	0.003	5.61	0.09	2,000,000	No
Zirc-4	Zr4 2015 Rod 2	4.5/0.55	N/A	N/A	N/A	N/A	15.65	0.13	18,500	Yes
Zirc-4	Zr4 2015 Rod 3	3.0/0.35	0.83	0.02	0.39	0.01	11.14	0.08	5,000,000	No
Zirc-4	Zr4-W-3	3.8/0.46	0.97	0.02	0.46	0.01	12.89	0.23	34,300	Yes
Zirc-4	Zr4-W-4	3.3/0.40	0.85	0.03	0.40	0.01	10.98	0.16	95,000	Yes

Note: The dynamic corrections factor for Zr4 2015 Rod 2 (0.21% strain amplitude) was 0.82; the dynamic corrections factor for all other tests was 0.87.

Table F-6. Maximum Average Stress, Maximum Stress, Dynamic Flexural Rigidity, and Rigidity Standard Deviation for the Unirradiated Zirc-4 Cladding Tubes

Cladding Material	Specimen ID	Maximum Average Stress (Mpa)	Maximum Cladding Stress (MPa)	Dynamic Flexural Rigidity Stress (N-m ²)	St. Dev. Dynamic Flexural Rigidity (N-m ²)
Zirc-4	Zr4-W-1	423	485	12.9	0.8
Zirc-4	Zr4 2015 Rod 2	167	189	13.3	0.1
Zirc-4	Zr4 2015 Rod 2	464	N/A	N/A	N/A
Zirc-4	Zr4 2015 Rod 3	331	361	13.4	0.4
Zirc-4	Zr4-W-3	382	421	13.3	0.1
Zirc-4	Zr4-W-4	326	368	13.0	0.7

**Figure F-8. CIRFT results of unirradiated Zirc-4 tubes compared with previously reported data on both unirradiated and irradiated Zirc-2 [F-8] and unirradiated Zirc-4 [F-9],[F-10].**

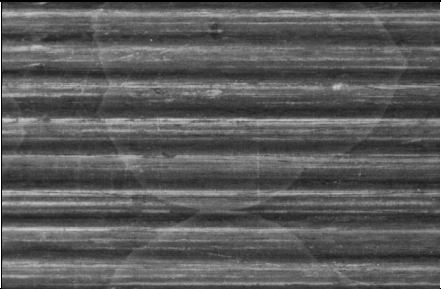
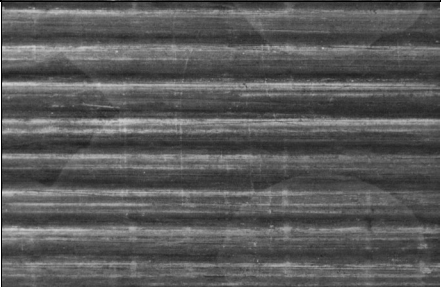

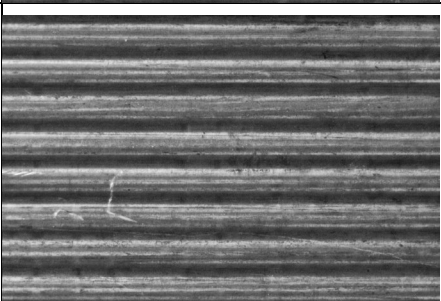
F-6. Description of the Sister Rods Tested

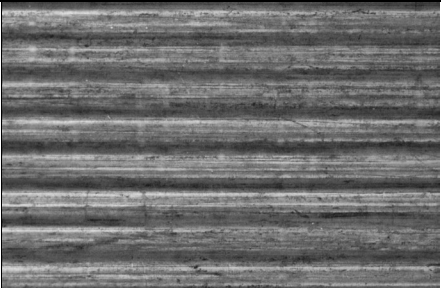
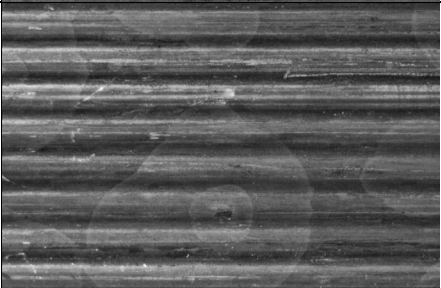
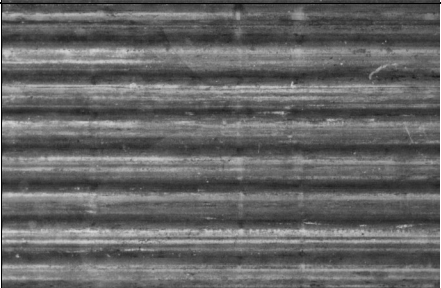


Additional descriptions of the rods used in these tests are provided in the sister rod test plan [F-3] and the nondestructive test results [F-11]. All rods were operated by Dominion Energy at the North Anna Power Station to high rod average burnup (>45 GWd/MTU). Table F-7 summarizes the parent assembly operation and lattice location for the rods test using CIRFT.

In Phase 1 of the sister rod test program [F-1, F-2], 7 of ORNL's 15 sister rods were selected for paired testing: 1 baseline fuel rod and 1 heat-treated fuel rod of each cladding type (M5, ZIRLO, and Zirc-4/LT-Zirc-4), plus an extra ZIRLO-clad rod for additional data points because no ZIRLO-clad rods were tested in previous campaigns. Baseline rods are tested in the condition in which they were received at ORNL, and full-length heat-treatment (FHT) rods are subjected to a thermal transient before testing, as described in Appendix A, to simulate dry storage conditions. Three full-length fuel rods have been heat-treated to date—one Zirc-4-clad (F35P17), one ZIRLO-clad (3F9N05), and one M5-clad (30AE14)—and the results from the heat-treated rods were compared with the results from the baseline rods to determine whether the fatigue lifetime is affected by dry storage thermal transients.

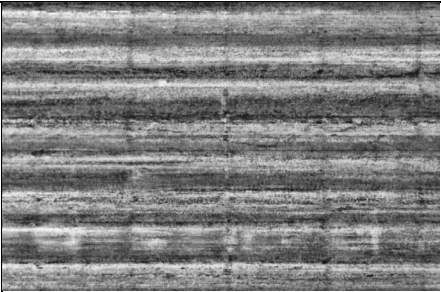
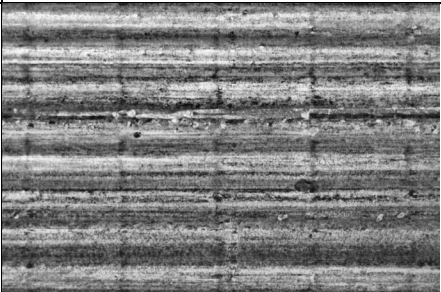
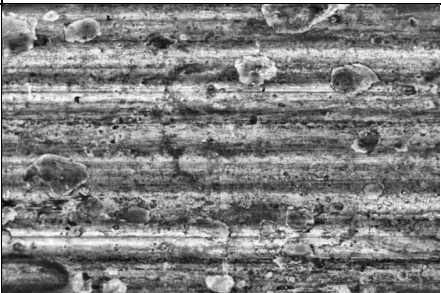
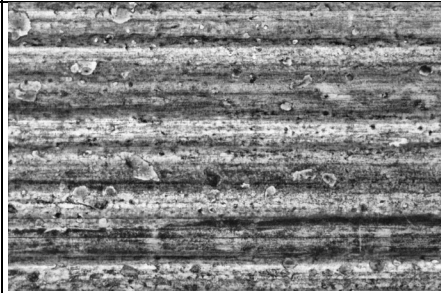
The CIRFT uses specimens that are 152.4 mm (6 in.) long that were taken from various elevations along the SNF rods. Because rod burnup varies as a function of elevation, the rod average burnup is used in conjunction with the gamma scans of the rod [F-11] to estimate the average burnup of the CIRFT segment, as listed in Table F-7. Full-circumference flattened images—as defined in the nondestructive examination (NDE) report [F-11]—of the pretest waterside surface condition of the CIRFT segments are also provided in Table F-7.

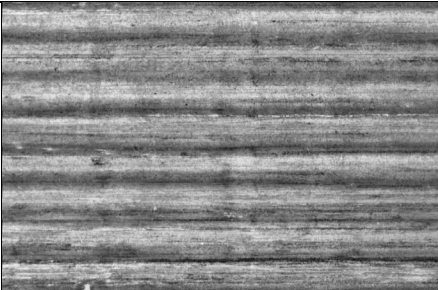
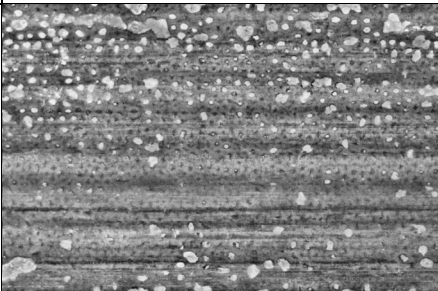
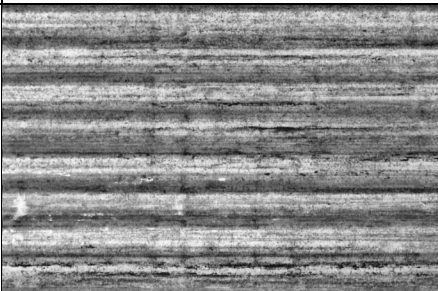
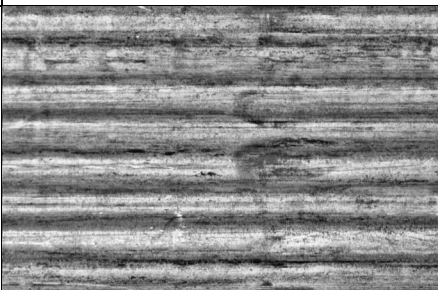
Table F-7. Sister Rod Segments Selected for CIRFT.

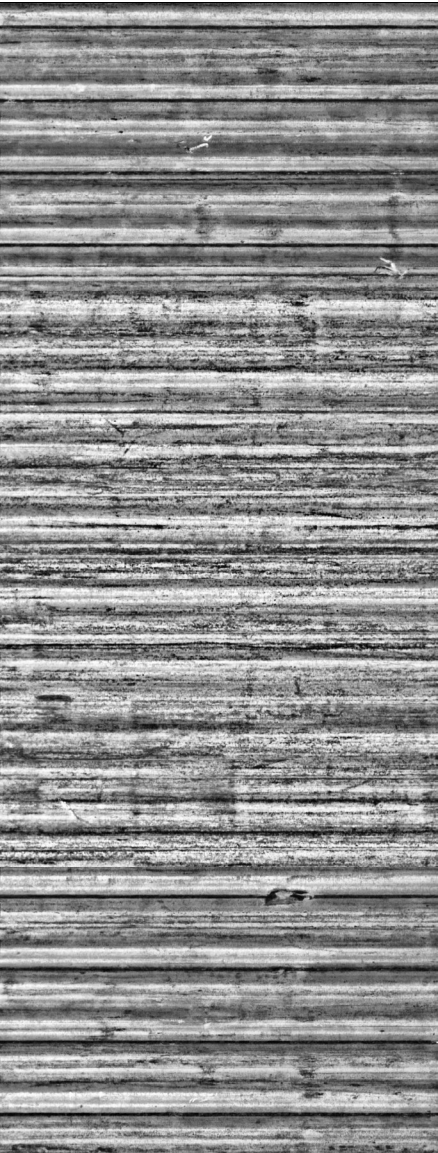
Clad material	Donor assembly	Sister rod lattice location	Assembly average burnup (GWd/MTU)	Rod average burnup (GWd/MTU)	Heat treatment applied to the rod	Measured rod internal pressure (MPa)	Measured rod void volume (cc)	Specimen lower elevation (mm)	Specimen upper elevation (mm)	Average specimen burnup (GWd/MTU)	Rod 360° appearance near the CIRFT gauge section pretest
The M5-clad rods exhibited very light waterside oxide that is visible as irregular, somewhat circular patches, with some areas including an interior patch that appears to have peeling oxide. Grid-to-rod-fretting (GTRF) marks are visible in some grid elevations, along with rod removal scratches.											
M5	30A	D05	52.0	54	No	3.46	10.63	697	850	58	
	30A	D05	52.0	54	No	3.46	10.63	2,050	2,203	59	
	30A	D05	52.0	54	No	3.46	10.63	2,630	2,783	59	
	30A	D05	52.0	54	No	3.46	10.63	3,732	3,886	24	 Pellet-pellet gaps throughout

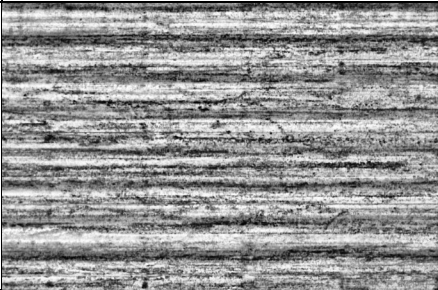
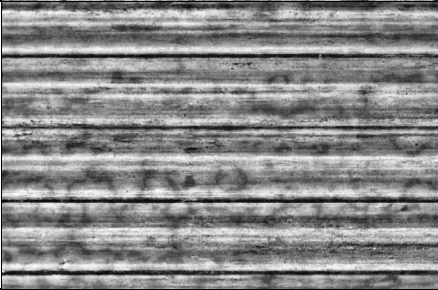
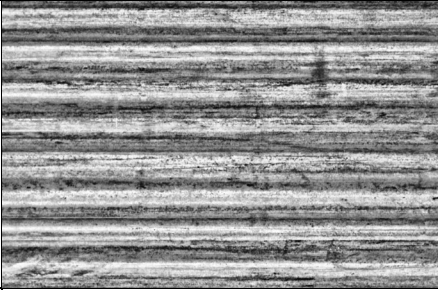
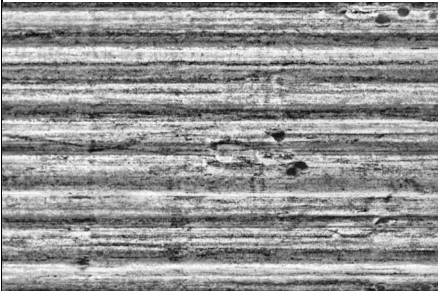
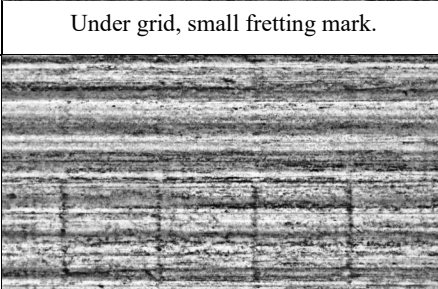
Clad material	Donor assembly	Sister rod lattice location	Assembly average burnup (GWd/MTU)	Rod average burnup (GWd/MTU)	Heat treatment applied to the rod	Measured rod internal pressure (MPa)	Measured rod void volume (cc)	Specimen lower elevation (mm)	Specimen upper elevation (mm)	Average specimen burnup (GWd/MTU)	Rod 360° appearance near the CIRFT gauge section pretest
M5	30A	D05	52	54	No	3.46	10.63	3,452	3,605	38	
	30A	E14	52	54	Yes	3.22	10.99	672	825	56	
	30A	E14	52	54	Yes	3.22	10.99	2,850	3,003	60	
	30A	E14	52	54	Yes	3.22	10.99	3,156	3,309	56	
	30A	E14	52	54	Yes	3.22	10.99	3,003	3,156	58	

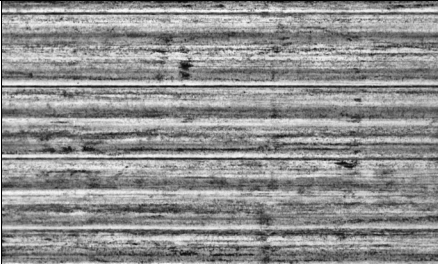
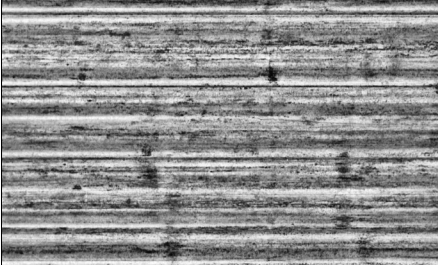


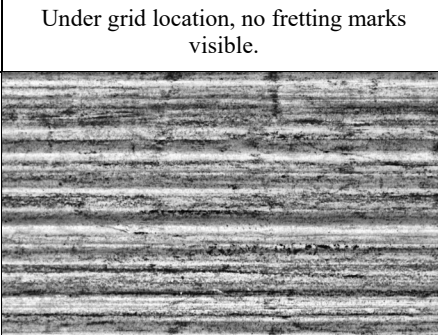
January 31, 2024

Clad material	Donor assembly	Sister rod lattice location	Assembly average burnup (GWd/MTU)	Rod average burnup (GWd/MTU)	Heat treatment applied to the rod	Measured rod internal pressure (MPa)	Measured rod void volume (cc)	Specimen lower elevation (mm)	Specimen upper elevation (mm)	Average specimen burnup (GWd/MTU)	Rod 360° appearance near the CIRFT gauge section pretest
Assemblies 3A1 and F35 (Zirc-4/LT Zirc-4 cladding types) appeared to have the greatest amount of oxide buildup/spalling among the sister rods. No visible signs of through-wall damage or large areas of clad degradation were found, but some areas of significant oxidation have a flake-like appearance, and spalling is evident at some elevations. Some shallow GTRF marks are visible, and some features that appear to be GTRF marks oxidized in later cycles are visible.											
LT Zirc-4	3A1	F05	50	51	No	3.73	12.94	1,853	2,006	56	
	3A1	F05	50	51	No	3.73	12.94	2,025	2,178	56	
	3A1	F05	50	51	No	3.73	12.94	3,214	3,367	48	 Under grid location, no fretting marks visible.
	3A1	F05	50	51	No	3.73	12.94	3,367	3,520	44	

Clad material	Donor assembly	Sister rod lattice location	Assembly average burnup (GWd/MTU)	Rod average burnup (GWd/MTU)	Heat treatment applied to the rod	Measured rod internal pressure (MPa)	Measured rod void volume (cc)	Specimen lower elevation (mm)	Specimen upper elevation (mm)	Average specimen burnup (GWd/MTU)	Rod 360° appearance near the CIRFT gauge section pretest
Assemblies 3A1 and F35 (Zirc-4/LT Zirc-4 cladding types) appeared to have the greatest amount of oxide buildup/spalling among the sister rods. No visible signs of through-wall damage or large areas of clad degradation were found, but some areas of significant oxidation have a flake-like appearance and spalling is evident at some elevations. Some shallow GTRF marks are visible, and some features that appear to be GTRF marks that have oxidized in later cycles are visible.											
Zirc-4	F35	P17	58	60	Yes	4.68	13.32	2,027	2,180	66	
	F35	P17	58	60	Yes	4.68	13.32	1,855	2,008	66	
	F35	P17	58	60	Yes	4.68	13.32	3,159	3,312	61	
	F35	P17	58	60	Yes	4.68	13.32	3,312	3,465	56	

Clad material	Donor assembly	Sister rod lattice location	Assembly average burnup (GWd/MTU)	Rod average burnup (GWd/MTU)	Heat treatment applied to the rod	Measured rod internal pressure (MPa)	Measured rod void volume (cc)	Specimen lower elevation (mm)	Specimen upper elevation (mm)	Average specimen burnup (GWd/MTU)	Rod 360° appearance near the CIRFT gauge section pretest
The ZIRLO-clad rods have a moderate-to-heavy oxide layer, with some oxide peeling observed. GTRF marks are present on most rods and range in severity from shallow to deep. No visible signs of through-wall cladding damage were observed. Darker regions are present at grid elevations, indicating either CRUD or possibly a thinner oxidation layer (attributed to better heat transfer in those areas resulting from flow turbulence).											
ZIRLO	3D8	E14	55	59	No	4.18	11.73	719	872	64	
	3D8	E14	55	59	No	4.18	11.73	2,412	2,565	64	
	3D8	E14	55	59	No	4.18	11.73	2,963	3,116	62	
	3D8	E14	55	59	No	4.18	11.73	1,178	1,331	63	
											Under grid location, GTRF mark aligned at maximum strain location

Clad material	Donor assembly	Sister rod lattice location	Assembly average burnup (GWd/MTU)	Rod average burnup (GWd/MTU)	Heat treatment applied to the rod	Measured rod internal pressure (MPa)	Measured rod void volume (cc)	Specimen lower elevation (mm)	Specimen upper elevation (mm)	Average specimen burnup (GWd/MTU)	Rod 360° appearance near the CIRFT gauge section pretest
ZIRLO	3D8	E14	55	59	No	4.18	11.73	3,225	3,378	56	
	3F9	N05	52	54	Yes	3.98	12.74	719	872	59	
	3F9	N05	52	54	Yes	3.98	12.74	2,329	2,482	59	
	3F9	N05	52	54	Yes	3.98	12.74	2,710	2,863	57	
	3F9	N05	52	54	Yes	3.98	12.74	3,440	3,593	45	

Clad material	Donor assembly	Sister rod lattice location	Assembly average burnup (GWd/MTU)	Rod average burnup (GWd/MTU)	Heat treatment applied to the rod	Measured rod internal pressure (MPa)	Measured rod void volume (cc)	Specimen lower elevation (mm)	Specimen upper elevation (mm)	Average specimen burnup (GWd/MTU)	Rod 360° appearance near the CIRFT gauge section pretest
ZIRLO	6U3	K09	53	55	no	3.64	11.78	2,310	2,463	59	
	6U3	K09	53	55	no	3.64	11.78	2,463	2,616	59	
	6U3	K09	53	55	no	3.64	11.78	2,635	2,788	58	
	6U3	K09	53	55	no	3.64	11.78	3,200	3,353	50	
	6U3	K09	53	55	no	3.64	11.78	3,353	3,506	46	

Under grid location, no fretting marks visible.

F-7. Selection of CIRFT Test Conditions

In specifying the loading conditions for the CIRFT tests, the previous data for M5 and Zirc-4 clad fuel rods were surveyed, [F-4,F-5] and several objectives were identified for the sister rod tests:

- Demonstrate that M5 and Zirc-4 clad sister rod fatigue performance is consistent with the data given in the established database for those cladding alloys
- Demonstrate whether FHT changes the fatigue lifetime of the cladding/rod when compared with non-FHT segments
- Demonstrate whether grid-to-rod fretting (GTRF) marks result in a reduced fatigue lifetime when they are aligned with the point of peak cladding deflection during the test
- Establish a range of tests for rods that have ZIRLO cladding consistent with the data given in the established database for other cladding alloys and demonstrate whether the ZIRLO-clad rods are consistent with other rods
- Demonstrate whether nonzero mean strain conditions degrade fatigue performance compared with zero mean strain

The sister rods are tested statically and dynamically as paired samples with similar burnup and oxide thicknesses.

- a. **Baseline rod specimens:** one specimen tested statically followed by a dynamic test at a relatively high load (~175 N-m), one specimen tested dynamically at a moderate load (~10–12 N-m), and one specimen tested dynamically at a low load (~5–6 N-m)
- b. **Heat-treated rod specimens:** one specimen tested statically followed by a dynamic test at the same load used for the baseline specimen, one specimen tested dynamically at the same moderate load used for the baseline specimen, and one specimen tested dynamically at the same low load used for the baseline specimen

Table F-8 lists the selected test type, test load, and paired specimens for testing performed at zero mean strain. Because testing under nonzero mean strain conditions has been identified as more important than the cumulative test type, the five samples identified for cumulative testing in Table F-8 have been repurposed for non-zero mean strain testing to represent the case where the rod is internally pressurized. The target test conditions at non-zero mean strain are provided in Table F-9. These were chosen to encompass the maximum expected non-zero mean strain conditions based on recommendations documented in Cantonwine et al. [F-12] for fatigue of an internally pressurized fuel rod.

Table F-8. CIRFT Specimen and Test Pairing

Baseline specimens					Heat-treated specimens					Test type	Nominal test moment applied (N-m)	Notes
Specimen ID		Cladding type	Estimated specimen average burnup (GWd/MTU)		Specimen ID		Cladding type	Estimated specimen average burnup (GWd/MTU)				
30AD05	0697	0850	M5	58	30AE14	0672	0825	M5	56	Static followed by Dynamic	17.8	---
30AD05	2050	2203		59	30AE14	3156	3309		56	Dynamic	6.1	---
30AD05	2630	2783		59	30AE14	2850	3003		60	Dynamic	12.2	---
30AD05	3732	3886		24						Dynamic	--	pellet-pellet gaps – not yet tested
30AD05	3452	3605	M5	38	30AE14	3003	3156	M5	58	Cumulative	--	Future test
3A1F05	1853	2006	LT Zirc-4	56	F35P17	1855	2008	Zirc-4	66	Static followed by Dynamic	17.8	---
3A1F05	3367	3520		44	F35P17	2027	2180		66	Dynamic	5.1	Replacement; originally allocated as a cumulative test specimen
3A1F05	2025	2178		56						Dynamic	10.2	Originally allocated for 5.1 N-m but mistakenly tested at 10.2 N-m
3A1F05	3214	3367		48	F35P17	3159	3312		61	Dynamic	10.2	
					F35P17	3312	3465	Zirc-4	56	Cumulative	--	Future test
3D8E14	0719	0872	ZIRLO	64	3F9N05	719	872	ZIRLO	59	Static followed by Dynamic	17.8	---
3D8E14	2412	2565		64	3F9N05	2329	2482		59	Dynamic	6.1	---
3D8E14	2963	3116		62	3F9N05	2710	2863		57	Dynamic	10.2	---
3D8E14	1178	1331		63						Dynamic	6.1	---
6U3K09	2310	2463		59						Dynamic	14.3	Additional higher load data point
6U3K09	2463	2616		59						Dynamic	10.2	Provides a good comparison with 3F9N05-2710-2863 based on segment burnup
6U3K09	2635	2788		58						Dynamic	7.6	Provides a good comparison with 3F9N05-2329-2482 based on segment burnup
6U3K09	3200	3353		50						Dynamic	10.2	Provides a comparison with 3F9N05-2710-2863 based on segment burnup
6U3K09	3353	3506		46						Dynamic	13.3	Additional higher load data point
3D8E14	3225	3378	ZIRLO	56	3F9N05	3440	3593	ZIRLO	45	Cumulative	--	Future test

Table F-9. Non-zero Mean Strain Dynamic Test Conditions

Specimen ID				Cladding Type	Estimated specimen average burnup (GWd/MTU)	Target Strain Amplitude (%)	Target Mean Strain (%)	Target Maximum Moment (N-m)	Notes
3F9N05	3440	3593		ZIRLO	47	0.06	0.05	6.0	---
3D8E14	3225	3378		ZIRLO	56	0.06	0.05	6.0	---
F35P17	3312	3465		Zirc-4	56	0.05	0.05	6.0	---
30AE14	3003	3156		M5	58	0.05	0.05	6.0	---
30AD05	3452	3605		M5	38	--	--	--	Not tested

F-8. CIRFT Test Results for the Sister Rods Tested

F-8.1 Static Tests

The static test is performed to measure the range of flexure of representative specimens for each sister rod cladding type: M5, ZIRLO, and Zirc-4 or LT Zirc-4. Six specimens—one of each cladding type and heat treatment—were tested in static mode to measure the flexural rigidity before testing the fatigue response in dynamic mode. An example of the data typically acquired is shown in Figure F-9; all were flexed beyond the knee in the curve, which is labeled as point B in Figure F-9 (a). The static flexural rigidity is calculated on the linear portion of the curve from approximately points A to B; this is consistent with the definition of EI2 in Reference [F-13].

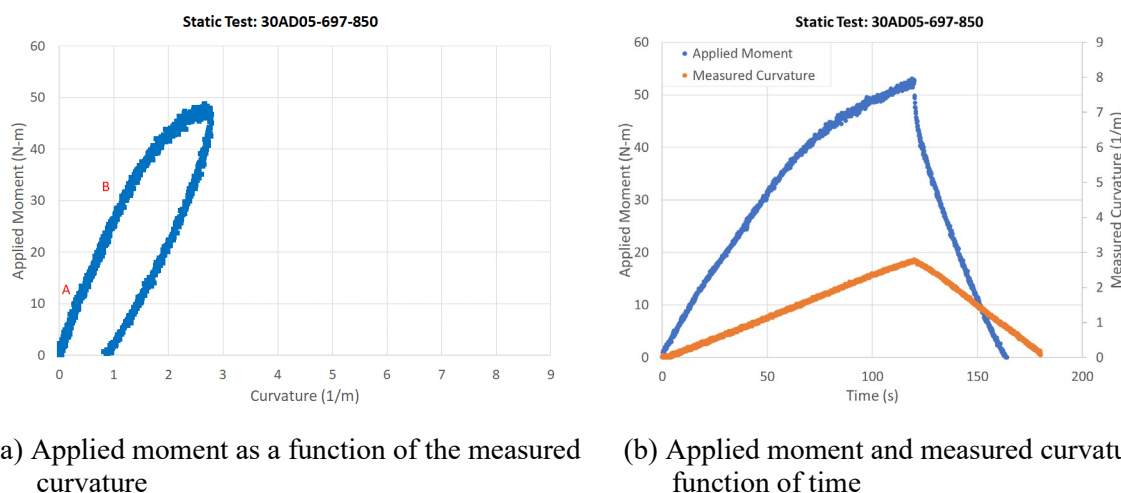


Figure F-9. Static test data for 30AD05-0697-0850 represent the typical result.

A deep investigation of the static test data revealed that specimen F35P17-1855-2008 failed during the static test. Rod F35P17 is a Zirc-4 clad rod that was heat treated before CIRFT testing. During the static test, there was an observed drop in the applied moment that correlated with an increase in the measured curvature. In addition, in subsequent dynamic fatigue testing the measured applied moment was lower than expected based on the measured flexural rigidity before failure. There are indications of oxide spalling on the specimen tested (see Figure F-29), which might have contributed to failure of the rod. Based on these observations, the only data from the static test considered valid for this specimen is the prefailure static flexural rigidity, which is reported in Table F-10; subsequent dynamic test data are not valid and are not included in the reported CIRFT dataset.

During the static tests of 30AE14-0672-0825 and 3D8E14-0719-0872, the LVDTs were not responding as expected, appearing to be stuck at times, and they did not provide consistent curvature or rigidity information. Therefore, data from these static tests are not reported in Table F-4.

The results of the remaining valid static tests are provided in Table F-10 with a comparison of the flexural rigidity results from the dynamic tests (Section F-8.2). Generally, the dynamically measured A-B rigidity of the statically tested specimens should be lower than the statically measured rigidity because the rod is usually flexed past the yield point during the static test. This was observed in the three samples that had valid rigidity measurements in both the static and dynamic tests (30AD05-0697-0850, 3A1F05-1853-2006 and 3F9N05-0719-0872), though in two cases the difference is within the measurement uncertainty.

Table F-10. Static Test Results.

Cladding material	Heat-treated?	Estimated specimen-average burnup (GWd/MTU)	Specimen ID	Maximum applied moment (N-m)	Applied moment from A to B (N-m)	Flexural rigidity in A to B region (N-m ²)	Dynamically applied moment (N-m) ^a	Dynamically measured flexural rigidity (after static flexure) (N-m ²) ^a
M5	No	58	30AD05-0697-0850	47.4	11.1-30.9	23.7 ± 7.8	15.8	15.6 ± 1.2
M5	Yes	56	30AE14-0672-0825	Not reported due to data acquisition issue			15.55	20.5 ± 4.2
LT Zirc-4	No	56	3A1F05-1853-2006	49.8	16.0 – 35.4	20.3 ± 6.5	15.92	19.3 ± 3.9
Zirc-4	Yes	66	F35P17-1855-2008	Not reported due to data acquisition issue	8.8 – 24.8	20.6 ± 7.2	N/A ^b	N/A ^b
ZIRLO	No	64	3D8E14-0719-0872	Not reported due to data acquisition issue			15.3	18.4 ^c
ZIRLO	Yes	59	3F9N05-0719-0872	46.6	17.2 to 31.9	21.9 ± 9.2	15.53	18.0 ± 3.6

^a Data are discussed in Section F-8.2.

^b Specimen failed in static test.

^c Because of invalid curvature measurement, the flexural rigidity is estimated as the average of other four measurements.

F-8.2 Dynamic Tests

All Phase 1 CIRFT dynamic tests were completed except for one sample with pellet-to-pellet gaps. Six specimens were cycled in static mode before being tested dynamically using a process referred to as static/dynamic testing. The results from the static/dynamic tests are not strictly comparable with the other tests because some changes in the rod condition might have occurred during the static test. The zero mean strain CIRFT fatigue data (applied moment, cycles to failure, strain amplitude, and maximum stress amplitude, as discussed in Section F-3.1), maximum cladding stress amplitude (based on the modified equivalent stress approach in [F-4]), and dynamic flexural rigidity are provided in Table F-11. The nonzero mean strain fatigue data are provided in Table F-12. As discussed in Section F-8.1, the static specimens are tested in dynamic mode after the static test, but the dynamic results for these specimens are not strictly comparable with the dynamic-only test results. The results of the dynamic tests of these specimens are provided in Table F-11.

Figure F-10 plots the applied bending moment, with the number of cycles to failure measured for completed tests with the available previous data [F-4, F-5]. The stress and strain amplitudes can be plotted as functions of the number of cycles to failure to map the fatigue limits of the composite rods. Figure F-11 plots the strain amplitude as a function of the number of cycles to failure for tests where an extended analysis of the test data is available.

F-8.2.1 Uncertainty in Strain Amplitude and Flexural Rigidity

Following Montgomery [F-14], uncertainty is defined as twice the standard deviation of the expected value (i.e., 2σ). When there are multiple sources of variability in a value or that value is calculated from other known values, the standard error propagation method can be used to combine the 2σ uncertainties (Eq. G-1 in Montgomery [F-14]). The 2σ uncertainty in the strain amplitude and the flexural rigidity is then a combination of the uncertainty in the measured value and the variability in the measured value during the test. The variability during the test is calculated as part of the standard data processing after the test and is reported in Table F-13 as Test St.Dev for both strain amplitude and flexural rigidity. The uncertainty in the LVDT-based strain amplitude was previously calculated by Montgomery [F-14] but was recently directly determined by comparing strain amplitude calculated from the LVDTs to strain amplitude directly measured by a strain gauge attached to a calibration sample [F-15]. The 2σ uncertainty of the LVDT-based strain amplitude relative to the strain-gauge data is 0.022% [F-15] and is reported as Measurement Uncertainty for strain amplitude in Table F-13. However, the measurement uncertainty in the flexural rigidity value must still be calculated using the standard error propagation method defined in Montgomery [F-14]. To use the uncertainty in the strain measurement, the calculation has been updated using the relationship for flexural rigidity as a function of strain rather than curvature:

$$EI = \frac{\Delta M \times y_{max}}{\Delta \epsilon} . \quad (F-9)$$

Because ΔM and $\Delta \epsilon$ are maximum minus minimum, the 2σ uncertainty is the square root of the sum of squares for the uncertainty of the maximum and minimum values. Thus, for $\Delta \epsilon$, the 2σ uncertainty is $\sqrt{0.022^2 + 0.022^2} = 0.03\%$, and for ΔM , the 2σ uncertainty is $\sqrt{0.8^2 + 0.8^2} = 1.1\text{N-m}$, given the 2σ uncertainty of the applied moment is 0.8 N-m [F-14]. Assuming the uncertainty on the radius of the rod, $y_{max} = 4.75\text{ mm}$, is negligible compared with $\Delta \epsilon$ and ΔM , the 2σ measurement uncertainty for the flexural rigidity can be calculated for each test as

$$U_f = \sqrt{\left(\frac{-\Delta M y_{max}}{\Delta \epsilon^2}\right)^2 0.0003^2 + \left(\frac{y_{max}}{\Delta \epsilon}\right)^2 1.1^2} . \quad (F-10)$$

The results are reported as Measurement Uncertainty for flexural rigidity in Table F-13.

The total 2σ uncertainty is then the combination of both the variability in the test and the measurement uncertainty (using the square root of the sum of squares).

F-8.2.2 Comparisons Based on Stress Amplitude

In previous revisions of this Appendix, the fatigue data were plotted as a function of stress amplitude and compared with the O'Donnell-Langer design curve on the basis of stress, in addition to comparisons with the measured stress amplitudes and cycles measured during transportation tests (see Figure F-12 and Figure F-13). In Figure F-12, the stress amplitude is calculated based on the composite rod maximum stress per Eq. (F-7), and in Figure F-13, the stress amplitude is calculated as the maximum cladding stress. The purpose of these plots is to show that the expected stress amplitude is well below the design limit. As was previously noted, the sister rod data were on the lower side of the other lifetime estimates, and some data were below the O'Donnell-Langer fatigue curve.

In addition, while most of the data are consistent with previous data from other 17×17 rods, two specimens failed earlier than expected: 3A1F05-3214-3367 at 3450 cycles (LT Zirc-4 clad) and F35P17-3159-3312 at 773 cycles (Zirc-4 clad). At the tested rod elevations, both specimens have estimated oxide thicknesses of $\sim 130 \mu\text{m}$. Other specimens were tested from nearby elevations on both rods, but only one was tested at a similar load: 3A1F05-2025-2178 failed at 48,200 cycles but had a local oxide thickness of only $\sim 80 \mu\text{m}$. Other sister rod segments tested had oxide thicknesses of less than $70 \mu\text{m}$ (M5 and ZIRLO clad segments). For the Zirc-4 clad rod, the difference in performance could also be a result of the main geometric difference of the rods—the pellet length—and if so, further data analysis focused on pellet length could clarify the effect.

F-8.2.3 Comparisons Based on Strain Amplitude

A review of the O'Donnell-Langer fatigue design limit development process [F-8] illuminates that although the design limit includes the effect of non-zero mean stress, the data were generated at zero-mean stress. This prompted a second look at the sister rod fatigue evaluation and its approach, as discussed in Cantonwine et al. [F-12] and in this section.

First, Cantonwine et al. [F-12] addresses the benefit of plotting the fatigue data in terms of strain amplitude, as opposed to stress amplitude. Strain amplitude is concluded to be more appropriate because it is independent of the composite nature of the fuel rod, while stress can be calculated two different ways: (1) using the modified equivalent stress approach defined by Wang and Wang [F-4] to represent the cladding surface stress and (2) using the equivalent stress approach per Eq. (F-7). Further, strain is directly measured in the shipping tests that provide representative data for the expected applied fatigue cycles, which means it can be compared directly with the strain amplitude fatigue data.

Cantonwine et al. [F-12] also considered whether to calculate fatigue damage as the sum of the ratio of applied cycles to cycles-to-failure or to compare a conservative representation of the applied cycles with the fatigue limit (the fatigue limit is strain amplitude below which fatigue damage does not occur—typically taken at 10^7 cycles). It was concluded that it is inappropriate to calculate fatigue damage when the applied cycles are less than the fatigue limit because the fatigue curve must be extrapolated well beyond where there is fatigue data. Thus, the approach in [F-12] is to define a conservative fatigue limit based on the fatigue data reported herein and show that a conservative strain amplitude representing the fatigue cycles experienced in transportation [F-16] is below that limit.

The high burnup fuel rod fatigue data are plotted in Figure F-14 and are compared with the fatigue performance of cladding-only tubes, as reported in Section F-5 and open literature data on cladding alloys [F-8][F-1]. In Figure F-14, it can be clearly observed that the fatigue performance of high burnup fuel rods is degraded compared with fatigue of cladding-only test specimens and test coupons (see Section F-5 and O'Donnell-Langer [F-8]). The fatigue limit decreased from $\sim 0.20\%$ for the cladding alloys to $\sim 0.06\%$ for the high burnup fuel rods and is significantly lower than the O'Donnell-Langer design curve for zero-mean

strain conditions. As pointed out in Section F-3.2.2, discontinuities within the pellets and pellet-pellet interfaces are sources of stress/strain concentration, and it is concluded that these discontinuities in cladding support applied by the pellet are the cause of the observed degradation in fatigue performance. The magnitude of the stress/strain concentration can be estimated as the ratio of the fatigue limit for cladding alloys to that of the high burnup fuel rods ($0.20\%/0.06\% = 3.3$). To account for this degradation, a modification to the O'Donnell-Langer correlation was developed and is compared with the CIRFT data in Figure F-14. The proposed ORNL Fuel Rod Design Curve was defined using the same approach applied to cladding-only data by O'Donnell-Langer (i.e., decrease the strain amplitude by a factor of 2). The area below the proposed ORNL fatigue limit is the region where fatigue damage does not accumulate and is compared with the range of most limiting conditions observed in the multimodal transportation test (MMTT) shipping test [F-16], [F-17] (see Figure F-14).

However, even the proposed ORNL fatigue limit for fuel rods is potentially nonconservative because there will be a non-zero mean strain as a result of the rod-internal pressure and nominal rod bending during transportation resulting from gravity. To develop some understanding of the effect of nonzero mean strain, four unpressurized samples were tested under nonzero mean strain conditions defined in Table F-9 and reported in Table F-12. The nonzero mean strain data are lower than other data within the fuel rod database and near the ORNL Fuel Rod Design Curve for zero mean strain conditions (see Figure F-14). These data are ~40% less than the best estimate ORNL Fuel Rod Model, which is significantly larger than the 7% degradation predicted by Cantonwine et al. [F-12], suggesting they should be explicitly considered in the best estimate model and design curve as in the approach taken by O'Donnell-Langer for nonzero mean strain conditions [F-8].

As noted in Section F-8.2.2, the two samples with the largest oxide thickness (3A1F05-3214-3367 and F35P17-3159-3312) failed earlier than expected. To better understand whether oxide thickness (or hydrogen uptake) influences fatigue performance, the fraction of the residual to the predicted strain amplitude ((measured-predicted)/predicted) using the best estimate ORNL fuel rod model [F-12] is plotted as a function of oxide thickness in Figure F-15. The data seems indicate that once the oxide thickness increases above ~100 μm , the fatigue performance degrades beyond normal variability, though it is not expected that oxide thickness is the root cause.

Further study is needed to better quantify the potential effect of non-zero mean strain and large oxidation (or hydrogen) on fatigue performance.

F-8.2.4 CIRFT-Measured Flexural Rigidity of HBU Fuel Rods

Flexural rigidity is also measured during the dynamic test at the specific test conditions. The flexural rigidity of the specimen can change over the duration of the CIRFT test; a rod subjected to many bending cycles is expected to have a lower flexural rigidity than an uncycled rod, especially at large applied moments, and the rigidity reported herein is evaluated using data from the beginning of the test. The results of the dynamic flexural rigidity measurements are provided in Table F-11. For one of the static tests (3D8E14-0719-0872), the data required to calculate the curvature, strain, and flexural rigidity were unavailable, so the data are estimated as the average of the other static tests. The flexural rigidity measured for the sister rod specimens is plotted as a function of the estimated specimen burnup in Figure F-16, along with the measured flexural rigidity of other 17×17 rods tested at ORNL using CIRFT [F-4], [F-18]; there is no observed trend with burnup. The flexural rigidity (was also evaluated as a function of the applied bending moment (Figure F-17) and the decreasing trend are consistent with previous data. Because of the large uncertainties in the tests at low applied moment and because all the samples at high applied moment were tested statically before dynamic testing, only the samples tested at applied moments between 8 and 14 N-m are used in calculating the average dynamic flexural rigidity, which is 27 N-m^2 .

Table F-11. Sister Rod CIRFT Test Results at Zero Mean Strain

Cladding material	Estimated specimen-average burnup (GWd/MTU)	Oxide Thickness (μm) ^a	Specimen ID	Curvature (1/m)	Cycles to failure	Applied moment (N-m) (± 0.8 N-m)	Maximum Average Stress ^b (MPa) (± 10.7 MPa)	Maximum Cladding Stress ^c (MPa)	Strain Amplitude (%)	Dynamic flexural rigidity (N-m ²)
M5	58	4	30AD05-0697-0850 ^d	1.0 ± 0.18	3,368	15.8	186.0	437	0.47	15.6
M5	59	7	30AD05-2050-2203	0.18 ± 0.10	133,000	5.1	61.9	76	0.08	28.7
M5	59	10	30AD05-2630-2783	0.38 ± 0.11	22,300	10.7	129.6	164	0.18	28.0
M5	56	4	30AE14-0672-0825 ^{d,e}	0.76 ± 0.15	1,630	15.6	187.0	328	0.36	20.5
M5	60	18	30AE14-2850-3003 ^e	0.46 ± 0.11	9,800	10.6	127.0	193	0.22	23.6
M5	56	23	30AE14-3156-3309 ^e	0.21 ± 0.10	113,000	5.0	59.5	92	0.10	23.2
Zirc-4	66	75	F35P17-2027-2180 ^e	0.15 ± 0.10	1,340,000	4.0	47.8	66	0.07	26.8
Zirc-4	62	130	F35P17-3159-3312 ^{e,f}	0.32 ± 0.10	773	8.6	101.0	122	0.15	30.7
LT Zirc-4	48	130	3A1F05-3214-3367	0.41 ± 0.11	3,450	8.8	105.9	178	0.19	21.6
LT Zirc-4	56	65	3A1F05-1853-2006 ^d	0.82 ± 0.16	1,300	15.9	191.5	357	0.39	19.3
LT Zirc-4	56	85	3A1F05-2025-2178	0.38 ± 0.11	48,200	8.8	105.9	165	0.18	23.2
LT Zirc-4	44	110	3A1F05-3367-3520	0.14 ± 0.09	214,000	4.0	48.6	59	0.06	29.7
ZIRLO	64	8	3D8E14-0719-0872 ^d	$0.58^2 \pm 0.12$	9,589	15.3	181.0	362	0.39 ^g	18.4 ^g
ZIRLO	64	30	3D8E14-2412-2565 ^h	0.18 ± 0.10	191,000	5.0	60.1	70	0.08	31.3
ZIRLO	62	50	3D8E14-2963-3116	0.31 ± 0.10	39,700	8.7	104.2	136	0.15	28.1
ZIRLO	63	12	3D8E14-1178-1331	0.16 ± 0.10	212,000	4.9	58.4	69	0.08	30.9
ZIRLO	59	5	3F9N05-0719-0872 ^{d,e}	0.86 ± 0.16	3,540	15.5	186.3	374	0.41	18.0
ZIRLO	59	25	3F9N05-2329-2482 ^e	0.21 ± 0.10	189,000	4.8	57.3	92	0.10	22.6
ZIRLO	57	40	3F9N05-2710-2863 ^e	0.40 ± 0.11	33,000	8.7	104.7	173	0.19	21.8
ZIRLO	59	17	6U3K09-2310-2463	0.42 ± 0.11	17,500	12.7	152.3	182	0.20	30.2
ZIRLO	59	22	6U3K09-2463-2616	0.27 ± 0.10	39,200	8.9	106.5	119	0.13	32.4
ZIRLO	58	24	6U3K09-2635-2788	0.17 ± 0.10	110,000	6.4	76.8	75	0.08	37.1
ZIRLO	50	33	6U3K09-3200-3353	0.31 ± 0.10	34,900	8.8	105.3	127	0.15	30.0
ZIRLO	46	30	6U3K09-3353-3506	0.43 ± 0.11	14,100	11.7	140.2	187	0.21	27.0

^a Oxide thickness is estimated from liftoff in Montgomery et al. [F-11].

^b Stress calculated using the equivalent stress approach per Eq. (F-7). Measured ODs used in calculation were typically approximately 9.5 mm.

^c Stress calculated using the modified equivalent stress approach in Reference [F-4] to represent the cladding surface stress.

^d Dynamically tested following a static test.

^e Specimen from heat-treated rod.

^f Erratic load cell data were recorded during the test. The applied moment might have been higher.

^g Estimated based on average flexural rigidity of valid static/dynamic tests.

^h Specimen had a GTRF mark in the gauge section that was aligned (as was possible) with the expected maximum strain location.

Table F-12. Sister Rod CIRFT Test Results at Non-zero Mean Strain

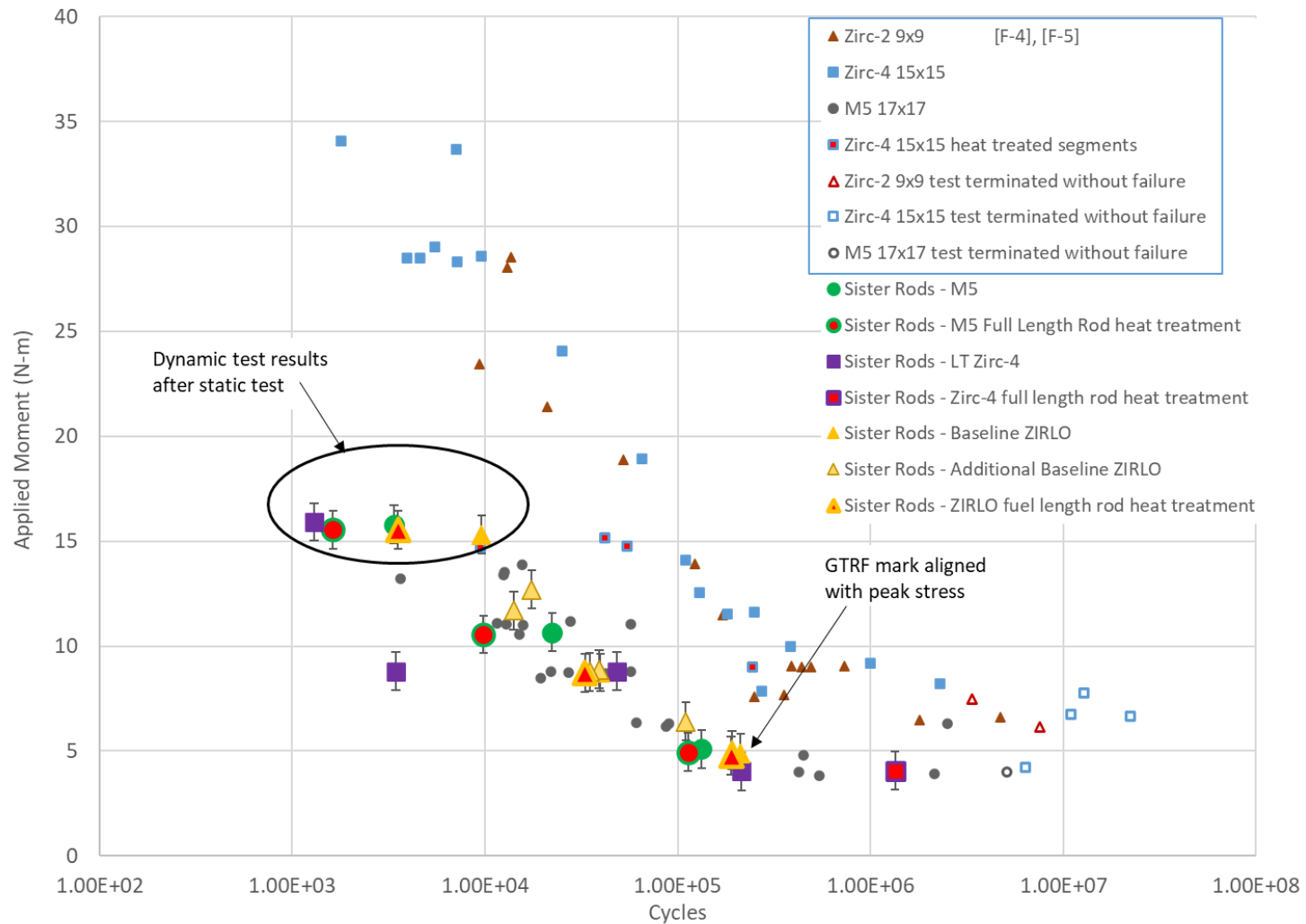
Cladding material	Specimen ID	Max/Min Curvature (1/m)	Cycles to Failure	Max/Min Strain (%)	Strain Amplitude (%)	Mean Strain (%)	Max/Min Applied Moment (N-m) (± 0.8 N-m)	Max/Min Maximum Average Stress ^a (MPa) (± 10.7 MPa)	Maximum Cladding Stress ^b (MPa)	Dynamic Flexural Rigidity (N-m ²)
ZIRLO	3F9N05-3440-3593	0.23/-0.007	280000	0.111/-0.003	0.057	0.054	5.4/-1.2	65.0/-14.1	101	27.4
ZIRLO	3D8E14-3225-3378	0.16/-0.034	352000	0.077/-0.016	0.047	0.031	5.8/-0.47	69.8/-5.6	71	32.1
Zirc-4	F35P17-3312-3465	0.20/0.053	188000	0.093/-0.025	0.059	0.034	6.4/0.47	75.0/-5.6	85	27.5
M5	30AE14-3003-3156	0.18/-0.017	315000	0.088/-0.008	0.048	0.040	6.5/-0.74	78.6/-9.0	80	28.6

^a Stress calculated using the equivalent stress approach per Eq. (F-7). Measured ODs used in calculation were typically ~9.5 mm.

^b Stress calculated using the modified equivalent stress approach in Reference [F-4] to represent the cladding surface stress.

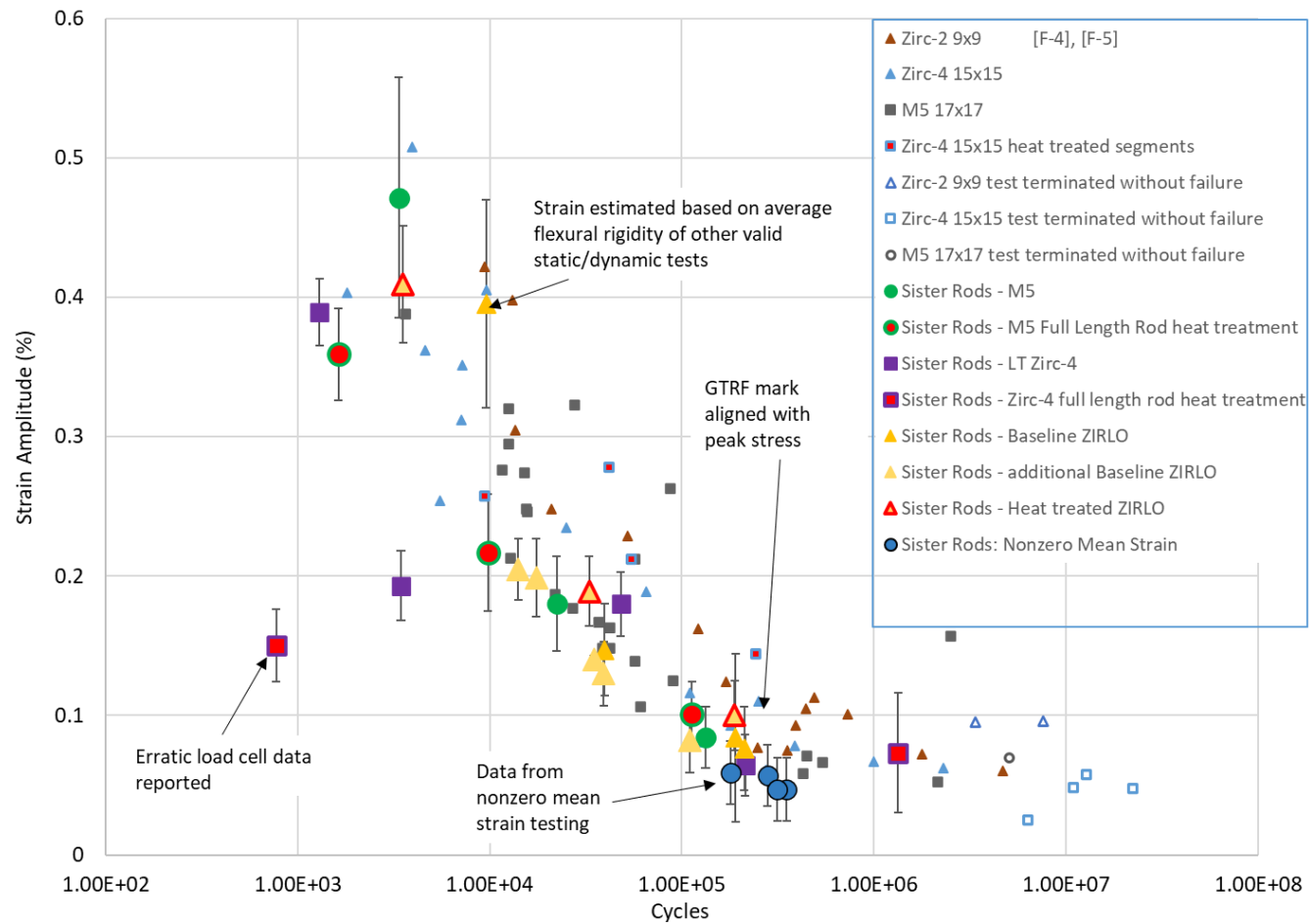
Table F-13. Strain Amplitude and Flexural Rigidity with Test and Measurement Variability Used to Calculate Uncertainty

Cladding Material	Specimen ID	Strain Amplitude				Dynamic Flexural Rigidity			
		Strain Amplitude	Test St.Dev.	Measurement Uncertainty	Total Uncertainty	Dynamic Flexural Rigidity	Test St.Dev.	Measurement Uncertainty	Total Uncertainty
		(%)	(%)	(%)	(%)	(N-m ²)	(N-m ²)	(N-m ²)	(N-m ²)
M5	30AD05-0697-0850 ^a	0.47				15.6			
M5	30AD05-2050-2203	0.08	0.002	0.022	0.022	28.7	0.5	6.5	6.6
M5	30AD05-2630-2783	0.18	0.013	0.022	0.034	28	0.6	2.8	3.0
M5	30AE14-0672-0825	0.36	0.012	0.022	0.033	20.5	0.8	1.1	2.0
M5	30AE14-2850-3003	0.22	0.018	0.022	0.042	23.6	8	2.0	16.1
M5	30AE14-3156-3309	0.1	0.003	0.022	0.023	23.2	0.5	4.4	4.5
Zirc-4	F35P17-2027-2180	0.07	0.007	0.022	0.026	26.8	2.9	6.9	9.0
Zirc-4	F35P17-3159-3312	0.15	0.046	0.022	0.095	30.7	11.7	3.2	23.6
LT Zirc-4	3A1F05-3214-3367	0.19	0.006	0.022	0.025	21.6	0.9	2.2	2.9
LT Zirc-4	3A1F05-1853-2006	0.39	0.005	0.022	0.024	19.3	0.1	1.0	1.0
LT Zirc-4	3A1F05-2025-2178	0.18	0.004	0.022	0.023	23.2	0.4	2.4	2.5
LT Zirc-4	3A1F05-3367-3520	0.06	0.002	0.022	0.022	29.7	0.9	9.0	9.2
ZIRLO	3D8E14-0719-0872	0.39	-	-	-	18.4 ^b	-	-	-
ZIRLO	3D8E14-2412-2565	0.08	0.028	0.022	0.060	31.3	9.3	6.5	19.7
ZIRLO	3D8E14-2963-3116	0.15	0.012	0.022	0.033	28.1	2.2	3.3	5.5
ZIRLO	3D8E14-1178-1331	0.08	0.01	0.022	0.030	30.9	1.6	6.4	7.1
ZIRLO	3F9N05-0719-0872	0.41	0.018	0.022	0.042	18	0.8	0.9	1.8
ZIRLO	3F9N05-2329-2482	0.1	0.006	0.022	0.025	22.6	0.7	4.3	4.5
ZIRLO	3F9N05-2710-2863	0.19	0.006	0.022	0.025	21.8	0.7	2.2	2.6
ZIRLO	6U3K09-2310-2463	0.2	0.009	0.022	0.028	30.2	1.1	2.6	3.4
ZIRLO	6U3K09-2463-2616	0.13	0.003	0.022	0.023	32.4	0.4	4.3	4.3
ZIRLO	6U3K09-2635-2788	0.08	0.004	0.022	0.023	37.1	1.5	7.8	8.4
ZIRLO	6U3K09-3200-3353	0.14	0.003	0.022	0.023	30	2.3	3.3	5.7
ZIRLO	6U3K09-3353-3506	0.21	0.002	0.022	0.022	27	0.3	2.3	2.3
ZIRLO	3F9N05-3440-3593	0.057	0.002	0.022	0.022	27.4	0.6	8.6	8.7
ZIRLO	3D8E14-3225-3378	0.047	0.002	0.022	0.023	32.1	1.8	12.2	12.7
Zirc-4	F35P17-3312-3465	0.059	0.002	0.022	0.022	27.5	1.3	8.1	8.5
M5	30AE14-3003-3156	0.048	0.002	0.022	0.022	28.6	1.1	11.7	11.9



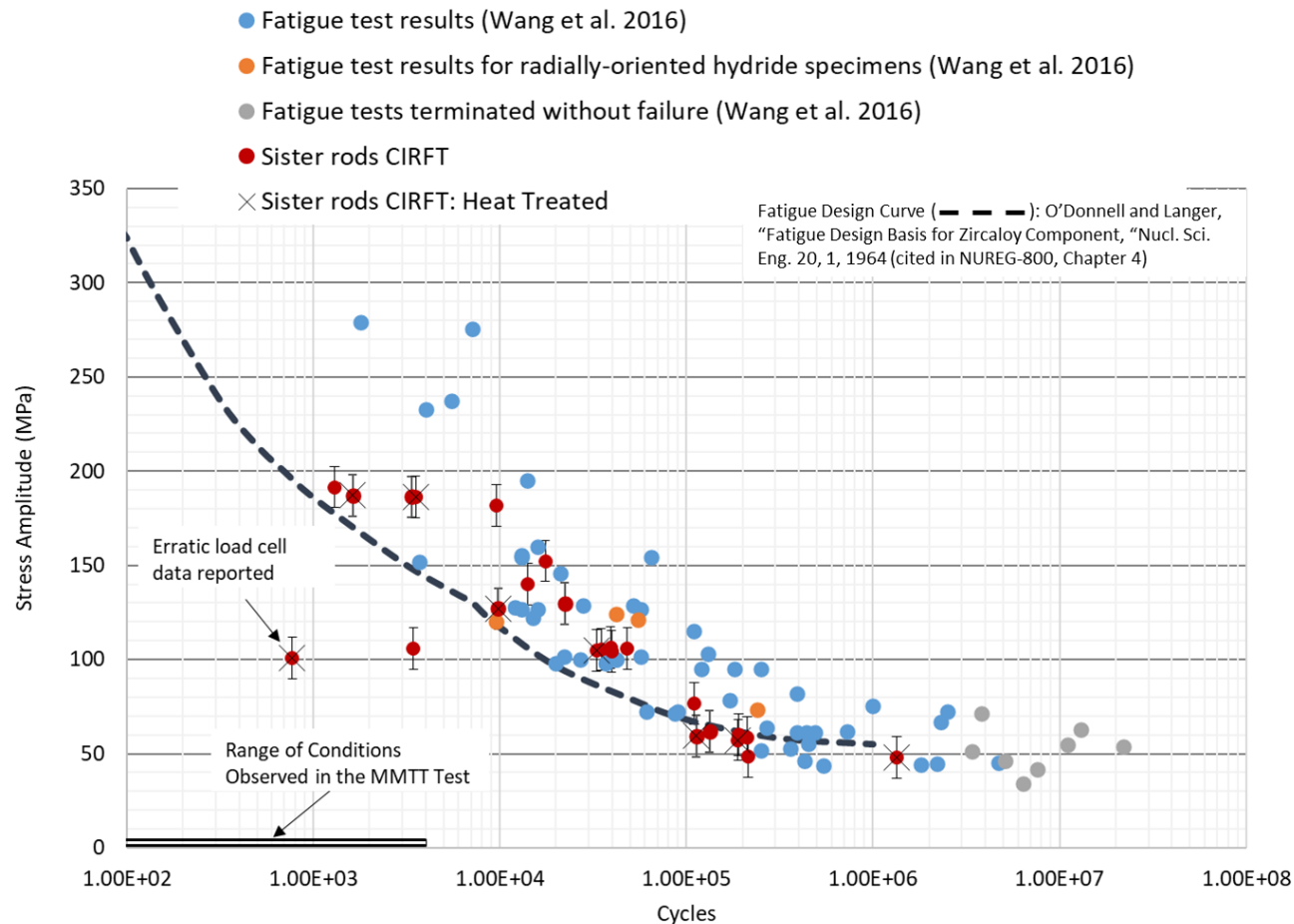
The error bars on the sister rod data represent the calculated uncertainty (0.8 N-m) in Section G-3.3, Appendix G (nonsister rod data from [F-4], [F-5])

Figure F-10. Results of zero mean strain CIRFT tests plotted with reference data, applied moment vs. cycles to failure.



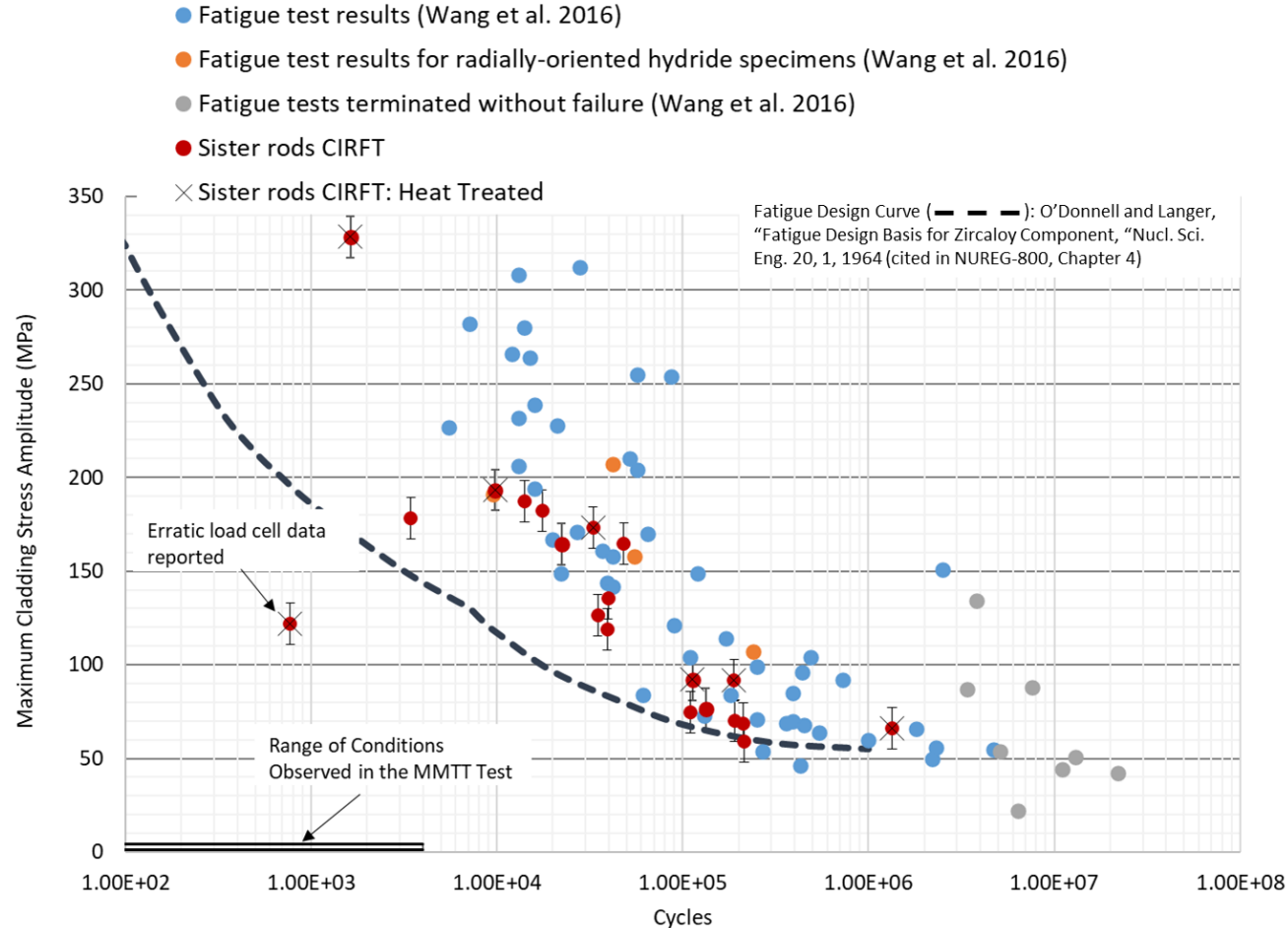
The error bars on the sister rod data represent the calculated uncertainty provided in Table F-13.

Figure F-11. Results of zero and non-zero mean strain CIRFT tests completed to date, strain amplitude vs. cycles to failure.



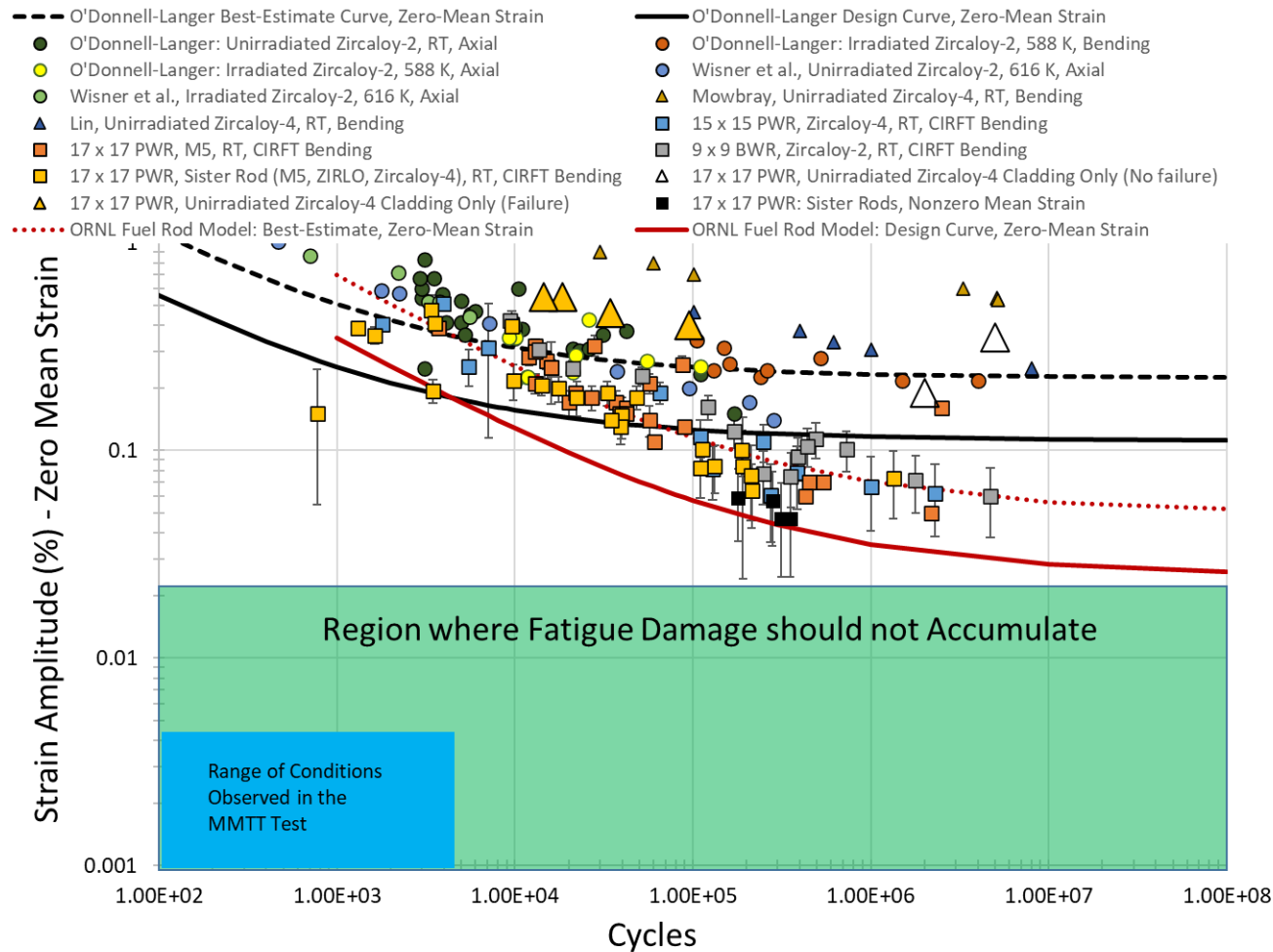
The error bars on the sister rod data represent the calculated uncertainty in Section G-3.5, Appendix G.

Figure F-12. Stress amplitude of the composite rod based on Eq. (F-7) as a function of cycles to failure for the sister rods. The stresses representing the conditions observed in the MMTT test are calculated based on measured strains: 1 MPa for the lower strain of 0.001% (or 10 μ strain), which is the minimum strain of the highest 4,000 cycles observed, and 4.2 MPa for the upper strain of 0.0042% (or 42 μ strain), which is the maximum strain observed during testing at the Transportation Technology Center, Inc. [F-16], [F-17].



The error bars on the sister rod data represent the calculated uncertainty in Section G-3.5, Appendix G.

Figure F-13. Cladding stress amplitude as a function of cycles to failure for the sister rods. The stresses representing the conditions observed in the MMTT test are calculated based on measured strains: 1 MPa for the lower strain of 0.001% (or 10 μ strain), which is the minimum strain of the highest 4,000 cycles observed, and 4.2 MPa for the upper strain of 0.0042% (or 42 μ strain), which is the maximum strain observed during testing at the Transportation Technology Center, Inc.[F-16], [F-17].



The error bars on the sister rod data represent the 2σ uncertainty provided in Table F-13.

Figure F-14. Strain amplitude as a function of cycles to failure for the sister rods compared with the fatigue data on cladding alloys from Figure F-7 and the proposed ORNL fatigue limit for fuel rods. [F-12] The strains representing the conditions observed in the MMTT test are based on measured strains: the lower strain is 0.001% (or 10 μ strain), which is the minimum strain of the highest 4000 cycles observed, and the upper strain is 0.0042% (or 42 μ strain), which is the maximum strain observed during testing at the Transportation Technology Center, Inc. [F-16], [F-17].

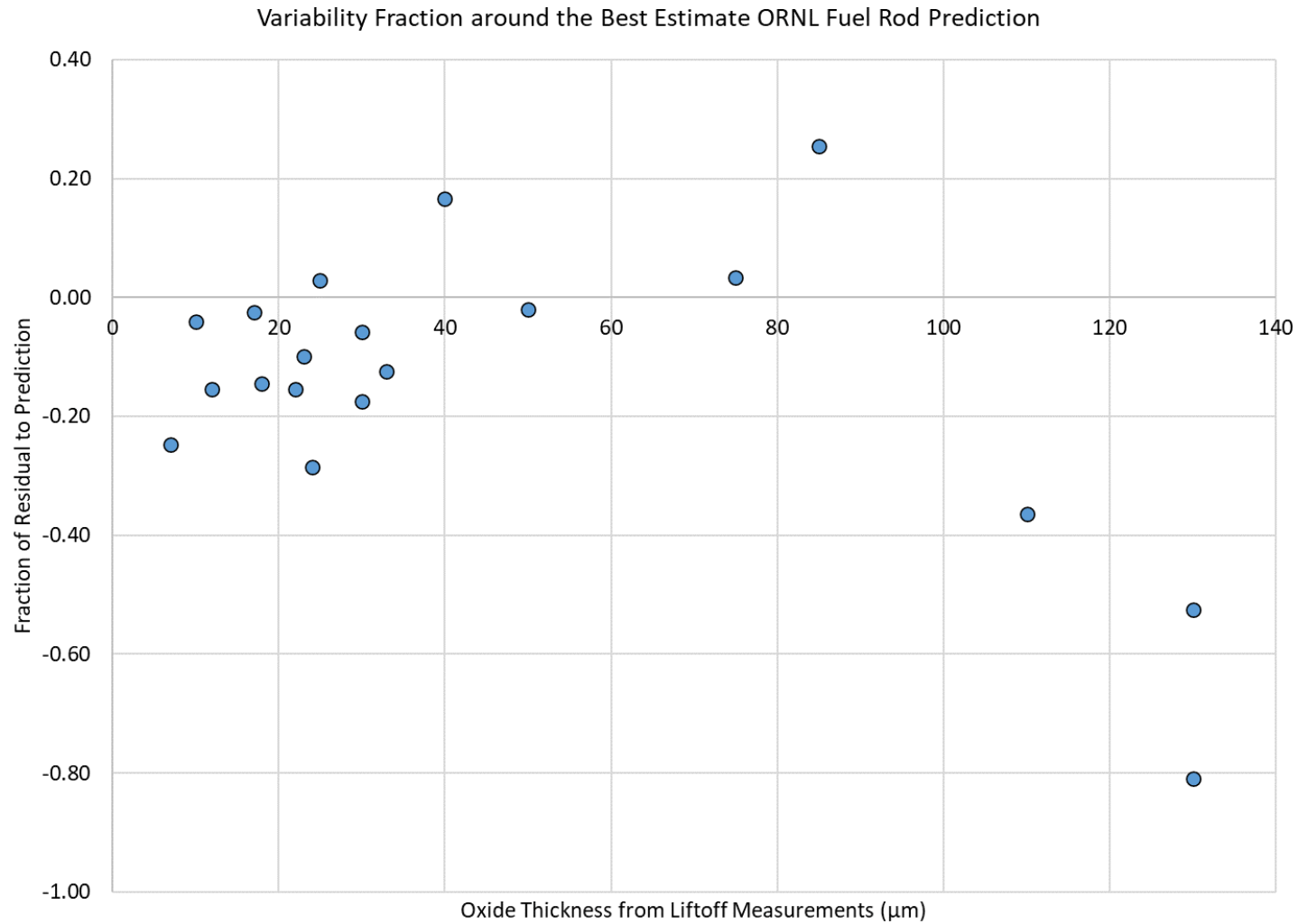


Figure F-15. The fraction of the residual to the ORNL fuel rod model best-estimate predicted strain amplitude ((measured-predicted)/predicted) for the zero mean strain fatigue data as a function of the oxide thickness estimated from the liftoff measurement in Montgomery et al. [F-11].

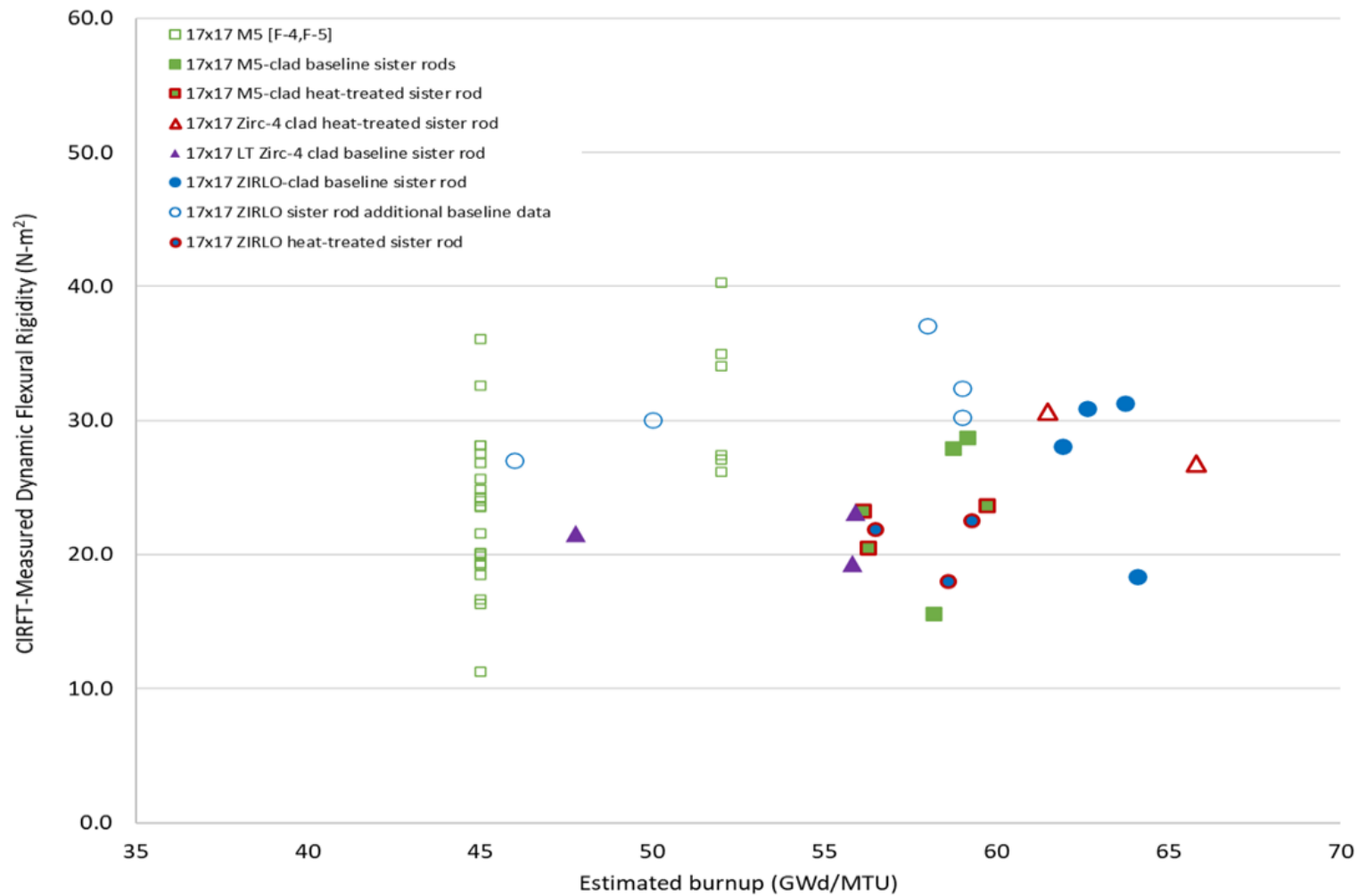
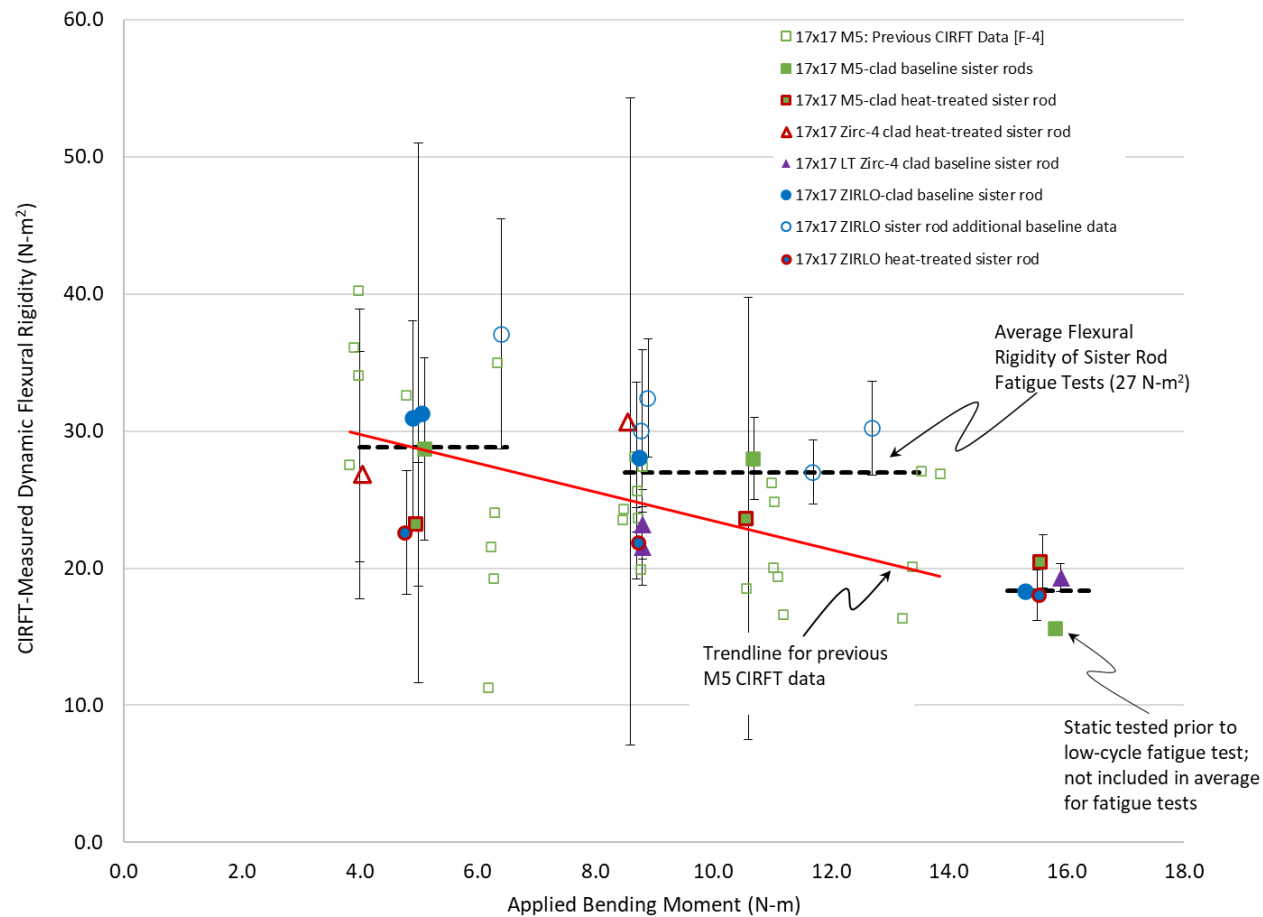


Figure F-16. CIRFT-measured flexural rigidity of the sister rod segments tested as a function of estimated segment burnup plotted with previous CIRFT data.



The error bars on the sister rod data represent the 2σ uncertainty provided in Table F-13.

Figure F-17. Trend of CIRFT-measured dynamic flexural rigidity with applied bending moment.

F-8.3 Comparisons of Paired Specimens

The paired results are tabulated in Table F-14. Averages are provided for burnup, cycles to failure, strain, and flexural rigidity for comparison purposes. For the M5-clad and ZIRLO-clad segments, the heat-treated rods generally have a shorter fatigue lifetime and lower flexural rigidity. Revisiting Figure F-16, the small but consistent difference in flexural rigidity between the baseline and heat-treated rods is clear. The reverse seems to be true for the Zirc-4-clad and LT Zirc-4-clad pairs; the heat-treated Zirc-4-clad segments have a higher flexural rigidity and a longer fatigue lifetime than the baseline LT Zirc-4-clad segments. However, there are several differences in the parent rods, and these two rods are not good matches for comparing heat-treatment effects. One potential explanation for the difference in performance is the pellet length. As shown in Table 4 of the NDE report [F-11], the pellets in the Zirc-4-clad rod are ~13.6 mm long, whereas the pellets in all other sister rods are ~10 mm long. The increased stiffness is possibly related to the longer pellet length.

Figure F-10 further illustrates a reduced fatigue lifetime related to the heat treatments. This effect is seen for all M5-clad and ZIRLO-clad heat-treated specimens. However, when the cycles to failure are plotted with the calculated strain amplitude, the offset related to the heat treatment is eliminated, as shown in Figure F-11. Because the rods have nearly the same geometry, the calculated strain would normally be expected to provide the same offset between baseline and heat-treated specimen results. However, for CIRFT, the strain is calculated based on the measured rod deflection and flexural rigidity. Because the heat-treated rods have a lower flexural rigidity, the stress and strain corresponding to the same bending moment are higher. Thus, plotting the fatigue lifetime by strain amplitude resolves the offset, and the heat-treated specimen's fatigue lifetime is consistent with the baseline specimen's performance given the same amount of applied stress and strain.

On the basis of the CIRFT rigidity measurements alone, as shown in Figure F-16, the observed difference between the heat-treated and baseline could be considered within measurement uncertainty. However, given the good alignment of the strain-amplitude results and the results of mechanical tests (Appendix E), the heat treatments clearly resulted in a lower flexural rigidity that led to a shorter fatigue lifetime for the same applied load. At least three potential sources are possible for a reduction in flexural rigidity with FHT: (1) a permanent increase in cladding OD and a pellet-cladding gap that resulted from the increased pressure at temperature during the heat treatment, (2) annealing of irradiation defects resulting from the FHT, and (3) reorientation of precipitated hydrides in the cladding during the heat treatment that make it more susceptible to cladding fracture. The latter source is unlikely because the amount of hydride reorientation resulting from the sister rod heat treatments (Appendices A and B) varied by cladding alloy; only very short, reoriented hydrides were observed on the Zirc-4/LT Zirc-4-clad rods, isolated hydrides were observed at the ID/OD on the ZIRLO-clad rods, and many reoriented hydrides were observed on the M5-clad rods. Because reorientation was not observed for all heat-treated rods, the difference in flexural rigidity and fatigue lifetime is not likely to be related to hydride reorientation. However, irradiation defect annealing could have occurred during FHT (particularly on the M5-clad rod, as discussed in Appendix A), resulting in a lower overall rigidity of the FHT rod, leading to a shorter fatigue lifetime. The other two potential sources are being investigated.

One specimen with visible GTRF marks was tested with the marks aligned (as was possible) with the highest cladding strain location, and the GTRF marks did not reduce the fatigue lifetime. The GTRF marks on this specimen are not considered representative or bounding; the specimen was selected based on availability only, and further tests should be completed to fully explore the effect.

Table F-14. Results Arranged by Paired Specimens (Baseline Rods vs. Heat-Treated Rods) for Static/Dynamic and Dynamic CIRFT.

Baseline rods								Heat-treated rods							
Specimen ID			Cladding type	Estimated specimen average burnup (GWd/MTU)	Cycles to failure	Dynamic flexural rigidity (N-m ²)	Applied strain amplitude (%)	Specimen ID			Cladding type	Estimated specimen average burnup (GWd/MTU)	Cycles to failure	Dynamic flexural rigidity (N-m ²)	Applied strain amplitude (%)
30AD05 0697 0850 ^a	M5	58	3,368	15.6	0.47	30AE14 0672 0825 ^a	M5	56	1,630	20.5	0.36				
30AD05 2050 2203		59	133,000	28.7	0.08	30AE14 3156 3309		56	113,000	23.2	0.10				
30AD05 2630 2783		59	22,300	28.0	0.18	30AE14 2850 3003		60	9,800	23.6	0.22				
Average				59	52,889	24.1	0.24					57	41,477	22.4	0.23
3A1F05 1853 2006 ^a	LT Zirc-4	56	1,300	19.3	0.39	F35P17 1855 2008 ^{a,b,c}	Zirc-4	53	525	28.7 ^d	0.16 ^d				
3A1F05 3367 3520		44	214,000	29.7	0.06	F35P17 2027 2180		52	1,340,000	26.8	0.07				
3A1F05 2025 2178		56	48,200	23.2	0.18										
3A1F05 3214 3367		48	3,450	21.6	0.19	F35P17 3159 3312 ^b		47	773	30.7	0.15				
Average				51	66,738	24.8	0.14					51	447,099	28.8	0.11
3D8E14 0719 0872 ^a	ZIRLO	64	9,589	18.4 ^d	0.39 ^d										
3D8E14 2412 2565 ^e		64	191,000	31.3	0.08										
3D8E14 2963 3116		62	39,700	28.1	0.15										
3D8E14 1178 1331		63	212,000	30.9	0.08										
6U3K09 2310 2463		59	17,500	30.2	0.20	3F9N05 0719 0872 ^a	ZIRLO	59	3,540	18.0	0.41				
6U3K09 2463 2616		59	39,200	32.4	0.13	3F9N05 2329 2482		59	189,000	22.6	0.10				
6U3K09 2635 2788		58	110,000	37.1	0.08	3F9N05 2710 2863		57	33,000	21.8	0.19				
6U3K09 3200 3353		50	34,900	30.0	0.15										
6U3K09 3353 3506		46	14,100	27.0	0.21										
Average zero mean tests				60	50,400	31.4	0.15					58	75,180	21.8	0.19
Non-zero mean strain tests															
3D8E14 3225 3378	ZIRLO		352,000	32.1	0.08	3F9N05 3440 3593	ZIRLO		280,000	27.4	0.06				
						F35P17 3312 3465	Zirc-4		188,000	27.5	0.06				
						30AE14 3003 3156	M5		315,000	28.6	0.05				

^a Dynamically tested following a static test.

^b Erratic load cell data were recorded during the test. The applied moment and strain amplitude were likely higher.

^c Deeper examination indicates that this specimen broke during the static test; therefore, the dynamic test results are invalid.

^d Estimated.

^e Specimen had a GTRF mark in the gauge section that was aligned (as possible) with the expected maximum strain location.

F-8.4 Optical Imaging of the Fractured Specimens

To provide additional information regarding how the specimens fractured, magnified images were obtained using the Irradiated Microsphere Gamma Analyzer facility at the Irradiated Fuels Examination Laboratory. The images (Figure F-18 through Figure F-41) provide information about the location where the fatigue crack propagated to fracture and about whether the fracture occurred at a pellet-pellet interface.

In many cases, the locations of the highest strains appear on the specimen surface as dull oval areas, as shown in Figure F-19. Rods with higher oxide thicknesses had some additional spalling during the test, which is particularly visible in LT Zirc-4-clad rods such as 3A1F05-1853-2006 (Figure F-32).

The M5-clad specimens tended to break cleanly around the circumference of the rod, but the break occurred in the body of the pellet, rather than at the pellet-pellet interface. Three of the six specimens broke in the center third of the specimen, whereas the other three broke near or inside a dogbone grip.

The ZIRLO-clad specimens broke differently, depending on the parent rod. The baseline 3D8E14 specimens tended to break cleanly around the circumference of the rod but at an ~30-degree angle. Three of the four specimens broke at pellet-pellet interfaces, and the cladding fracture extended into the body of a pellet. Three of the four specimens broke in the center third, and one broke near the dogbone. All 6U3K09 specimens broke circumferentially: three of the five broke near or inside the dogbone grip, and three of the five broke at pellet-pellet interfaces. Two of the 6U3K09 specimens had double fractures—a partial circumference break in the center third, with the full fracture near the dogbone. All specimens from FHT rod 3F9N05 broke in the center third of the specimen: two had a flat circumferential break at the pellet-pellet interface, and one broke in the body of a pellet at an ~30-degree angle.

The Zirc-4-clad specimens all broke dramatically in the same way, with a flat circumferential crack around half the rod that was sheared around the half the rod and at a pellet-pellet interface. One specimen fractured in the center third of the dogbone, and two fractured near the dogbone grip. The Zirc-4-clad fractures are jagged, and the sheared sections span a full pellet length or more, although the crack appears to have nucleated at a pellet-pellet interface. The baseline LT Zirc-4-clad specimens look similar to the LT Zirc-4 specimens at higher rod elevations, and at lower elevations they also look similar to the ZIRLO rods. Two baseline LT Zirc-4-clad specimens fractured in the center third of the specimen, and three fractured at pellet-pellet interfaces.

There does not appear to be a difference in the fracture mode of the baseline and heat-treated rods. The specimens with lower-than-expected fatigue lifetimes did not fracture in an anomalous manner.

Table F-15 summarizes the visual observations of CIRFT-fractured dogbones.

Table F-15. Summary of Visual Observations of CIRFT-Fractured Dogbones.

Rod type	Cladding material	Estimated specimen-average burnup (GWd/MTU)	Specimen ID	Fracture location	Cladding fracture orientation	Pellet fracture appearance
17×17	M5	58	30AD05-0697-0850	Center third	Circumferential	Pellet body
17×17	M5	59	30AD05-2050-2203	In grip	Circumferential	Pellet body
17×17	M5	59	30AD05-2630-2783	Near grip	Circumferential with some flaring and uneven ends	Pellet body but very near end
17×17	M5	56	30AE14-0672-0825	Center third	Circumferential with some flaring and uneven ends	Pellet body
17×17	M5	60	30AE14-2850-3003	Near grip	Circumferential	Pellet body
17×17	M5	56	30AE14-3156-3309	Center third	Circumferential with partial shearing	Pellet body
17×17	Zirc-4	66	F35P17-1855-2008	Center third	Partially sheared	At pellet end and through body
17×17	Zirc-4	66	F35P17-2027-2180	Near grip	Partially sheared	At pellet end
17×17	Zirc-4	62	F35P17-3159-3312	Near grip	Partially sheared	At pellet end
17×17	LT Zirc-4	48	3A1F05-3214-3367	In grip	Partially sheared	Pellet end
17×17	LT Zirc-4	56	3A1F05-1853-2006	Near grip	Circumferential at ~30-degree angle	Just off pellet end
17×17	LT Zirc-4	56	3A1F05-2025-2178	Center third	circumferential	Pellet end
17×17	LT Zirc-4	44	3A1F05-3367-3520	Center third	Partially sheared	Pellet body
17×17	ZIRLO	64	3D8E14-0719-0872	Near grip	Circumferential with partial shearing	Pellet end
17×17	ZIRLO	64	3D8E14-2412-2565	Center third	Circumferential at ~30-degree angle	Pellet body
17×17	ZIRLO	62	3D8E14-2963-3116	Center third	circumferential	Pellet end
17×17	ZIRLO	63	3D8E14-1178-1331	Center third	Circumferential. GTRF mark obliterated.	Pellet end
17×17	ZIRLO	59	3F9N05-0719-0872 ³	Center third	Circumferential at ~30-degree angle	Pellet body
17×17	ZIRLO	59	3F9N05-2329-2482	Center third	Circumferential	Pellet end
17×17	ZIRLO	57	3F9N05-2710-2863	Center third	Circumferential	Pellet end
17×17	ZIRLO	59	6U3K09-2310-2463	Center and near grip; double fracture	Circumferential	Pellet end
17×17	ZIRLO	59	6U3K09-2463-2616	Near grip	Circumferential	Pellet end
17×17	ZIRLO	58	6U3K09-2635-2788	At grip	Circumferential	Pellet end
17×17	ZIRLO	50	6U3K09-3200-3353	Center third and near grip, double fracture	Circumferential	Pellet body
17×17	ZIRLO	46	6U3K09-3353-3506	Near grip	Circumferential	Pellet body

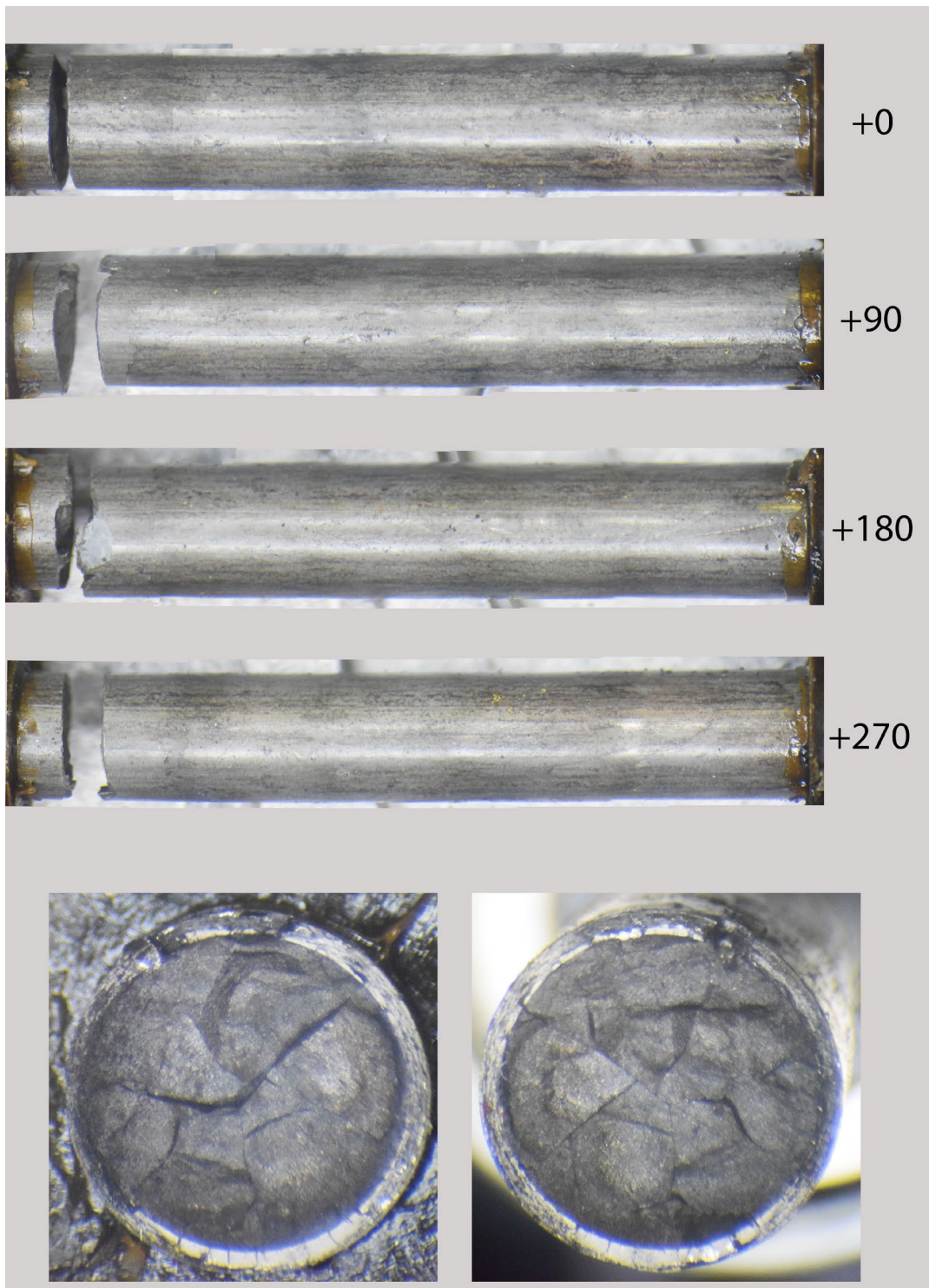


Figure F-18. 6U3K09-3353-3506 post-fatigue test condition.

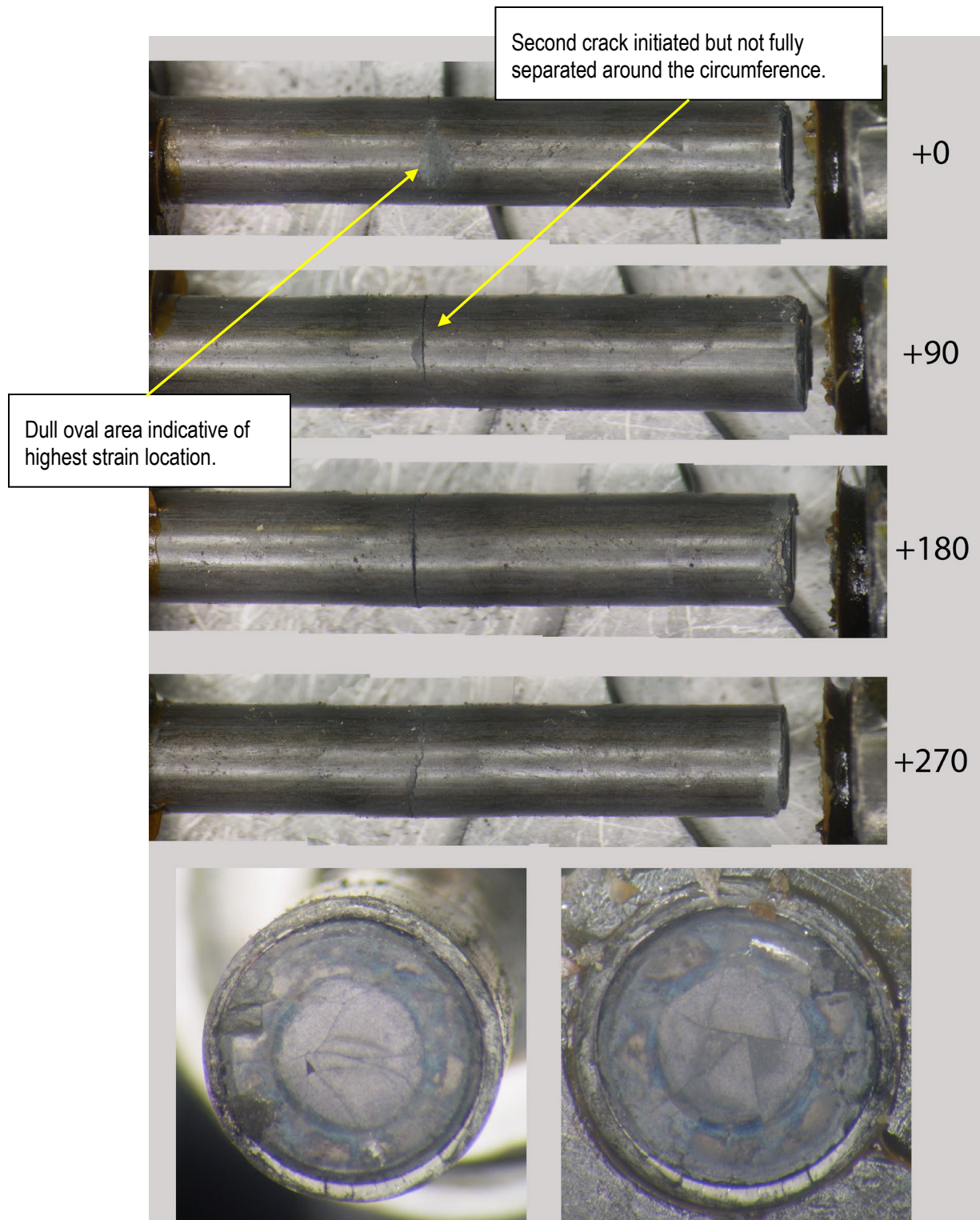


Figure F-19. 6U3K09-2310-2463 post-fatigue test condition.

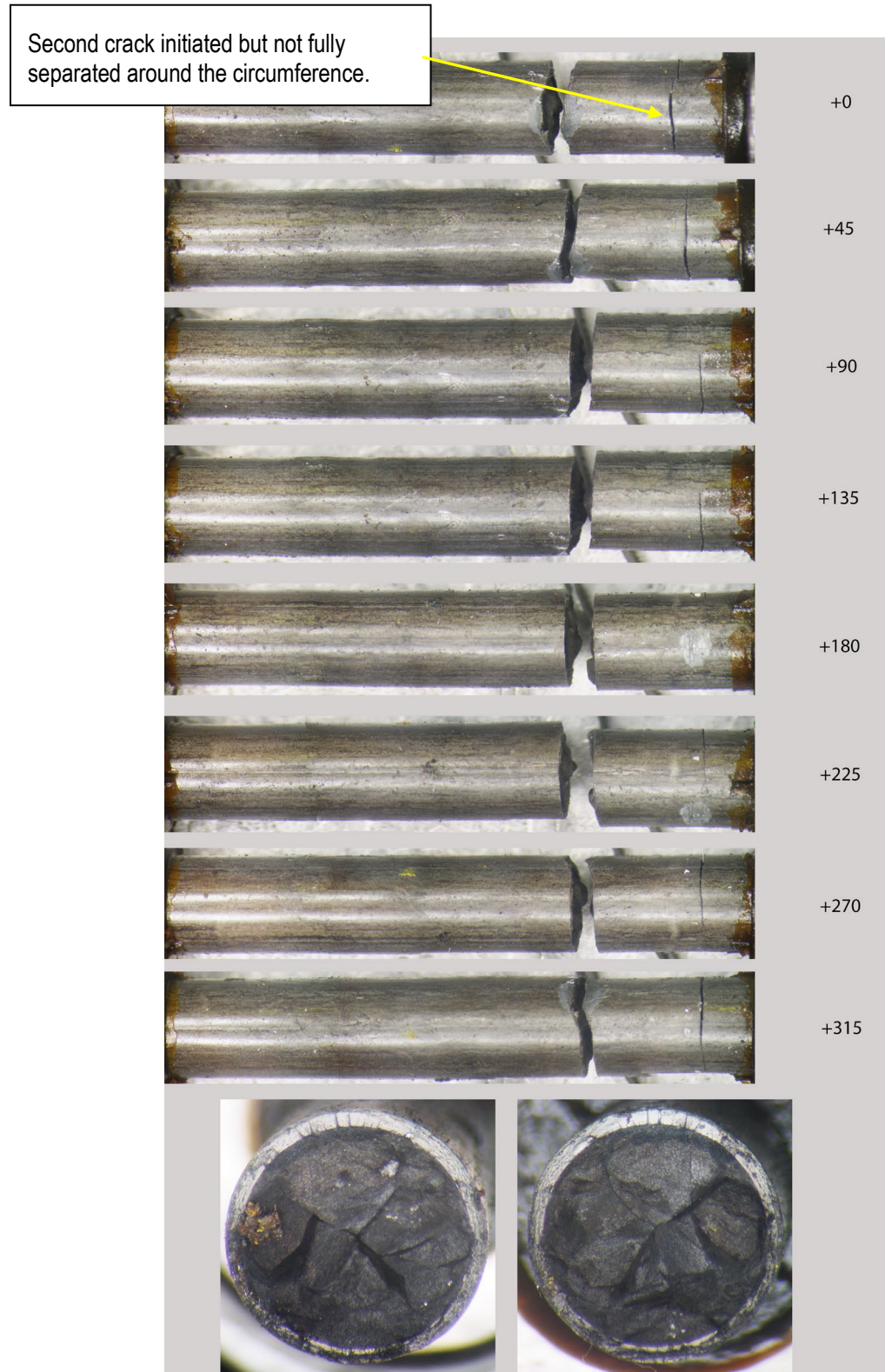


Figure F-20. 6U3K09-3200-3353 post-fatigue test condition.

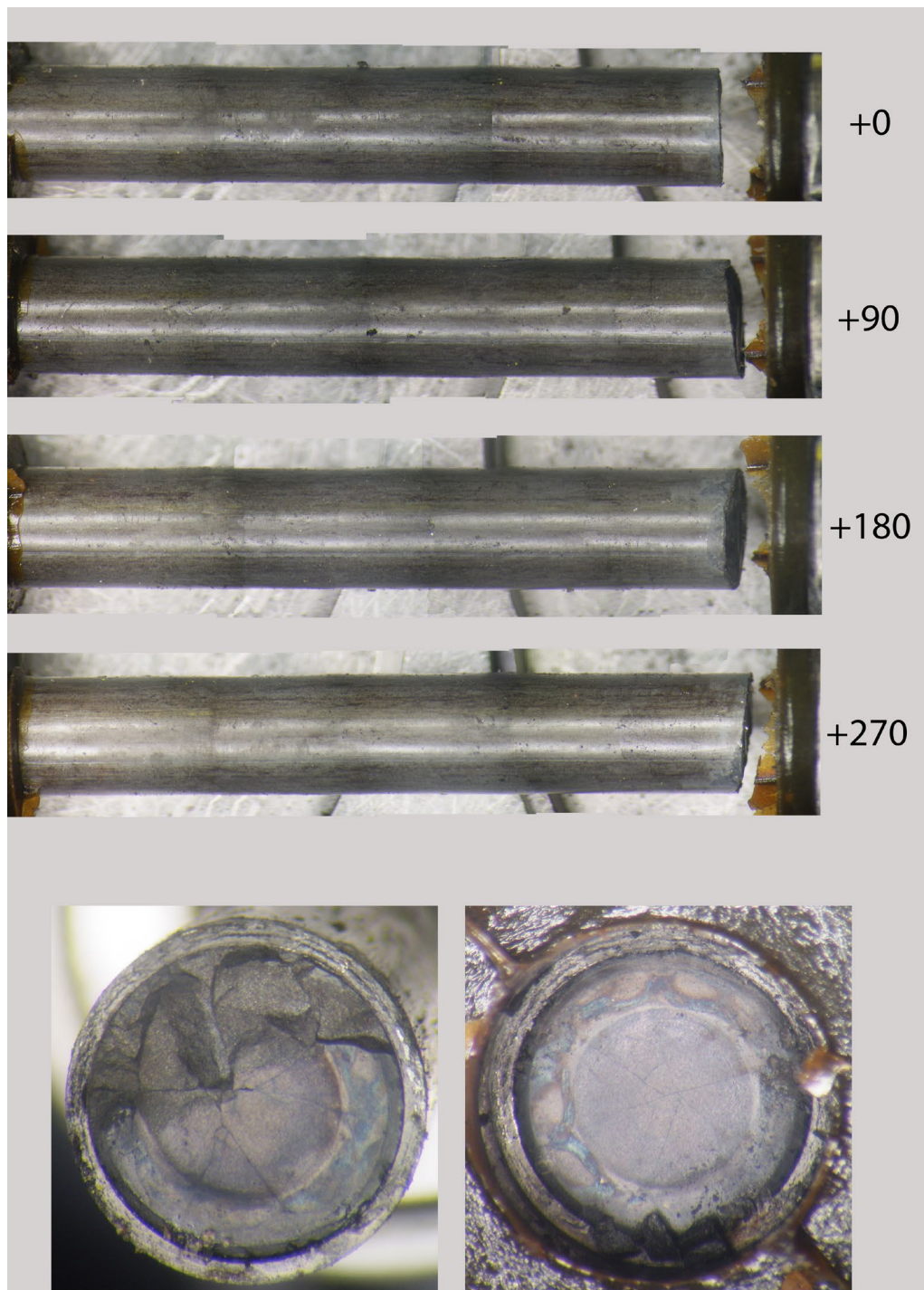


Figure F-21. 6U3K09-2635-2788 post-fatigue test condition.

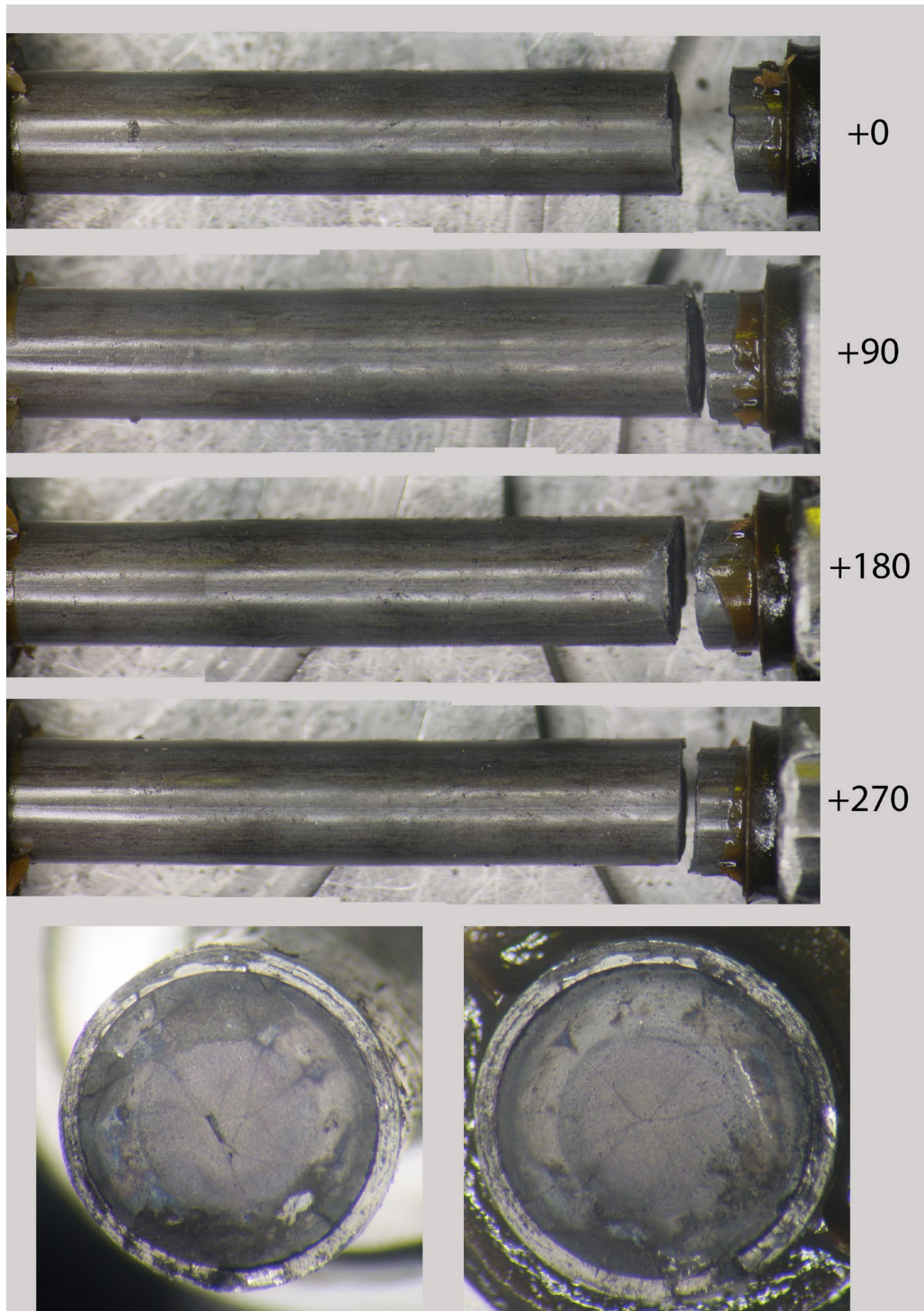


Figure F-22. 6U3K09-2463-2616 post-fatigue test condition.

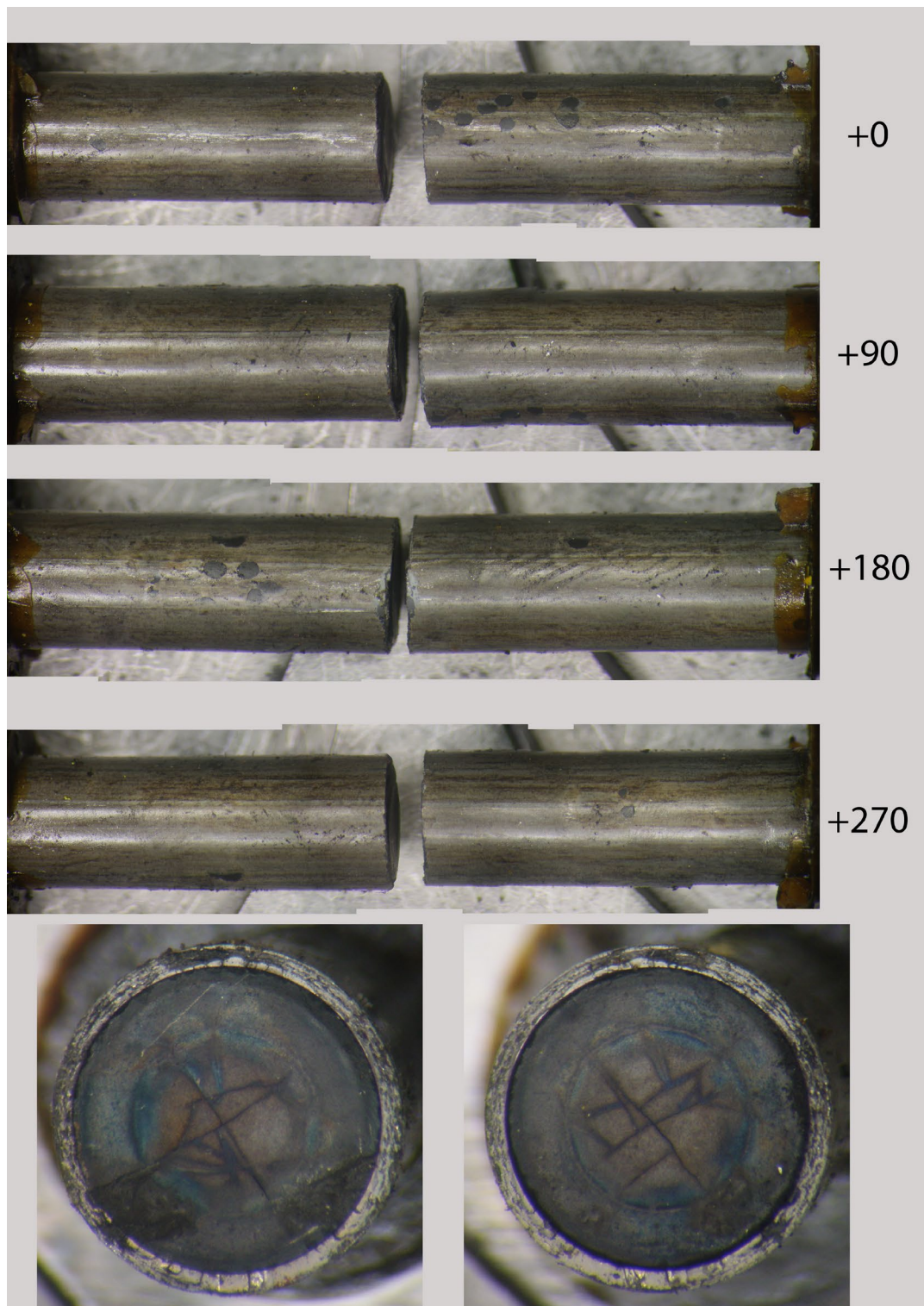


Figure F-23. 3F9N05-2710-2863 post-fatigue test condition.

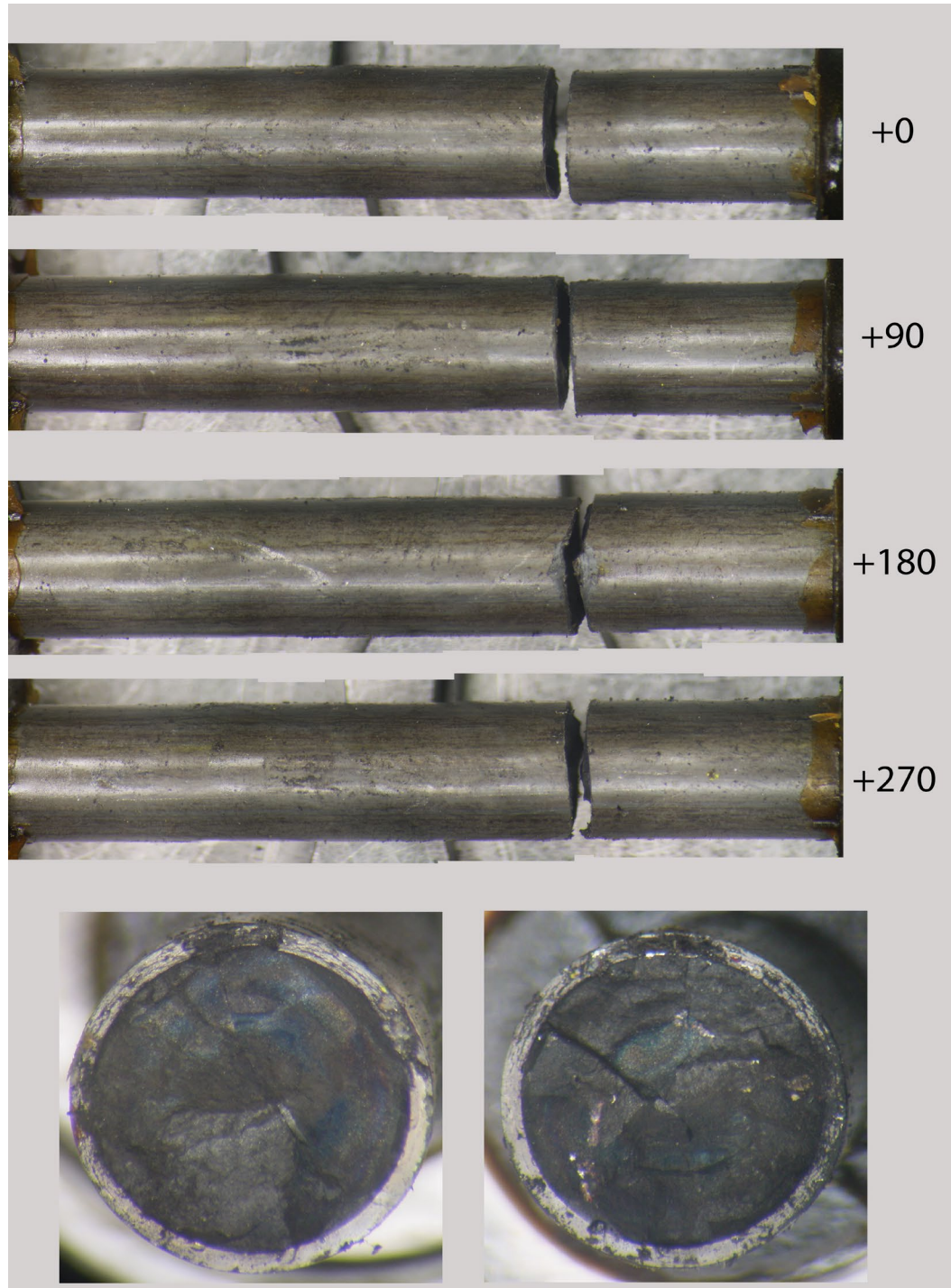


Figure F-24. 3F9N05-2329-2482 post-fatigue test condition.

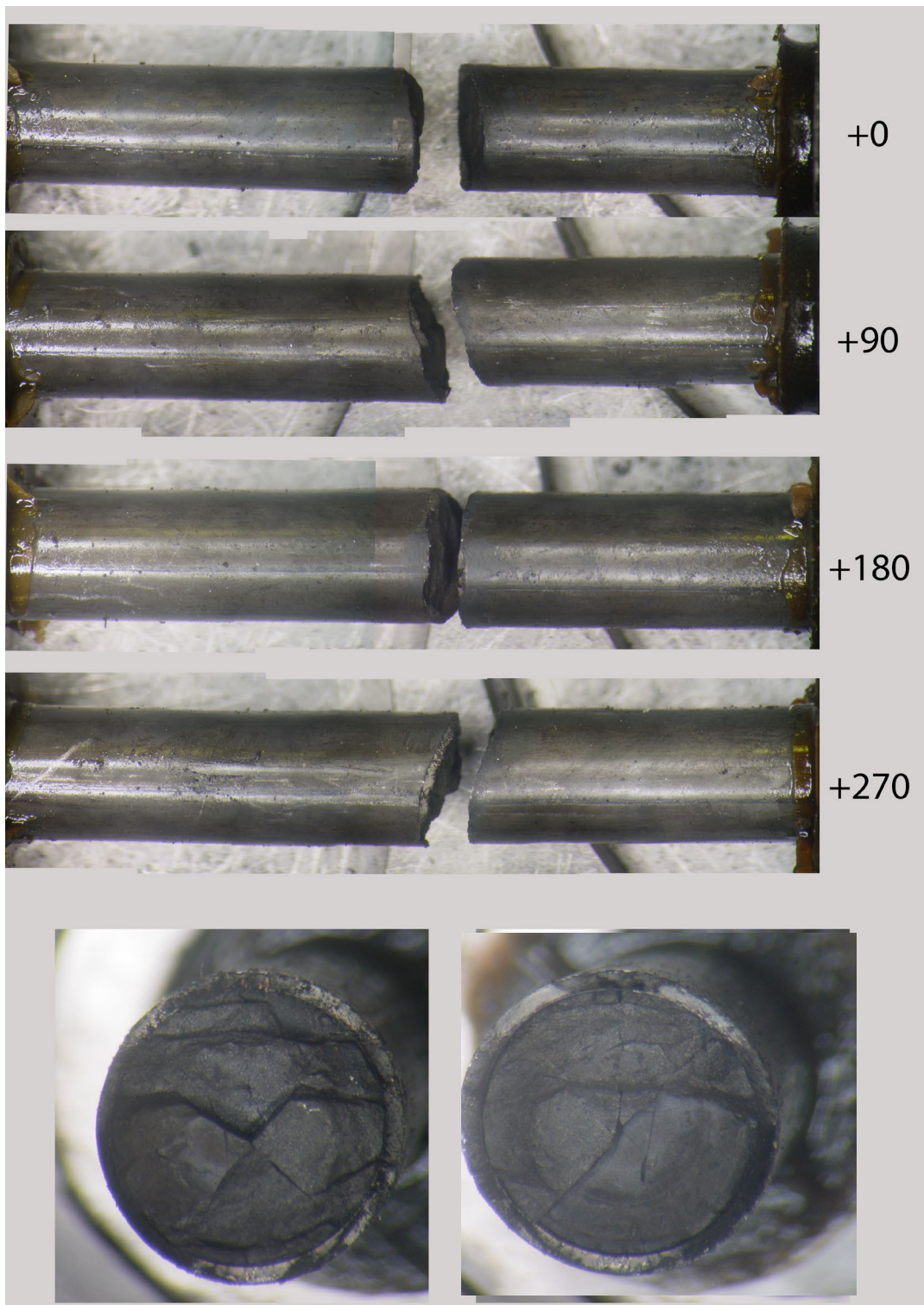


Figure F-25. 3F9N05-0719-0872 post-fatigue test condition.

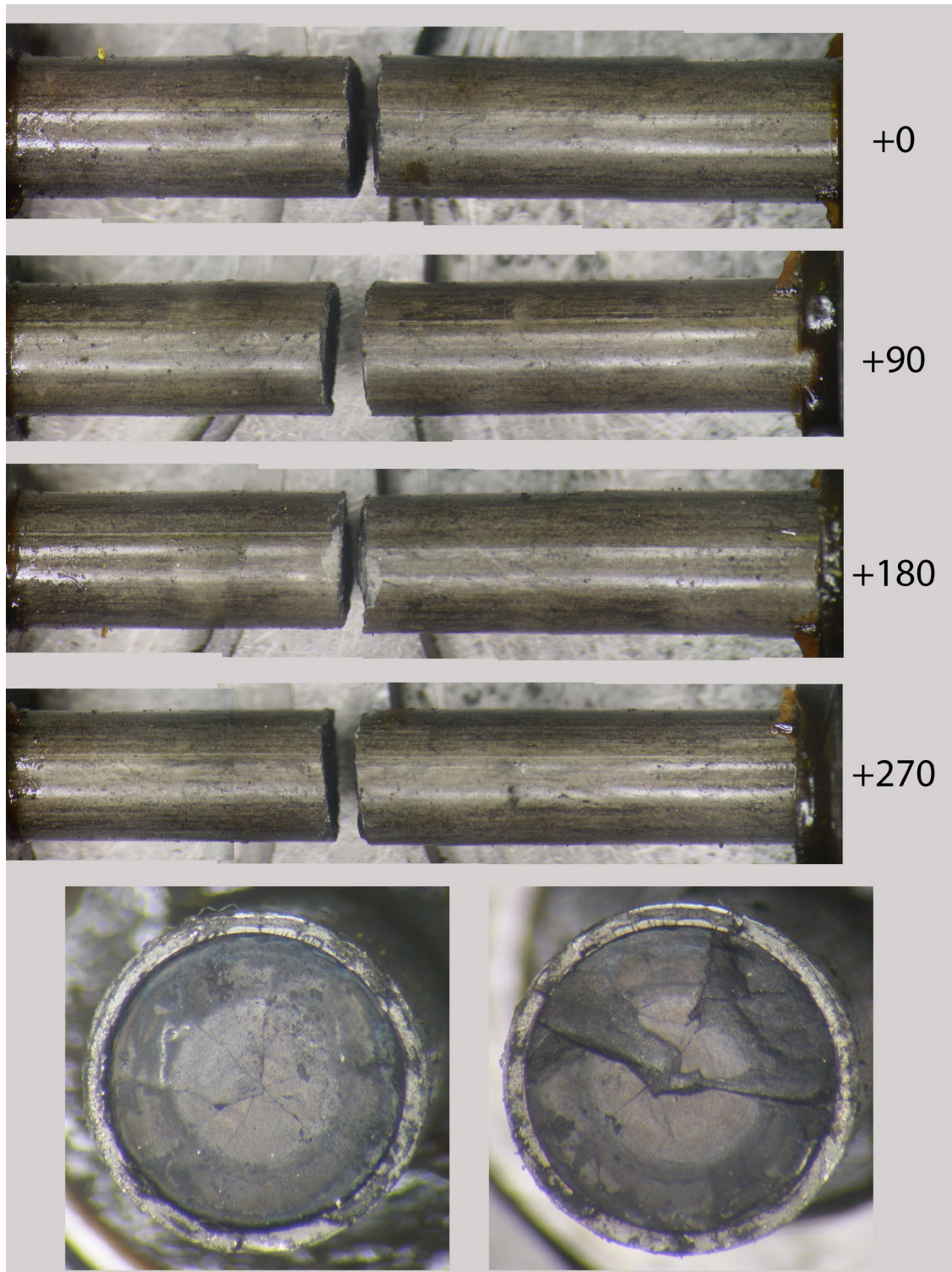


Figure F-26. 3D8E14-2963-3116 post-fatigue test condition.

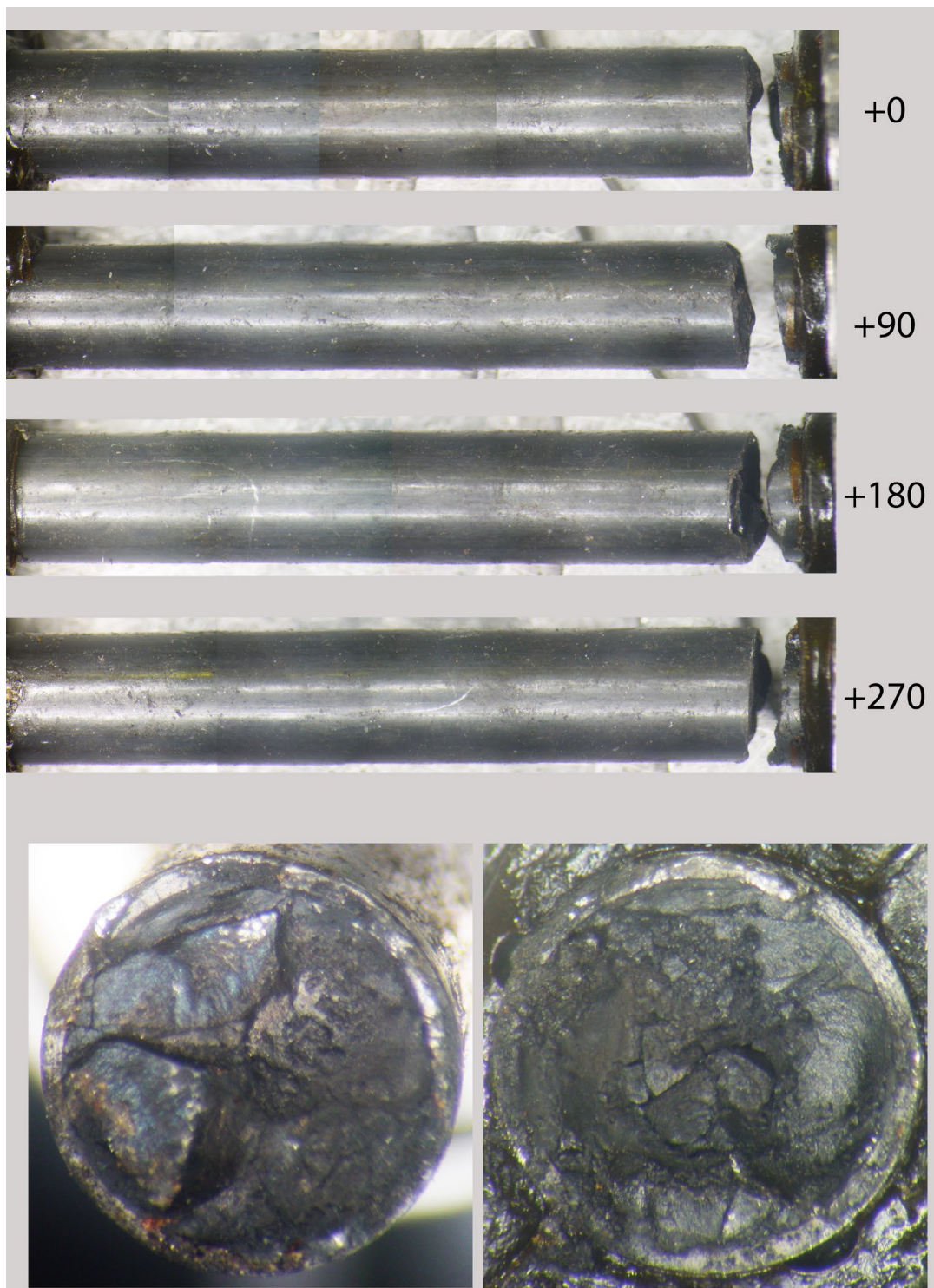


Figure F-27. 30AD05-2630-2783 post-fatigue test condition.

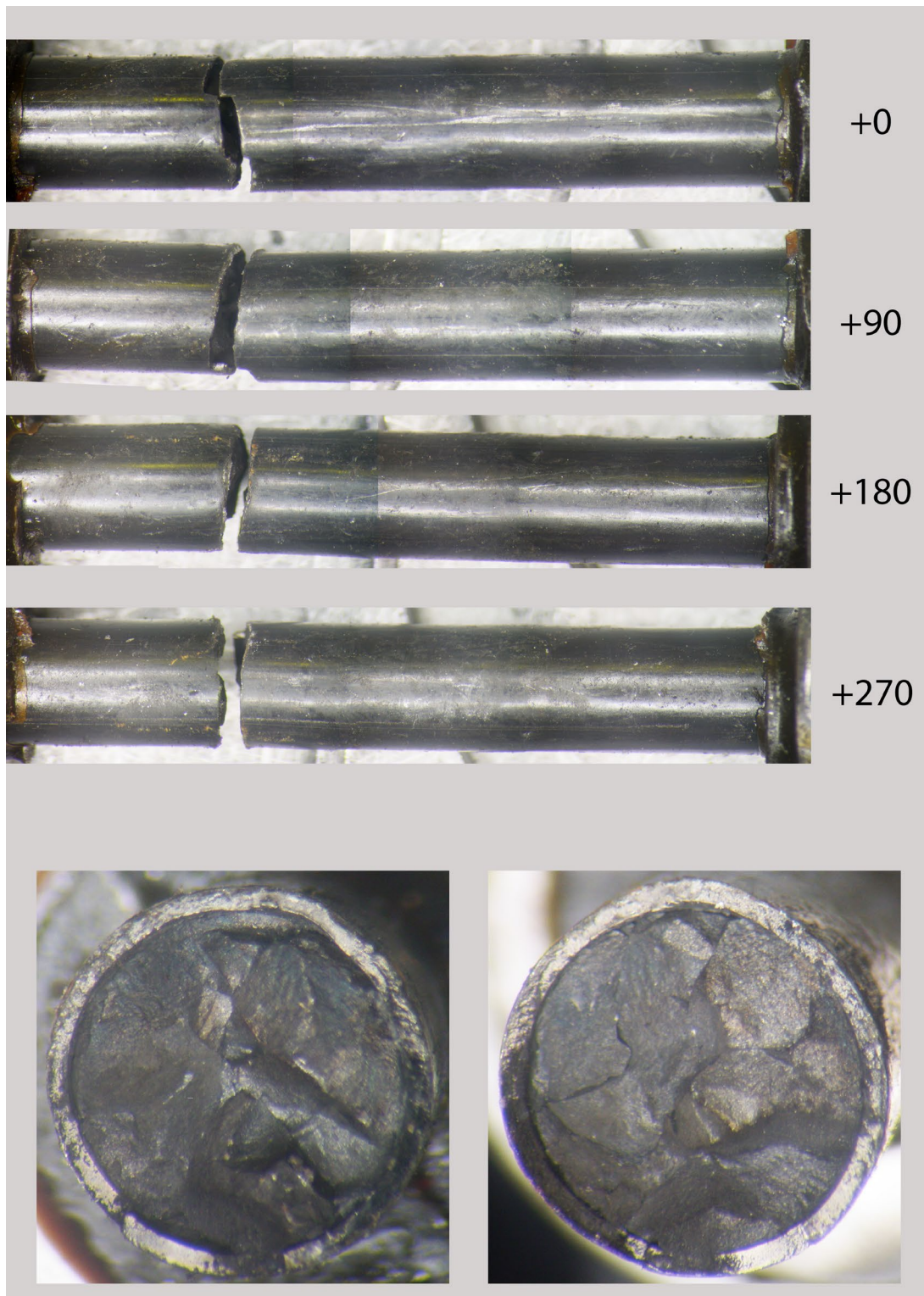


Figure F-28. 30AE14-0672-0825 post-fatigue test condition.

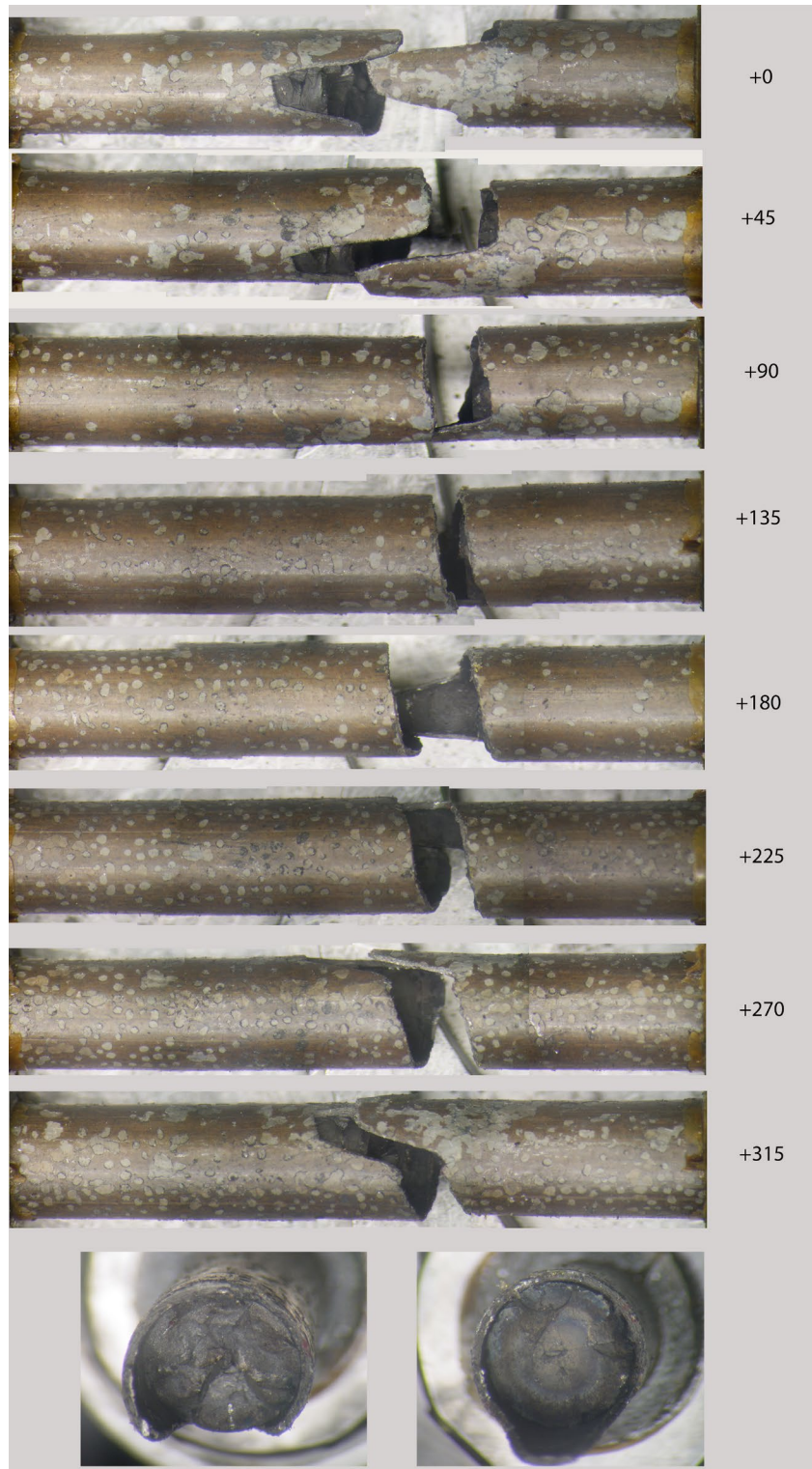


Figure F-29. F35P17-1855-2008 post-fatigue test condition.

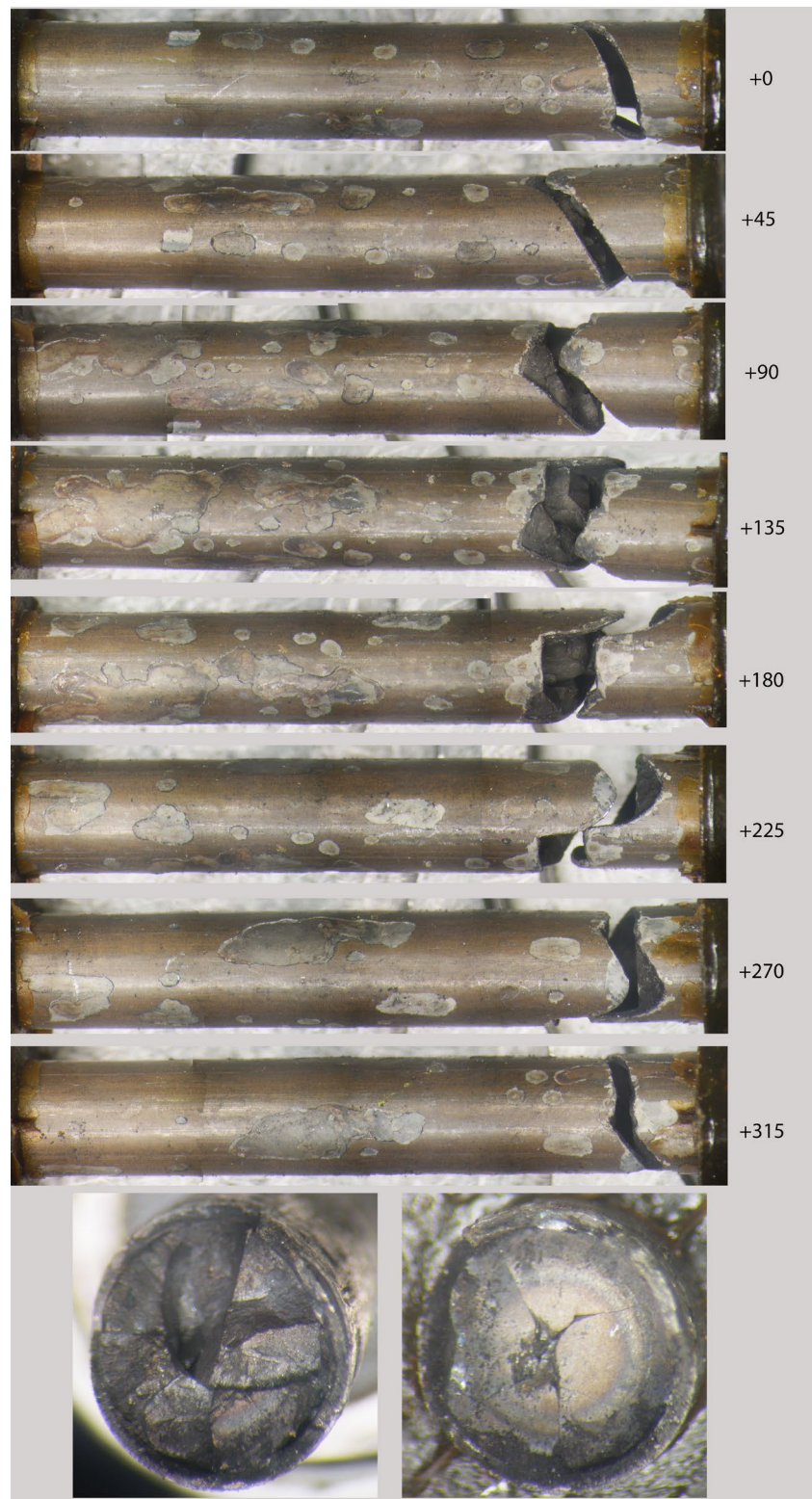


Figure F-30. F35P17-3159-3312 post-fatigue test condition.

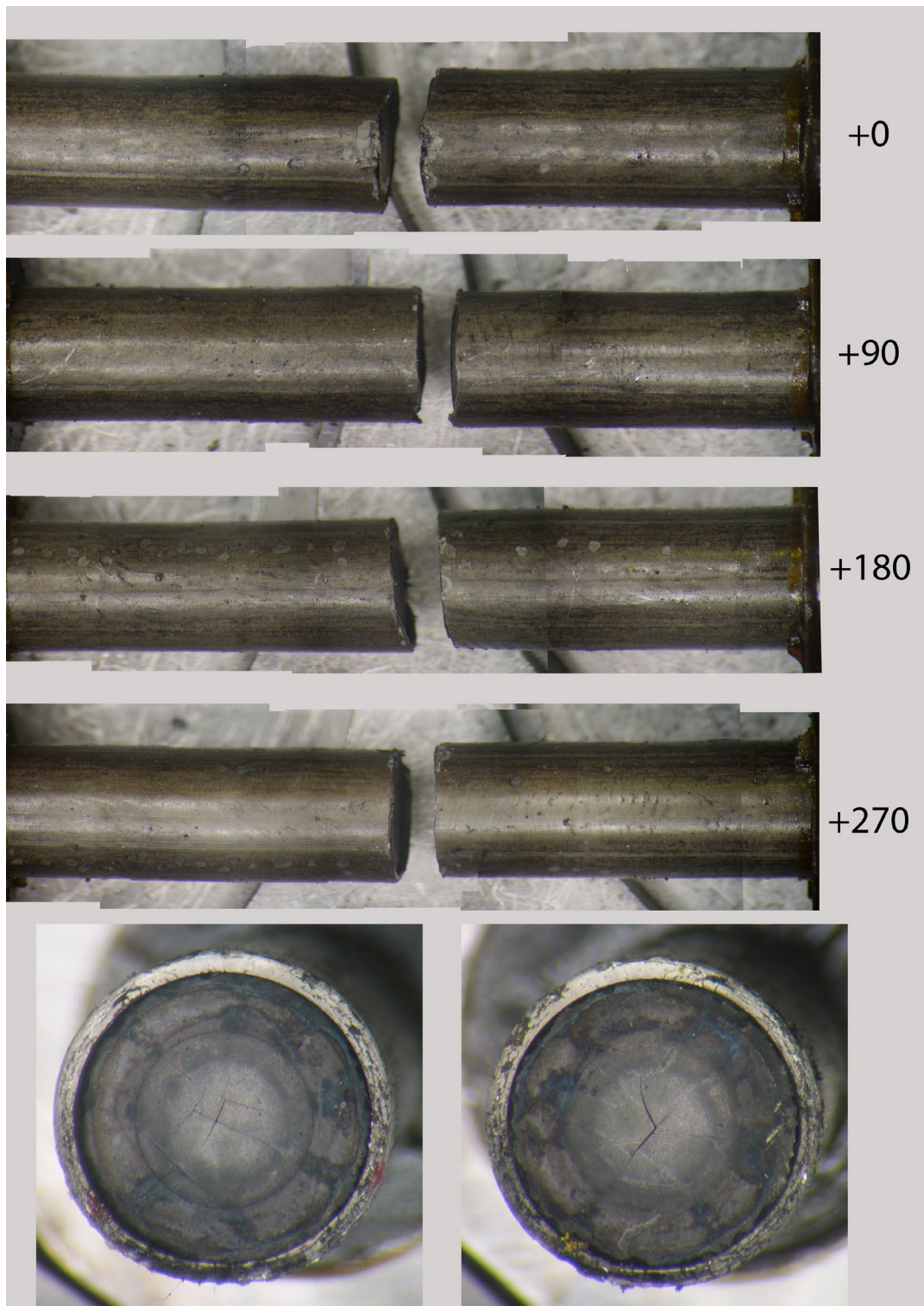


Figure F-31. 3A1F05-2025-2178 post-fatigue test condition.

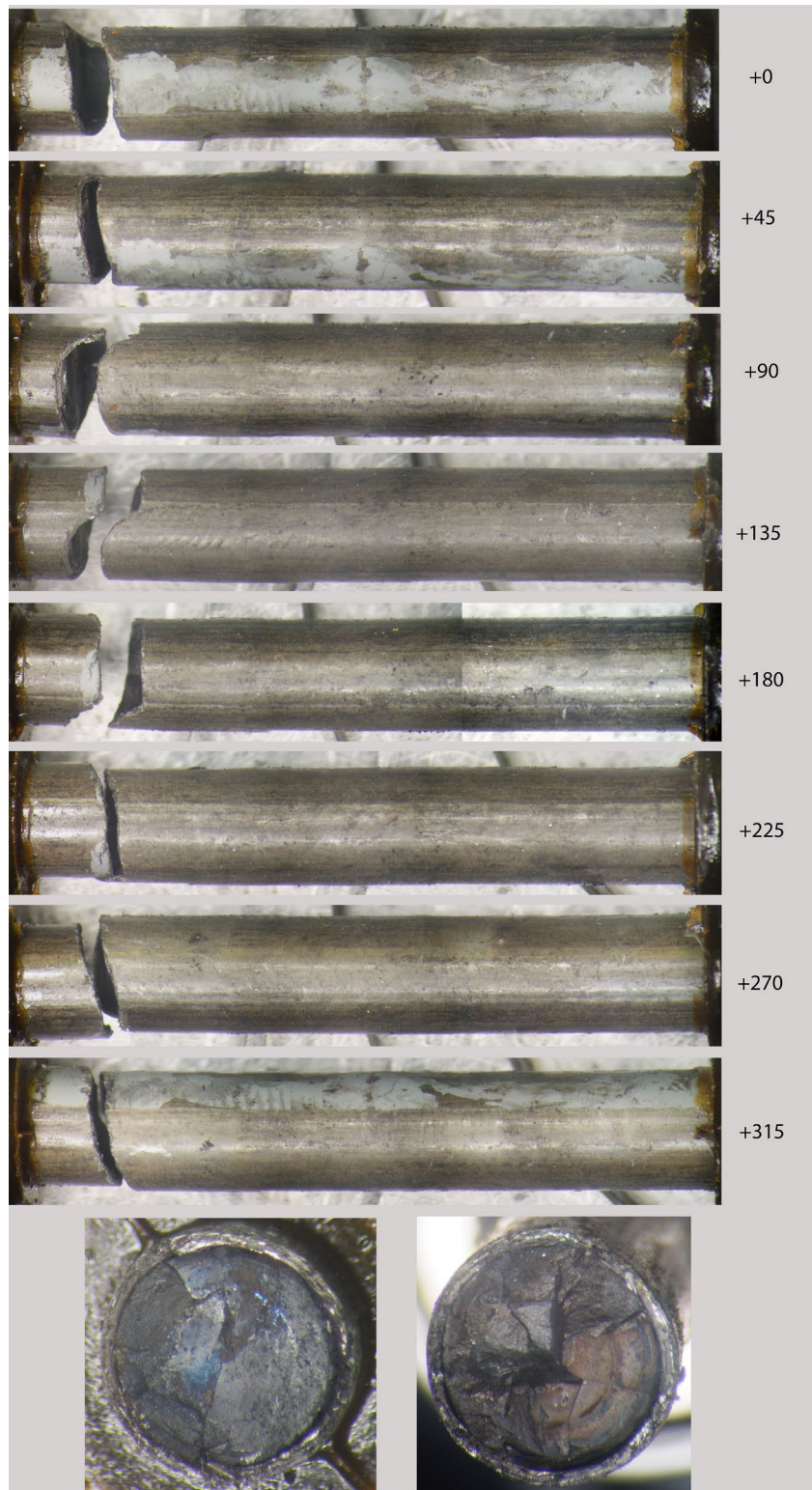


Figure F-32. 3A1F05-1853-2006 post-fatigue test condition.

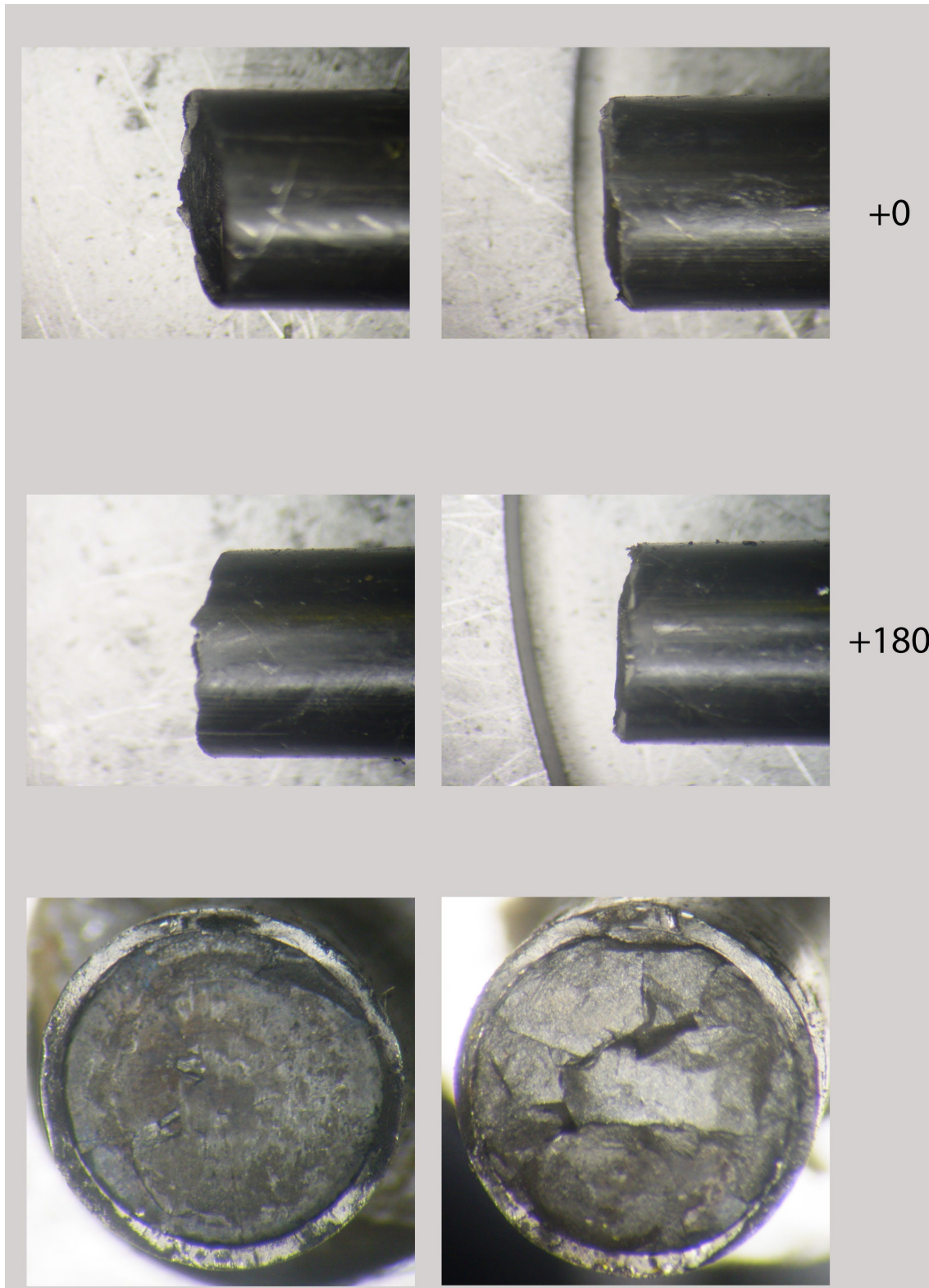


Figure F-33. 30AD05-0697-0850 post-fatigue test condition (broken ends only).

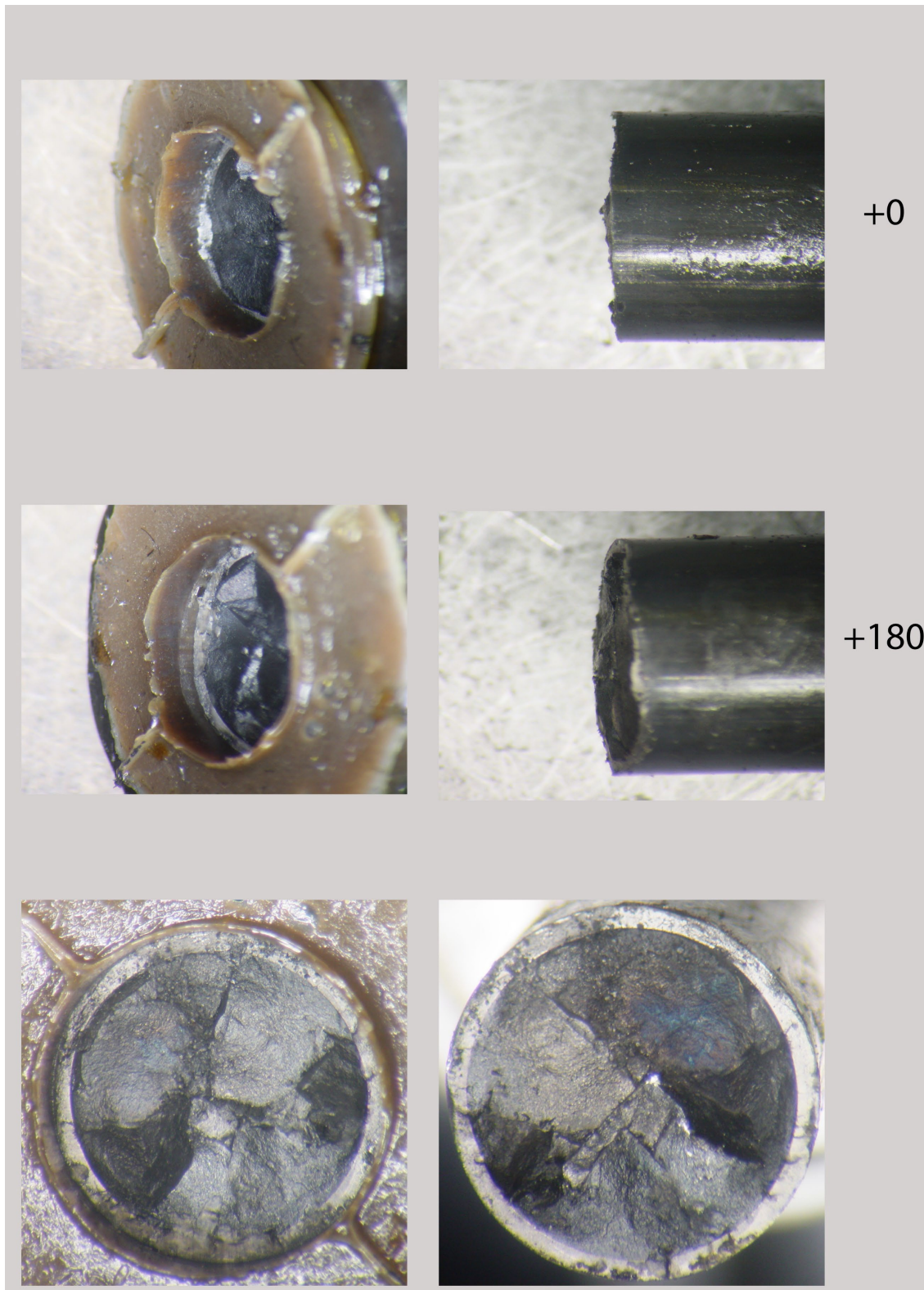


Figure F-34. 30AD05-2050-2203 post-fatigue test condition (broken ends only).

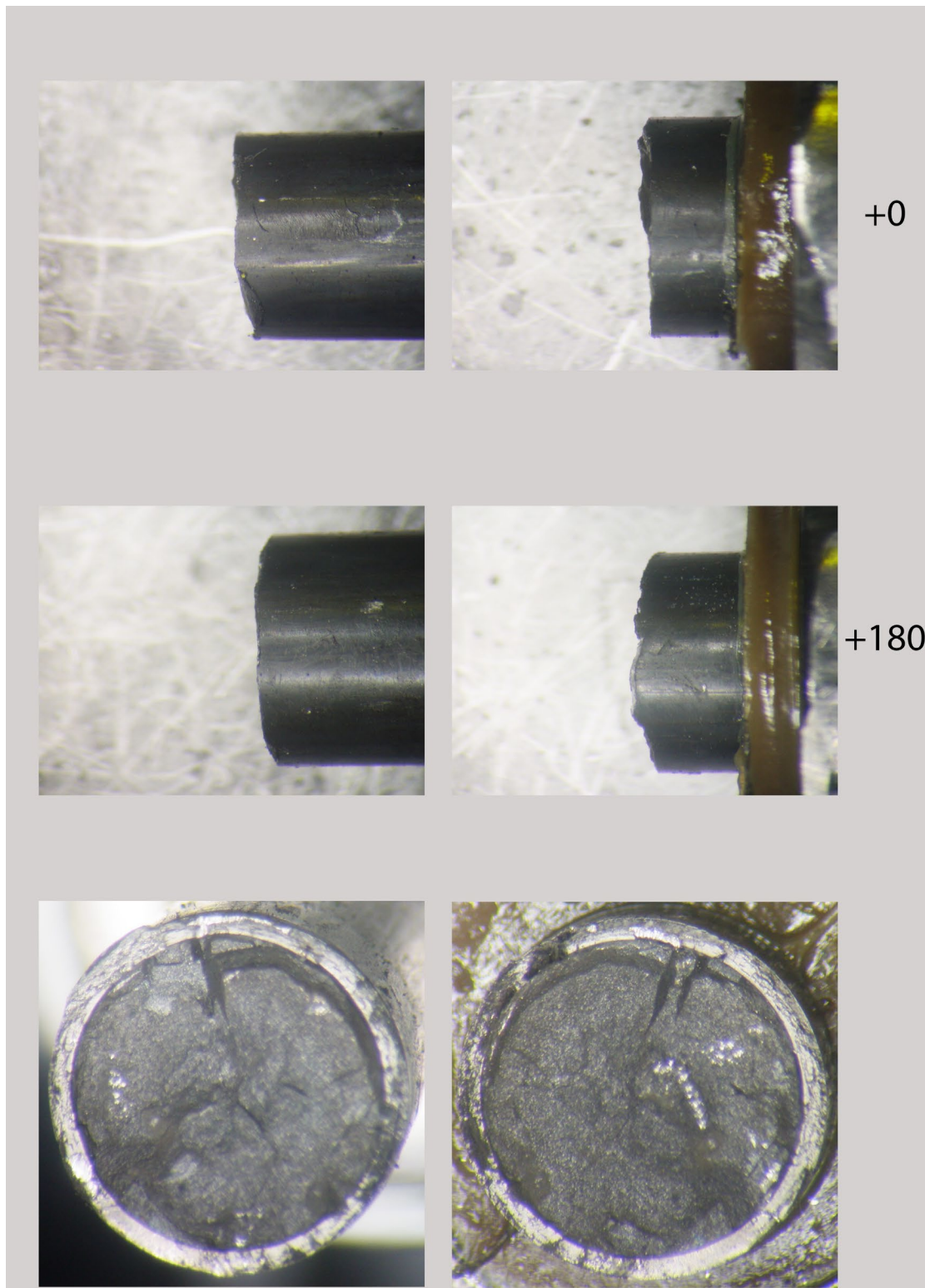


Figure F-35. 30AE14-2850-3003 post-fatigue test condition (broken ends only).

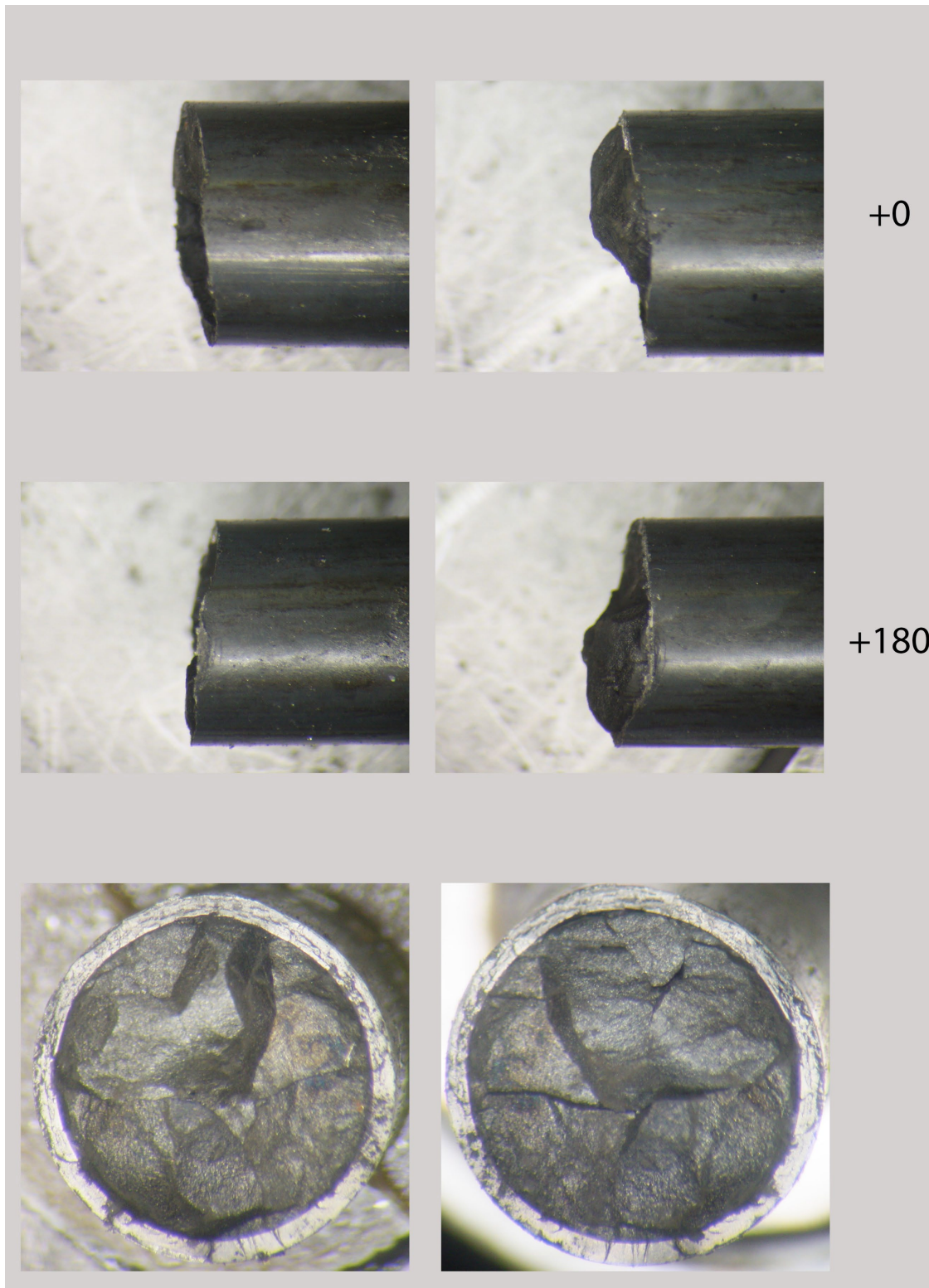


Figure F-36. 30AE14-3156-3309 post-fatigue test condition (broken ends only).

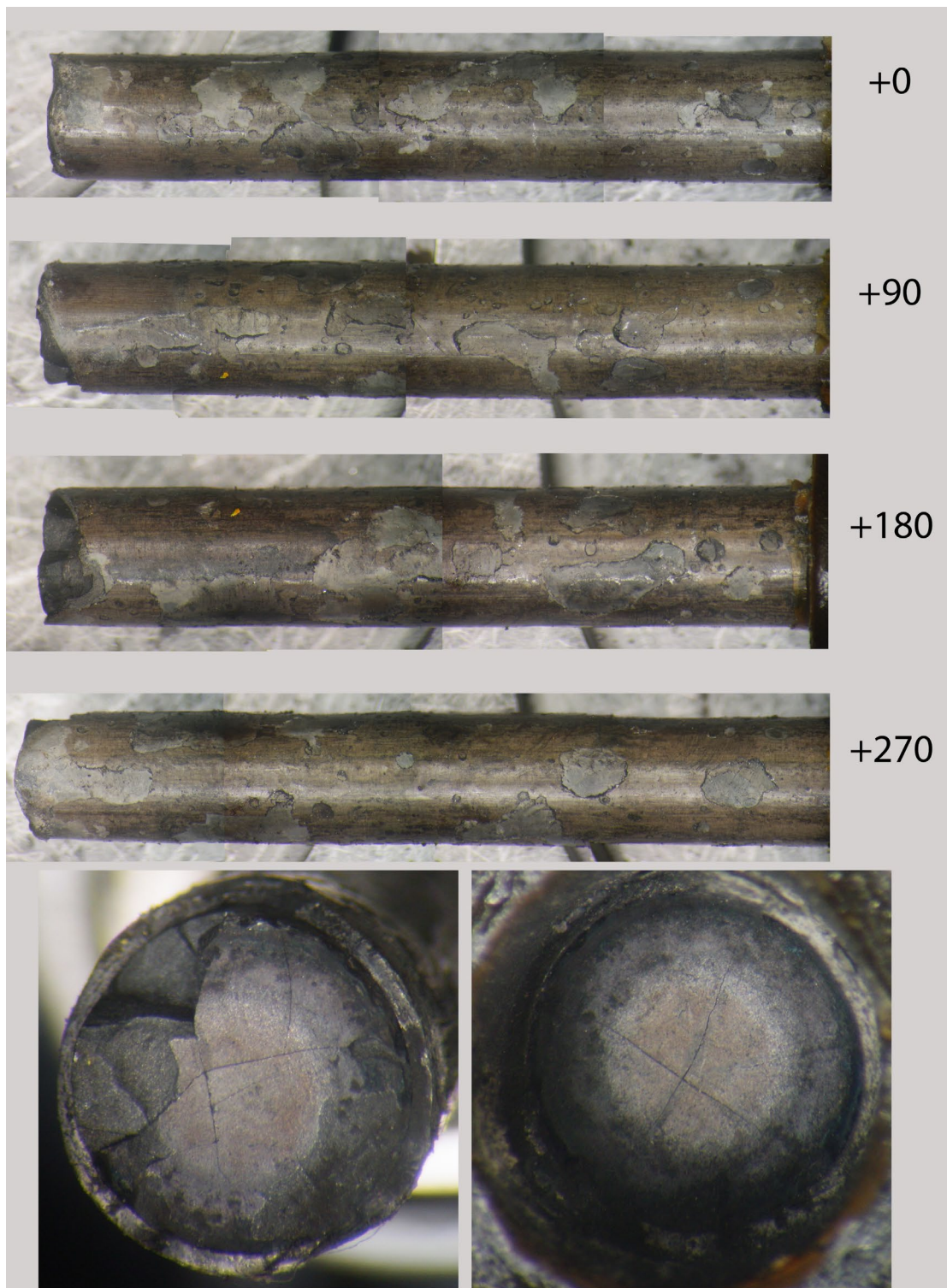


Figure F-37. 3A1F05-3214-3367 post-fatigue test condition.

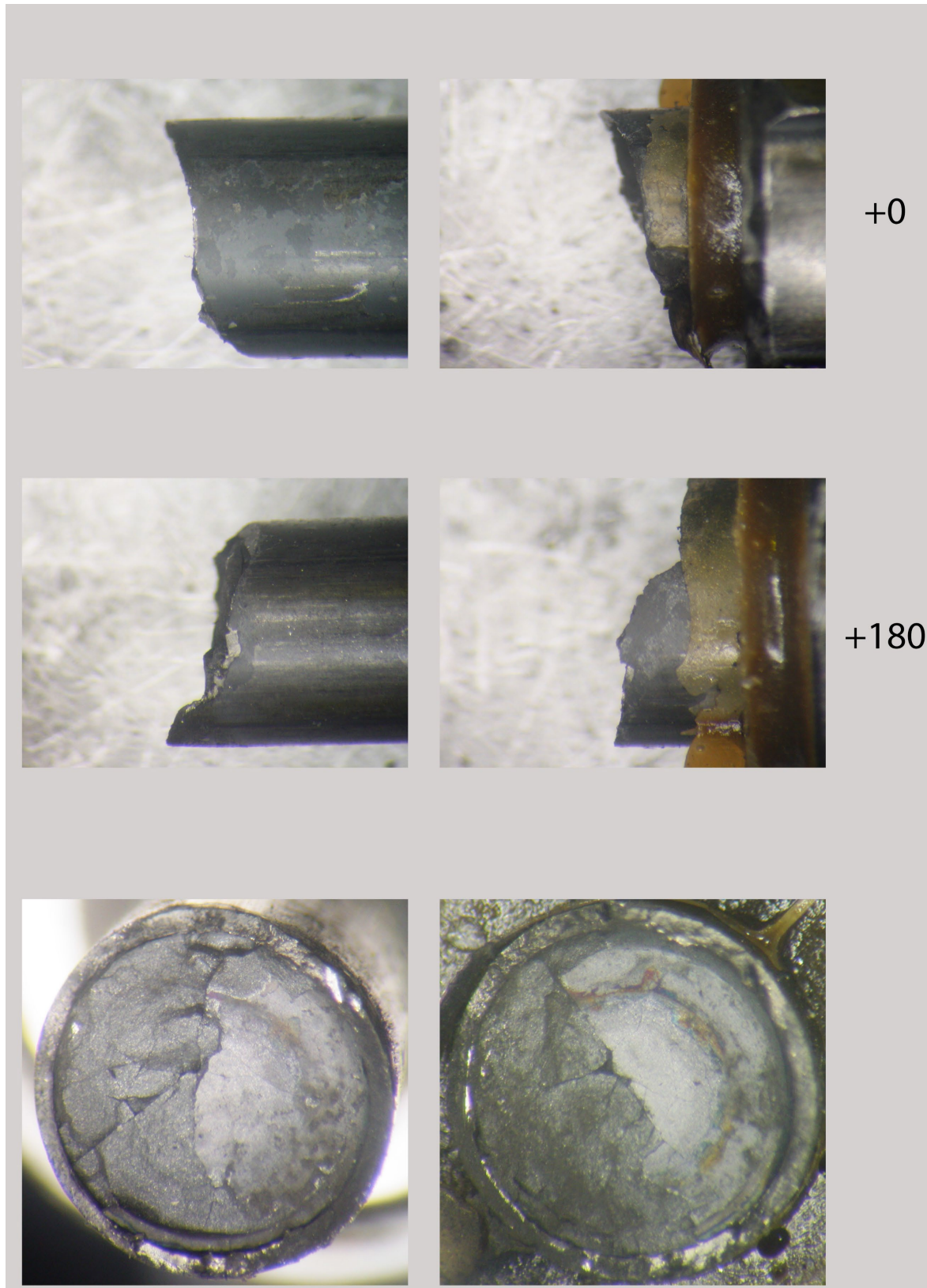


Figure F-38. 3D8E14-719-872 post-fatigue test condition.

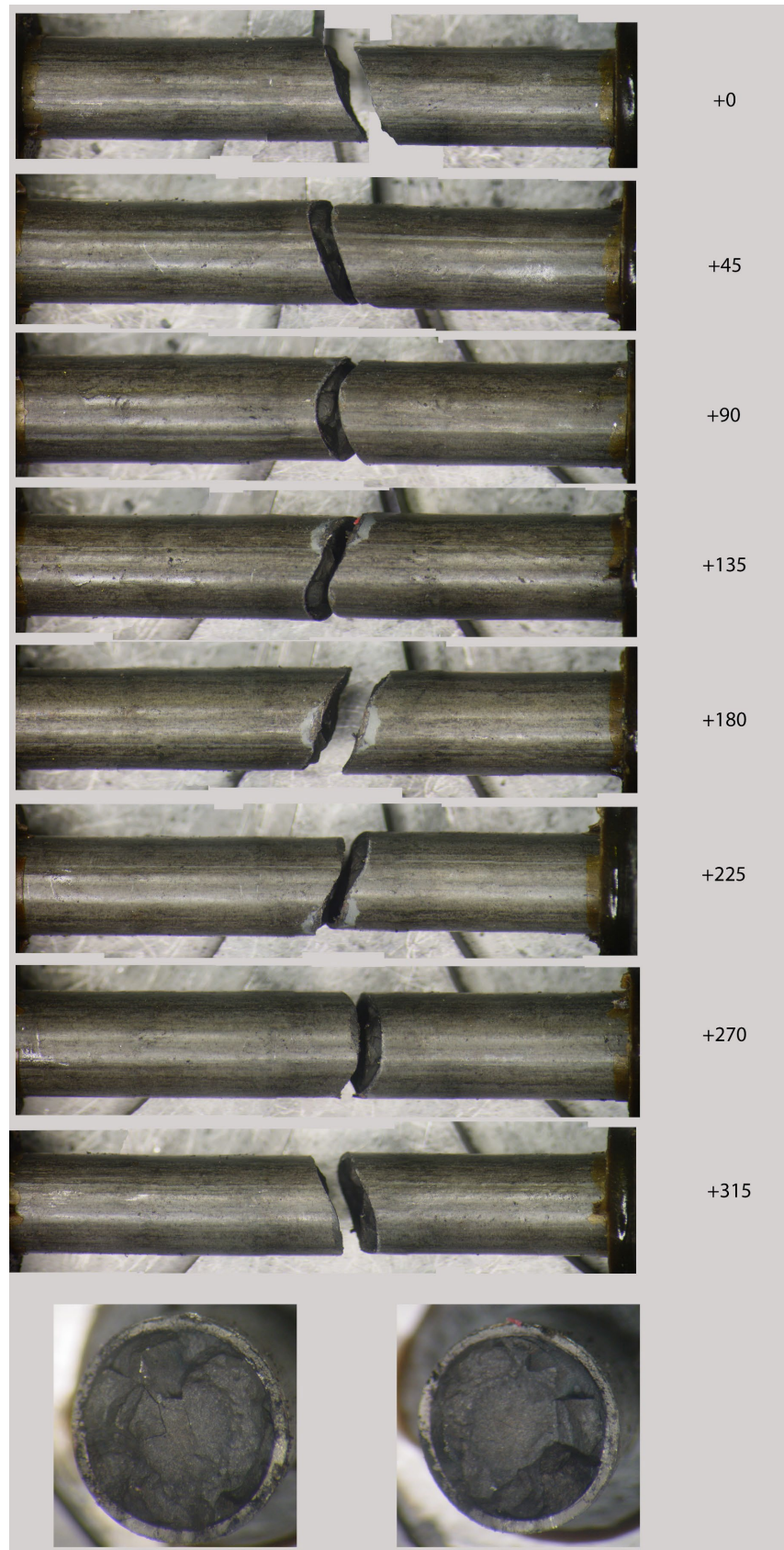


Figure F-39. 3D8E14-2412-2565 post-fatigue test condition.

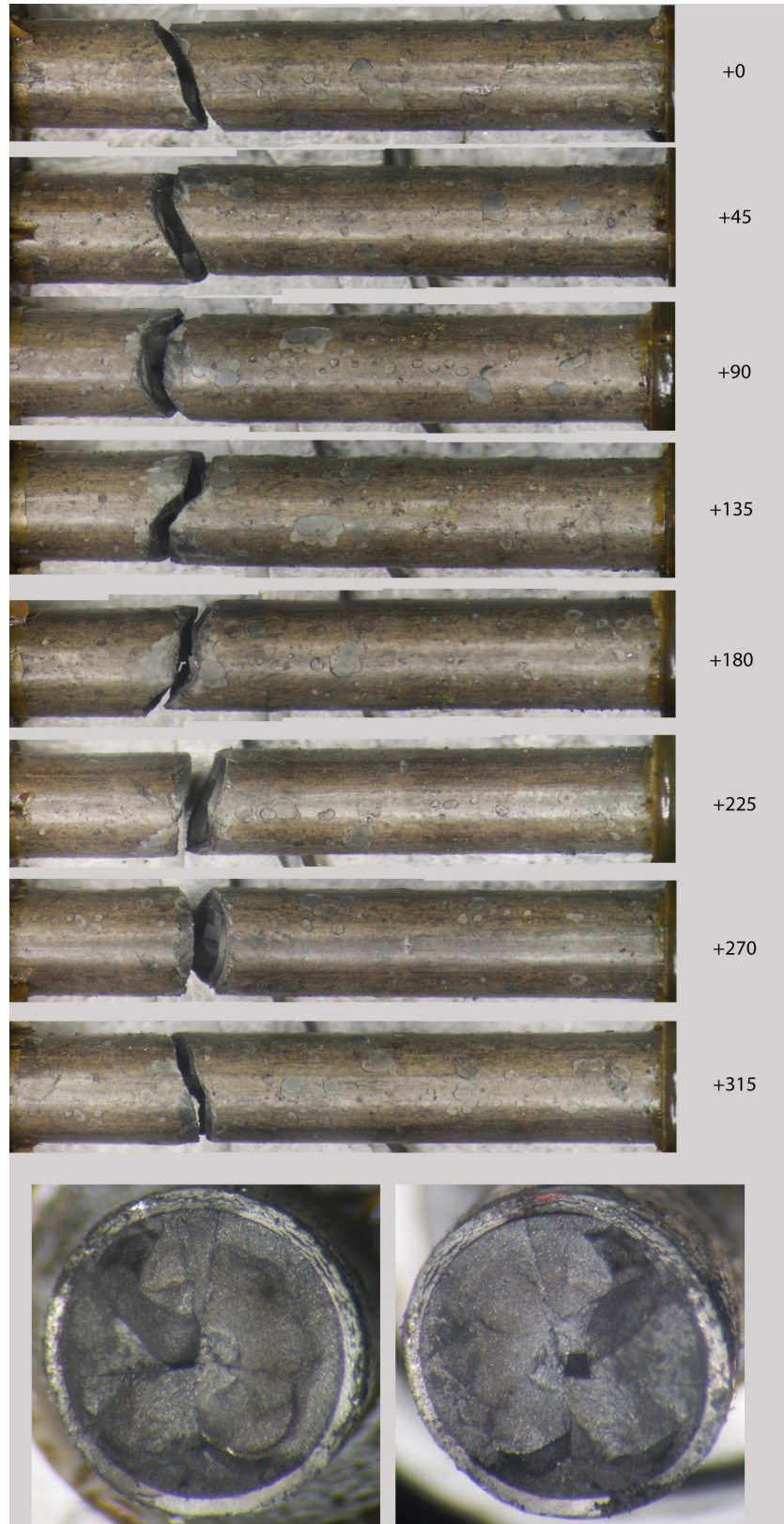


Figure F-40. 3A1F05-3367-3520 post-fatigue test condition.

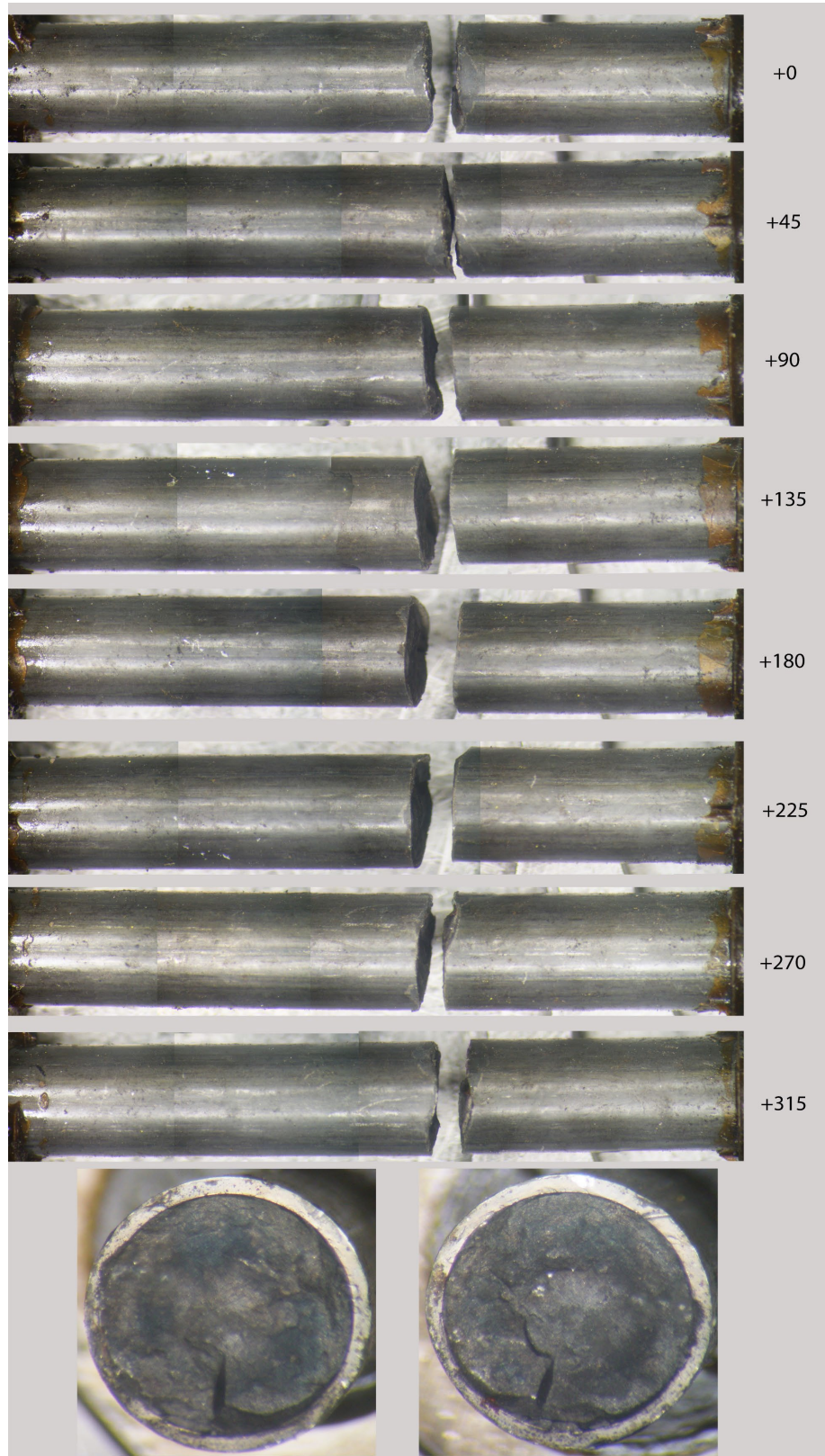


Figure F-41. 3D8E14-1178-1331 post-fatigue test condition.

F-8.5 Scanning Electron Microscope Characterization of Selected CIRFT Fractures

To gain insight into the fatigue failure mechanism, the fracture surfaces of a subset of the samples are being evaluated using SEM. The SEM characterization has six goals: to (1) provide a more thorough investigation of the two specimens that failed at a lower-than-expected-number of cycles, (2) determine whether surface features like oxide spalling are associated with fatigue initiation, (3) further investigate the role of pellet discontinuities causing stress concentration and pellet-clad bonding, (4) determine the direction of fracture (from water side to pellet side, or vice versa), (5) further investigate the role of precipitated hydrides in the fracture, and (6) characterize the mode of fracture (brittle or ductile) and identify accessible materials. A list of potential failed rods for characterization is provided in Table F-16. Fractography of two samples that failed between 40,000 and 50,000 cycles (applied strain amplitudes were 0.15% and 0.18%) is reported herein and is highlighted in Table F-16.

In addition, fractography of two unirradiated cladding-only CIRFT specimens is documented herein to better understand how failure occurs without the presence of the pellet, which will provide a reference for the fractography on the failed fuel rods. The two samples reported herein failed between 30,000 and 100,000, which is comparable with the fuel rods characterized, although the applied strain amplitudes were larger (0.40% and 0.46%).

Finally, future work for next year is described that will investigate the role of precipitated hydrides in the fracture.

Table F-16. CIRFT Specimens Identified for Potential SEM Characterization.

Samples highlighted with shading have been started, and those in **bold** have been completed.

Cladding material	CIRFT Specimen ID	Estimated specimen-average burnup (GWd/MTU)	Cycles to failure	Strain amplitude (%)	Status
M5	30AD05-0697-0850	58	3,368	0.47	Not started
M5	30AD05-2050-2203	59	133,000	0.08	Not started
M5	30AD05-2630-2783	59	22,300	0.18	Started
M5	30AE14-0672-0825	56	1,630	0.36	Not started
Zirc-4	F35P17-2027-2180	66	1,340,000	0.07	Not started
Zirc-4	F35P17-3159-3312	62	773	0.15	Not started
LT Zirc-4	3A1F05-3214-3367	48	3,450	0.19	Not started
LT Zirc-4	3A1F05-1853-2006	56	1,300	0.39	Not started
LT Zirc-4	3A1F05-2025-2178	56	48,200	0.18	Complete
ZIRLO	3D8E14-2412-2565	64	191,000	0.08	Started
ZIRLO	3D8E14-2963-3116	62	39,700	0.15	Complete
ZIRLO	3F9N05-2329-2482	59	189,000	0.10	Not started
ZIRLO	6U3K09-2310-2463	59	1.75E+04	0.20	Started
ZIRLO	6U3K09-3200-3353	50	3.49E+04	0.15	Not started

F-8.5.1 Sample preparation

A CIRFT-fueled specimen is prepared in the hot cell for SEM characterization by cutting off the tip of one side of the fractured specimen. The cut is made a few millimeters from the fractured end, and the sample is then defueled. The sample is then attached to a metallic mount using conductive adhesive, avoiding the fracture surfaces. After curing, the sample is transferred out of the hot cell to the SEM enclosure. Once in

the SEM, a montage of the entire circumference is created at a relatively low magnification ($\sim 25\times$). The circumference is divided into four quadrants to allow for imaging and identifying regions of interest.

The CIRFT unirradiated cladding specimens were similarly prepared out of cell but were inserted directly in a mounting fixture rather than being attached to a metallic mount with conductive adhesive.

F-8.5.2 Characterization of Fracture in ZIRLO- 17 × 17

To provide a baseline characterization, a ZIRLO-clad sister rod that fractured as expected and with a fatigue lifetime consistent with other data (3D8E14-2963-3116) was sectioned, SEM-imaged, and characterized. Optical images of this sample are provided in Figure F-26 and Figure F-42. This sample failed near the center of the CIRFT test gauge section, and its fatigue life (39,700 cycles) was consistent with previous test data.

The most distinct feature of 3D8E14-2963-3116's fracture surface is in the upper part of quadrant 1 near the boundary with quadrant 4. At the end of each CIRFT test, the specimen must be removed from the CIRFT machine. Often, the specimen has not fractured completely, and the fracture must be manually completed to remove it from the CIRFT machine. A fracture area in quadrant 1 was likely created after the fatigue test was stopped, during removal of the dogbone specimen from the test equipment. At higher magnification (Figure F-43), the features near the center of the cladding wall have a classic ductile dimple appearance, further suggesting that the fracture surface was created as the specimen was removed from the equipment rather than during the fatigue test. In contrast, the features in quadrant 1 near the cladding ID appear to be more brittle, with ratchet lines typical of fatigue, thus indicating that these features were created during the fatigue test.

In quadrant 3, shown in Figure F-44 ($\sim 180^\circ$ from the quadrant 1 region), the features are flat compared with those in quadrant 1. This is likely the quadrant where the fatigue crack first initiated, and then wear of the surfaces progressed as the test continued. High magnification of one area in quadrant 3 shows ratchet lines emanating from the cladding ID surface, suggesting that the fatigue crack initiated on the ID in this region.

The high magnification images from quadrants 2 and 4 both show remnants of fatigue crack propagation in the form of fatigue striations (see Figure F-45 and Figure F-46). These images also show indications of circumferential cracks in both quadrants, which might be associated with propagation of the crack along precipitated hydrides. The flat area on the cladding ID in quadrant 4 might be a fatigue crack initiation site.

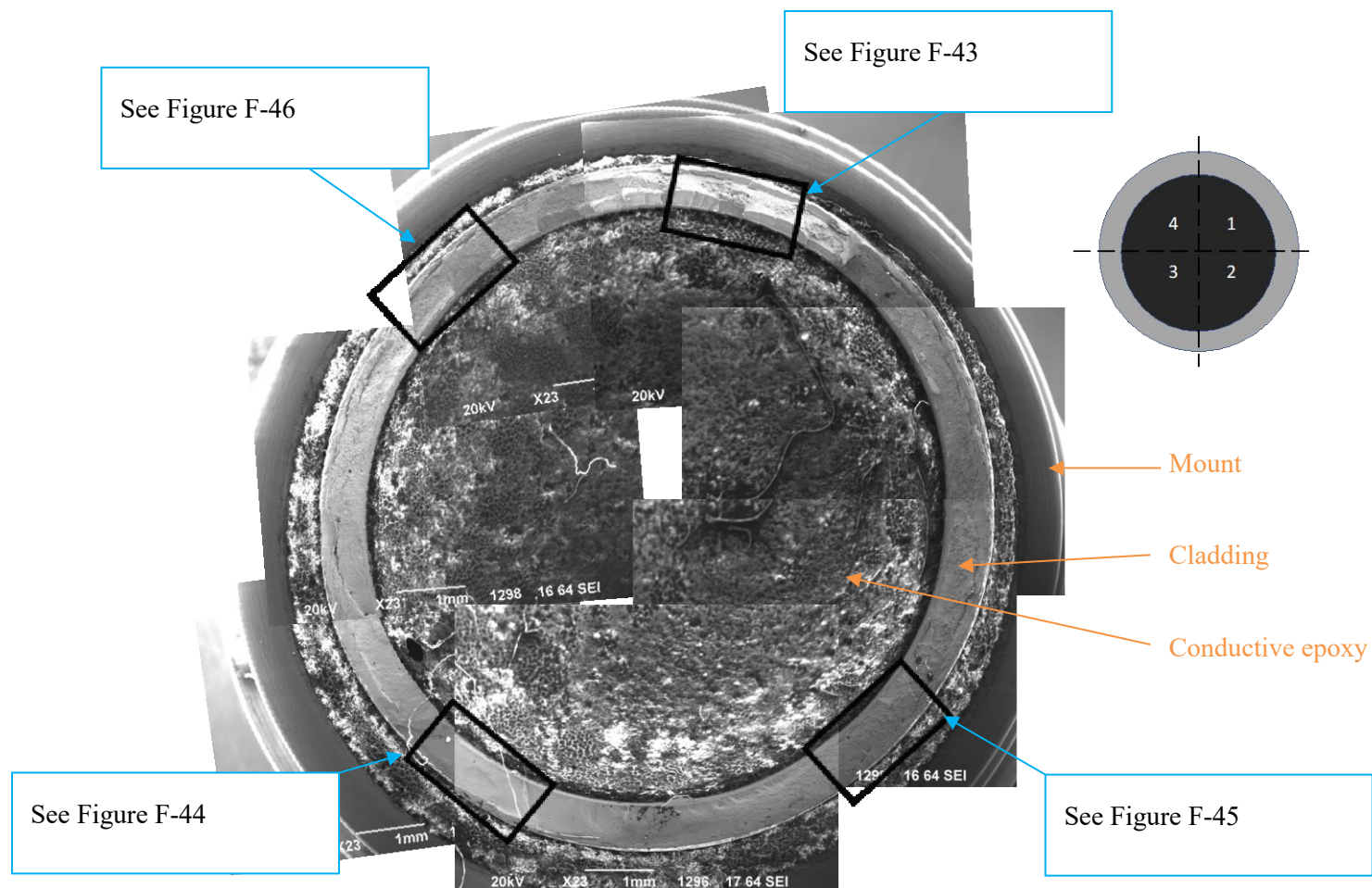


Figure F-42. Montage (23×) of the surface of the fatigue failure in sample 3D8E14-2963-3116. The areas identified in the various quadrants were investigated at higher magnification (see Figures F-42 to F-45).

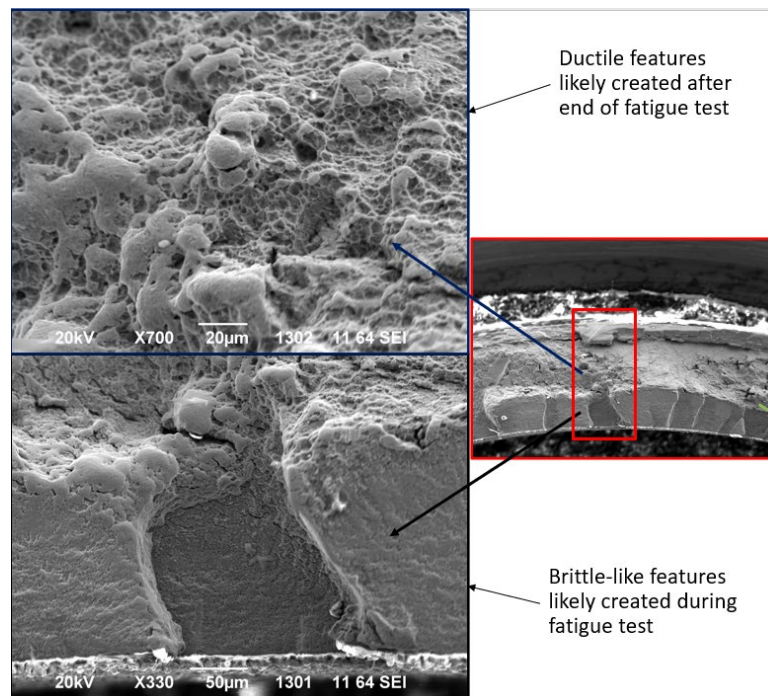


Figure F-43. Images at 330× and 1,000× of quadrant 1 in sample 3D8E14-2963-3116.

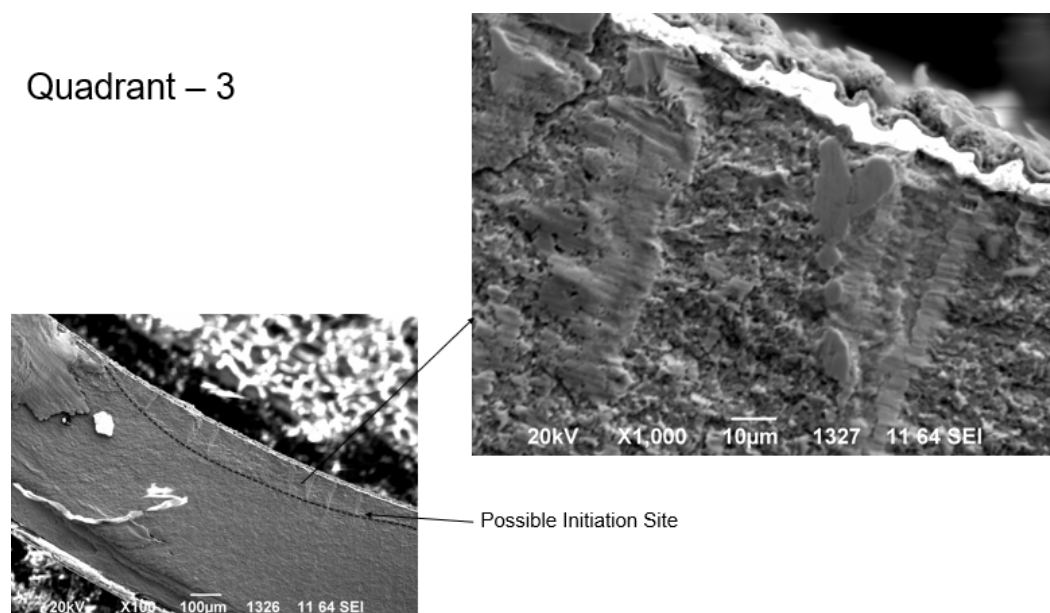


Figure F-44. Images at 100× and 1,000× of quadrant 3 in sample 3D8E14-2963-3116, ~180° from region in quadrant 1 that is suspected to have failed after fatigue test ended.

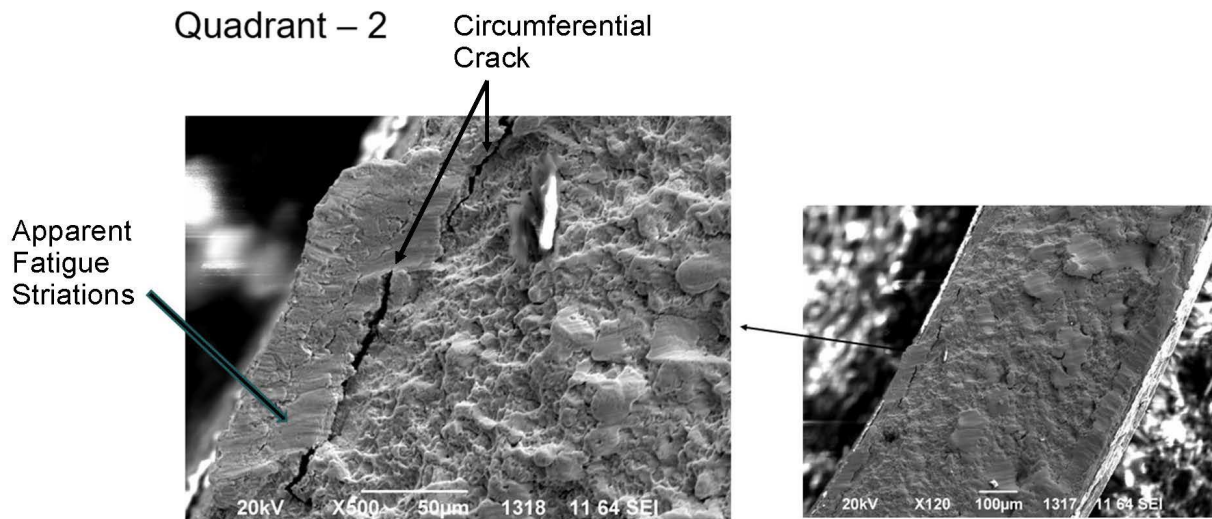


Figure F-45. Images at 120× and 500× of quadrant 2 in sample 3D8E14-2963-3116, showing signs of fatigue striations typical of fatigue crack propagation, indicating propagation in the circumferential direction.

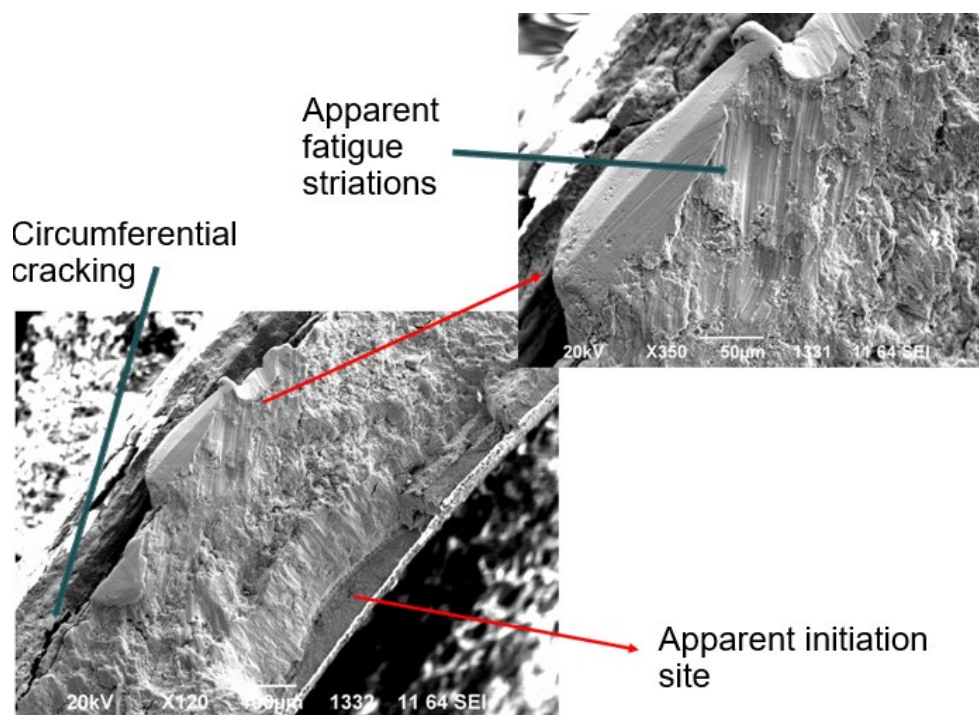


Figure F-46. Images at 120× and 350× of quadrant 4 in sample 3D8E14-2963-3116 showing signs of fatigue striations typical of fatigue crack propagation. The flatness of the feature on the cladding ID might be associated with fatigue initiation. Circumferential cracks near the cladding OD might also be associated with hydrides.

F-8.5.3 Characterization of Fracture in LT Zirc-4 Fuel Rods

Figure F-31 and Figure F-47 provide the optical images of sample 3A1F05-2025-2178 (DE50017) after failure. Figure F-47 is a montage of the failed surfaces of 3A1F05-2025-2178 taken at 100× magnification around the fracture surface. Various regions of interest were identified from the montage for further imaging at higher magnification. This sample failed under medium load at a pellet-pellet interface, near the center of the CIRFT test gauge section, and its fatigue life (48,200) was consistent with previous test data. The fatigue initiation appears very close to fatigue failure, as can be observed from the moment vs. curvature data.

The montage is divided into four quadrants (Q1, Q2, Q3, and Q4). From a simple observation in the montage, Q2 appears relatively flat and has no visible circumferential cracks, which are most often seen because of precipitated hydrides. Q4, like Q2, has flat brittle or cleavage-like areas that appear to be crack initiation sites on the ID; these are similar to those seen in sample 3D8E14-2963-3116, as reported in the last FY.

Figure F-48 and Figure F-49 show two different regions in Q1. Whereas Q1 has areas of ductile fractures and circumferential cracks, there are cleavage-like regions approaching Q2 that are indicative of brittle behavior. The features continue in Q2, as shown in Figure F-50, where many of these crack initiation features (termed “beach marks”), including cleavage-like regions adjacent to fatigue striations, can be observed. No ductile fracture regions were observed in Q2. Figure F-50 also shows a different type of flat feature but with long running striations that do not quite match the fatigue striations seen elsewhere. This flat feature is thought to be formed by wear because the fractured rod continues a few cycles during and after propagation.

Figure F-51 shows the ductile fracture regions in Q3, along with long-running circumferential cracks that were prominent between small brittle regions and beach marks that are similar to the features seen in Q1 (Figure F-48).

Figure F-52 shows the flat brittle or cleavage-like regions seen in Q4. The flat regions look similar to the brittle fracture regions seen in Q2 that are associated with fatigue failure. Note that the brittle regions, where the fatigue failure likely initiated, can be seen on the fuel side of the sample. This points towards stress concentrations that were acting on this side of the cladding because of the fuel pellet. Thus, it can be stated that the pellet does play a role in the fatigue process and acts as a source for the initiation.

Although the fracture surfaces were marked as Q1, Q2, Q3, and Q4, the actual regions can be divided as brittle fracture regions where the fatigue crack initiated, ductile fracture regions corresponding to a low cycle fatigue propagation, or regions of failure caused at the end of the test when the sample was failed manually for removal from the CIRFT. The closeness in texture seen in the opposite quadrants also helps illustrate how the fatigue failure might have initiated, propagated, and failed. Thus, from Figure F-48, Figure F-50, Figure F-51, and Figure F-52, it can be inferred that crack initiation occurred on the ID in both Q2 and Q4 but that the crack propagation started in Q2, slowly at first, creating the large flat region in Q2, and then increasing in velocity through regions in Q1 and Q3 towards Q4, creating a rougher crack surface with some indications of ductile failure where final failure occurred.

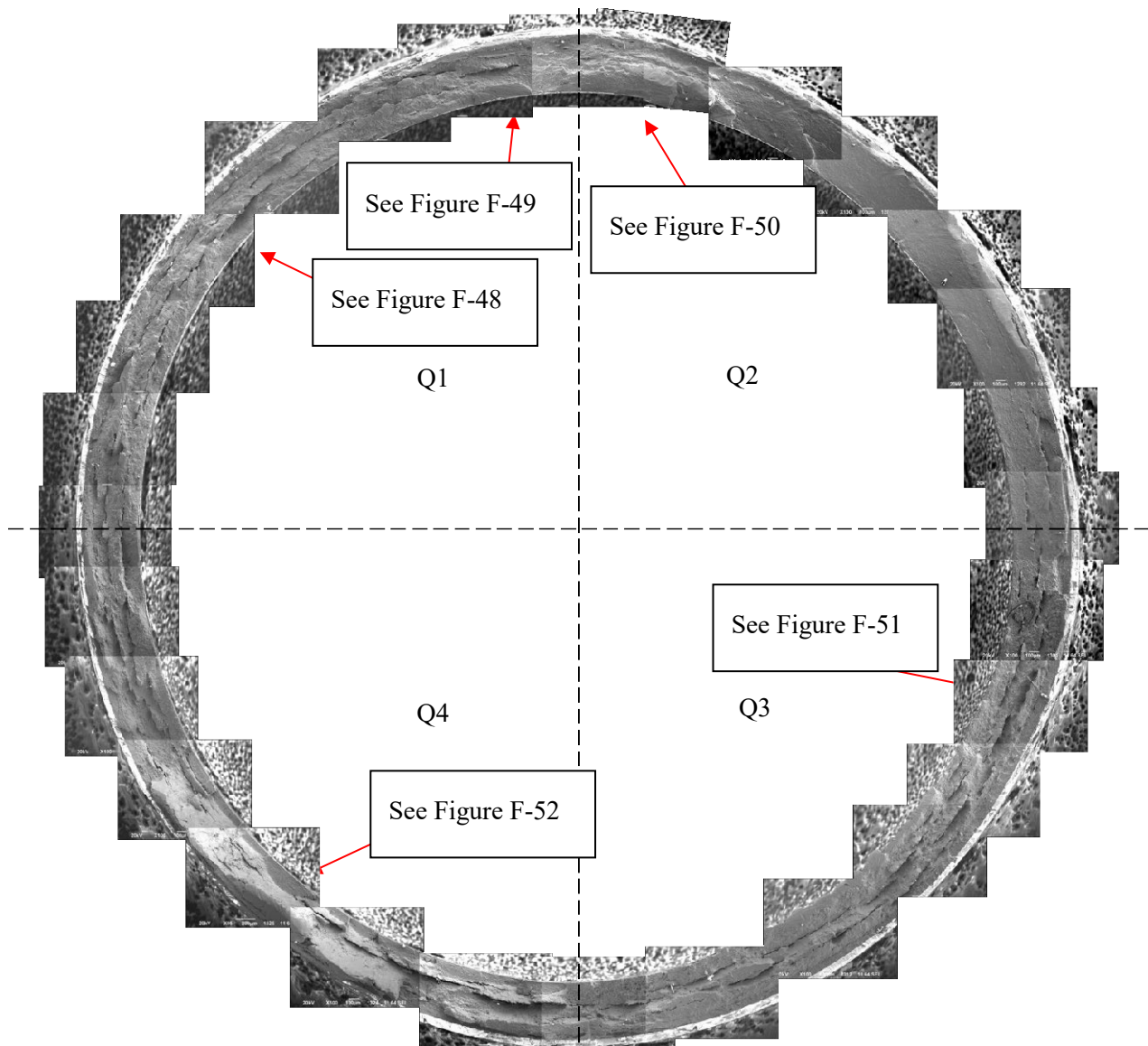


Figure F-47. Montage (100x) of the surface of the fatigue failure in dogbone sample DE50017. The areas identified in the various quadrants were investigated at higher magnification.

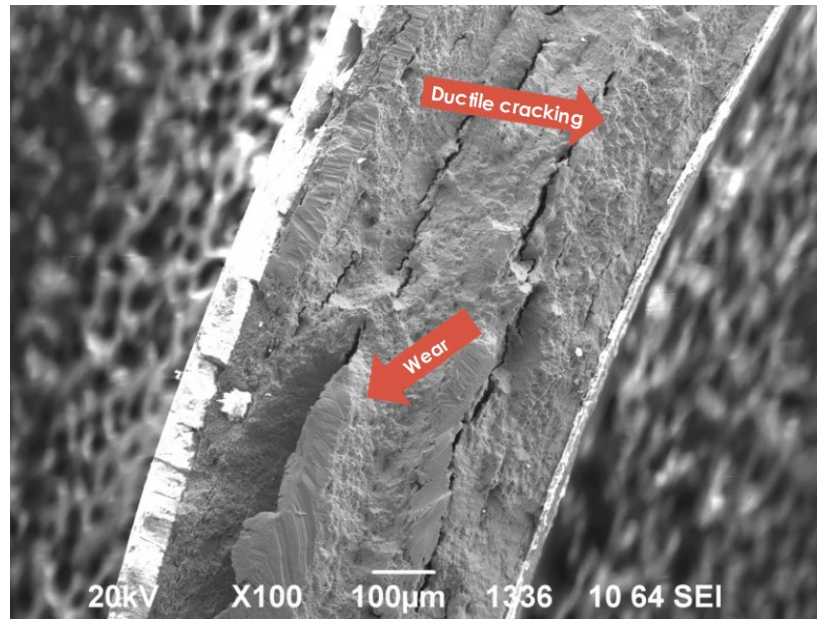


Figure F-48. Ductile regions and wear marks of Q1 in sample 3A1F05-2025-2178.

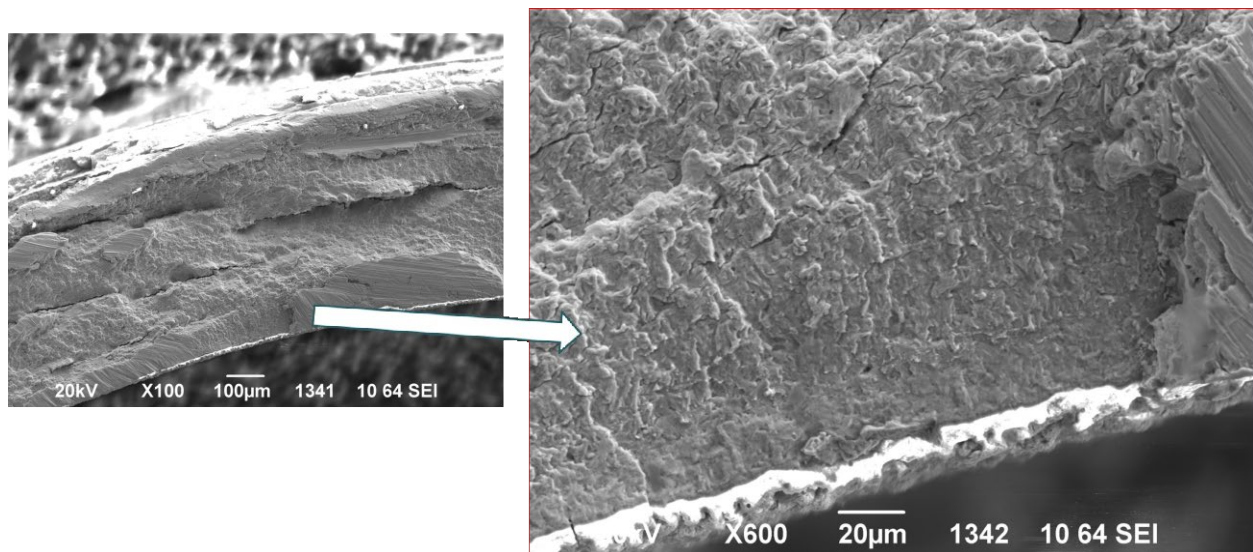


Figure F-49. Fuel-side brittle regions of Q1 (approaching Q2) in sample 3A1F05-2025-2178.

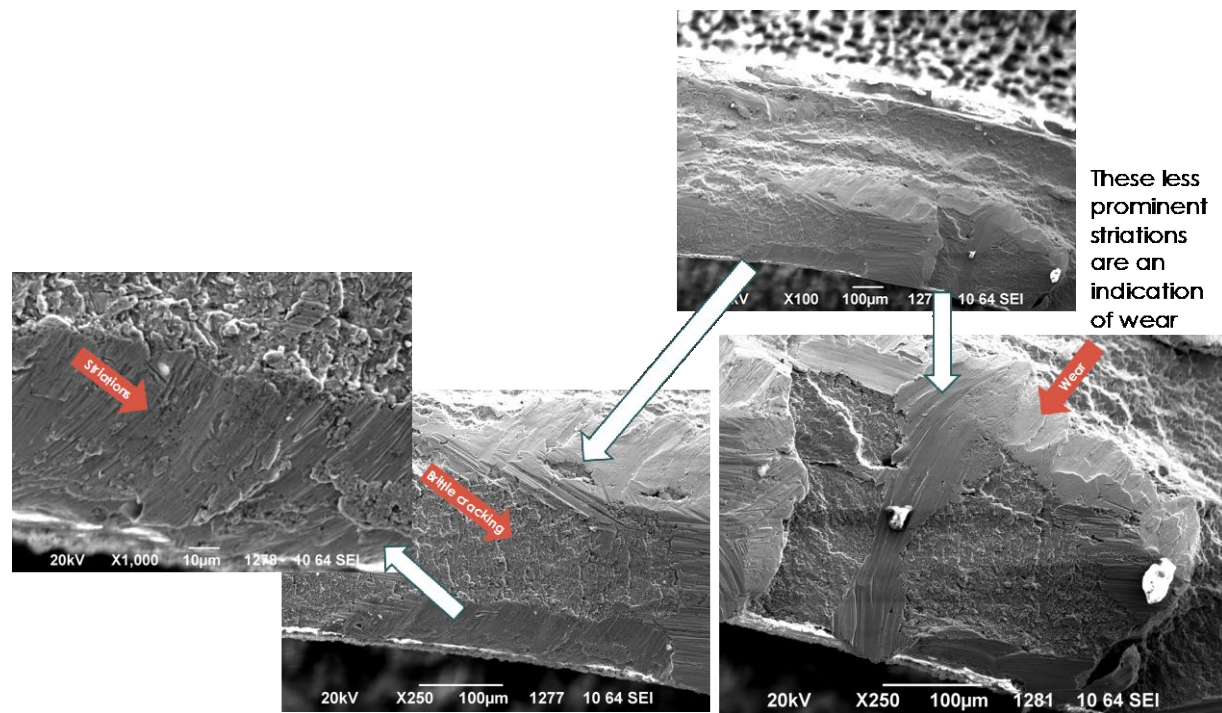


Figure F-50. Cleavage-like regions, apparent fatigue striations, and flat wear marks on the fuel side of Q2 in sample 3A1F05-2025-2178.

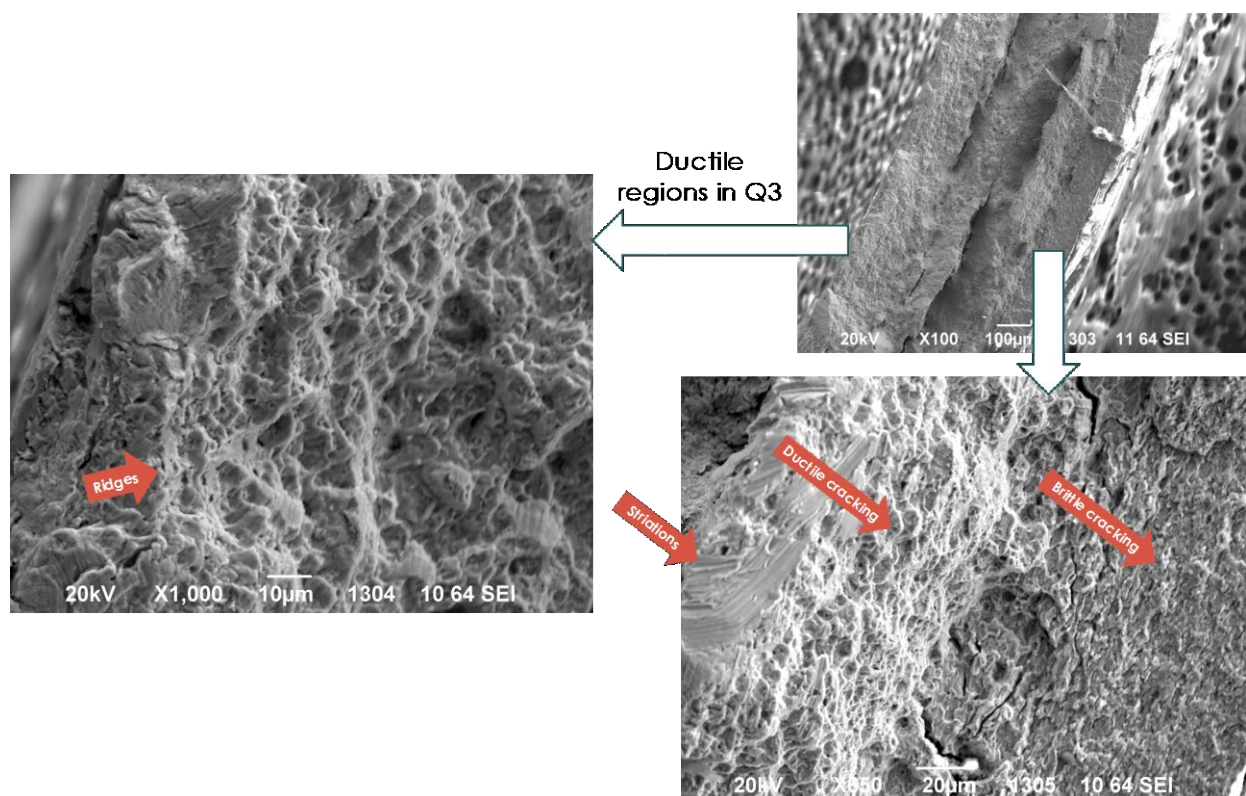


Figure F-51. Ductile fracture regions amidst striations and brittle cracks on Q3 in sample 3A1F05-2025-2178.

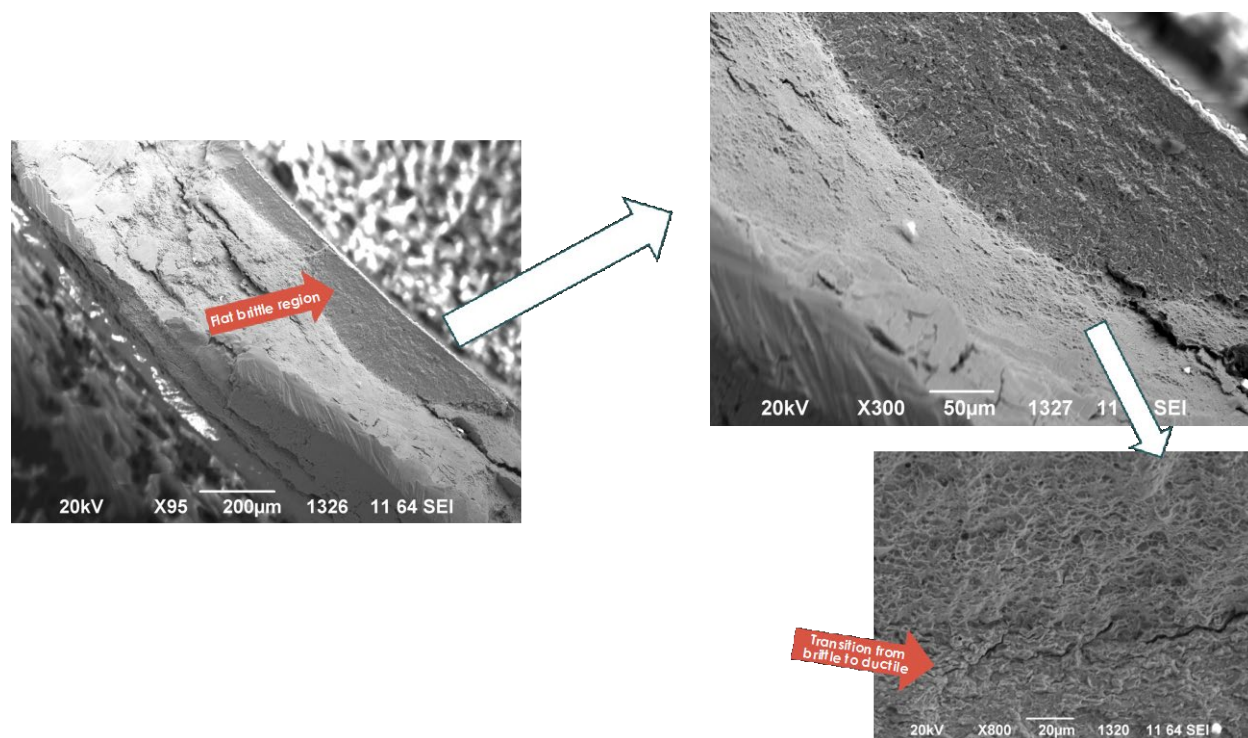


Figure F-52. Flat cleavage-like regions on the fuel side leading to cracks and ductile failure seen on Q4 in sample 3A1F05-2025-2178.

F-8.5.4 Fractography of unirradiated Zirc-4 CIRFT specimens

Two unirradiated fuel cladding samples were tested for fatigue until failure (see Section F-5.1) and were characterized using SEM. This section discusses major insights from the SEM data and draws certain conclusions from comparison with fueled sample fractography analysis.

The samples were unirradiated Zirc-4 cladding tested at 0.46% and 0.40% strain amplitude. One confounding issue is that sample Zr4-W-3 experienced ~6,300 cycles after fatigue initiation and specimen Zr4-W-4 experienced ~4,500 cycles after fatigue initiation; thus, some indication of wear on the fracture surfaces are expected. After the specimen was removed from the CIRFT, a short segment of the tube with the fracture surfaces was cut from the dogbone using a tube cutter and then was mounted onto an SEM fixture for imaging in a manner similar to that used for the fueled CIRFT sample, as described in Sections F-8.5.2 and F-8.5.3.

F-8.5.4.1 Zr4-W-4

Figure F-53 shows a montage of images taken at 100× magnification around the fracture surface of sample Zirc-4-W-4. The sample was divided into four quadrants to make it easier to identify different regions of interest. Certain firsthand observations can be made from Figure F-53:

- The highest strains occurred in the planer region in Q4, suggesting that the fatigue crack initiated in this area and then propagated through Q1 and Q3.
- The long circumferential striations observed in Q2 and Q3 adjacent to the diagonal markings correspond to a change in the crack plane, as illustrated in Figure F-54, where the region is matched with the side view of the failed specimen in the CIRFT machine.

Figure F-55 shows the crack initiation region in Q4. This region can be seen as a damaged region on the ID, with long branch-like radial beach marks extending into the cladding surface. The OD region of the

fractured surface seems to be flatter with straight striations, which might be associated with crack propagation in the circumferential direction. Figure F-56 is a tilted image showing the ID side of the crack initiation region. Surface damage can be observed on the ID below the crack surface, along with localized regions of surface damage extending well below the crack surface. This suggests a line of ID surface damage at the point on the cladding where the maximum strain occurred. In future exams, the ID surface in Q1 that is $\sim 90^\circ$ from the initiation and in Q2 that is 180° from the initiation site will be examined to compare these observations with a surface on the neutral axis and one where similar strain occurred. Figure F-56 shows the flat fracture regions in Q1. The flat fracture surface can be associated with a slow initial propagation rate of fatigue. This observation is supported by the increased fracture surface roughness seen in Q2 and Q3 before failure when the propagation rate is higher. Figure F-57 also shows flat, featureless marks in between the brittle regions. These might be caused by wear from the cycles that occurred after failure.

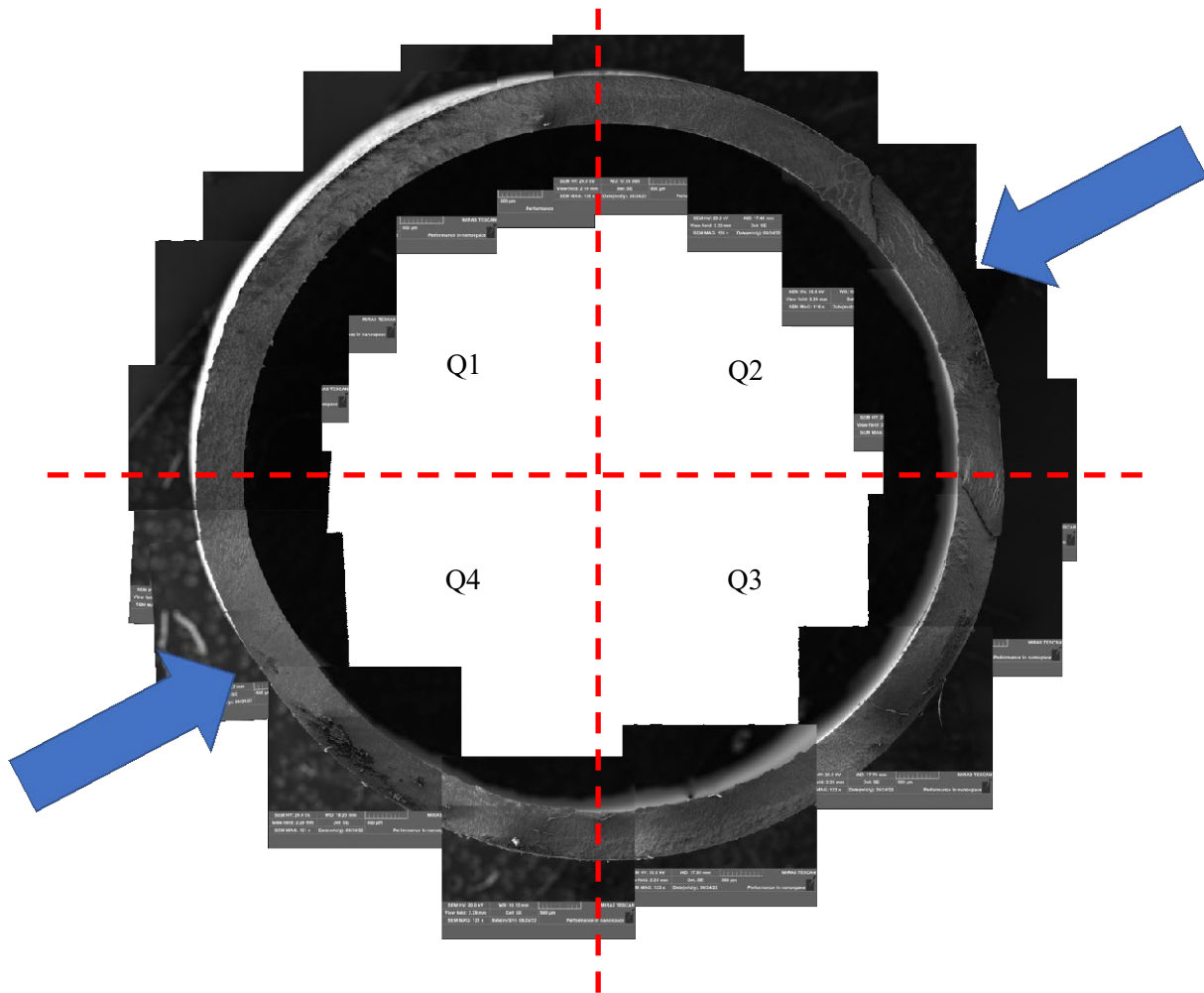


Figure F-53. Montage (100 \times) of the surface of the fatigue failure in dogbone sample Zirc-4-W-4. Arrow marks show regions of high bending strain in the sample.

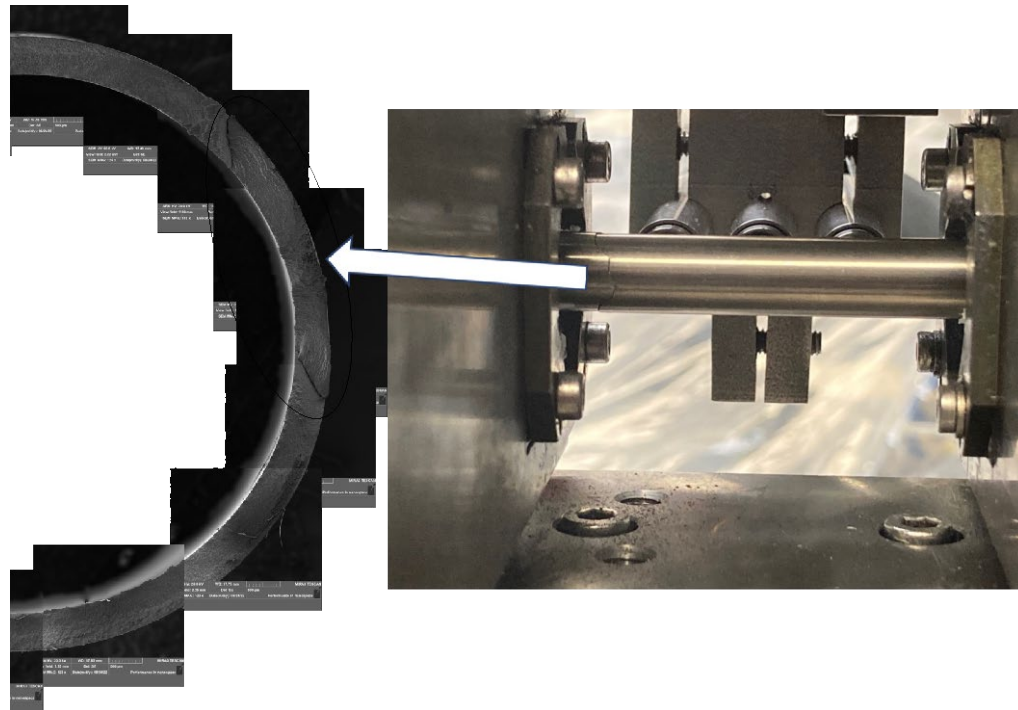


Figure F-54. Top (fracture) view and side view of the fatigue failure region in Q2 and Q3 of sample Zirc-4-W-4.

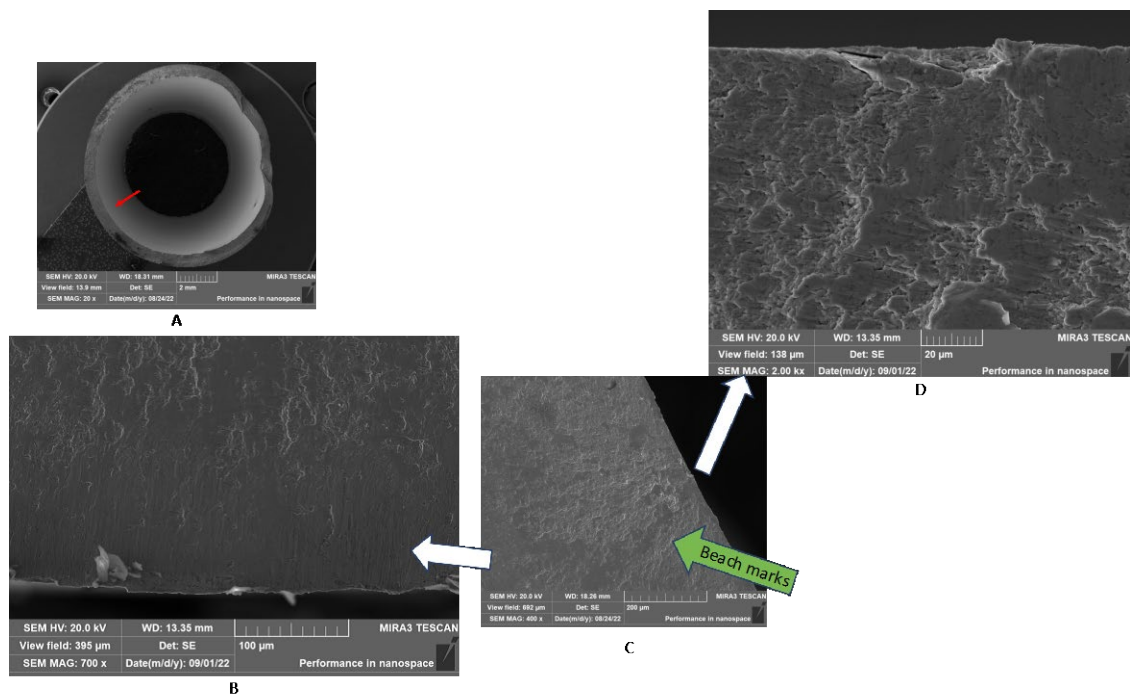


Figure F-55. Fatigue crack initiation region in Q4 of sample Zirc-4-W-4: (A) location of the region in a low-magnification image of the sample, (B) OD side of the fatigue failure initiation site, (C) ID side of the fatigue crack initiation site, and (D) detailed view of C.

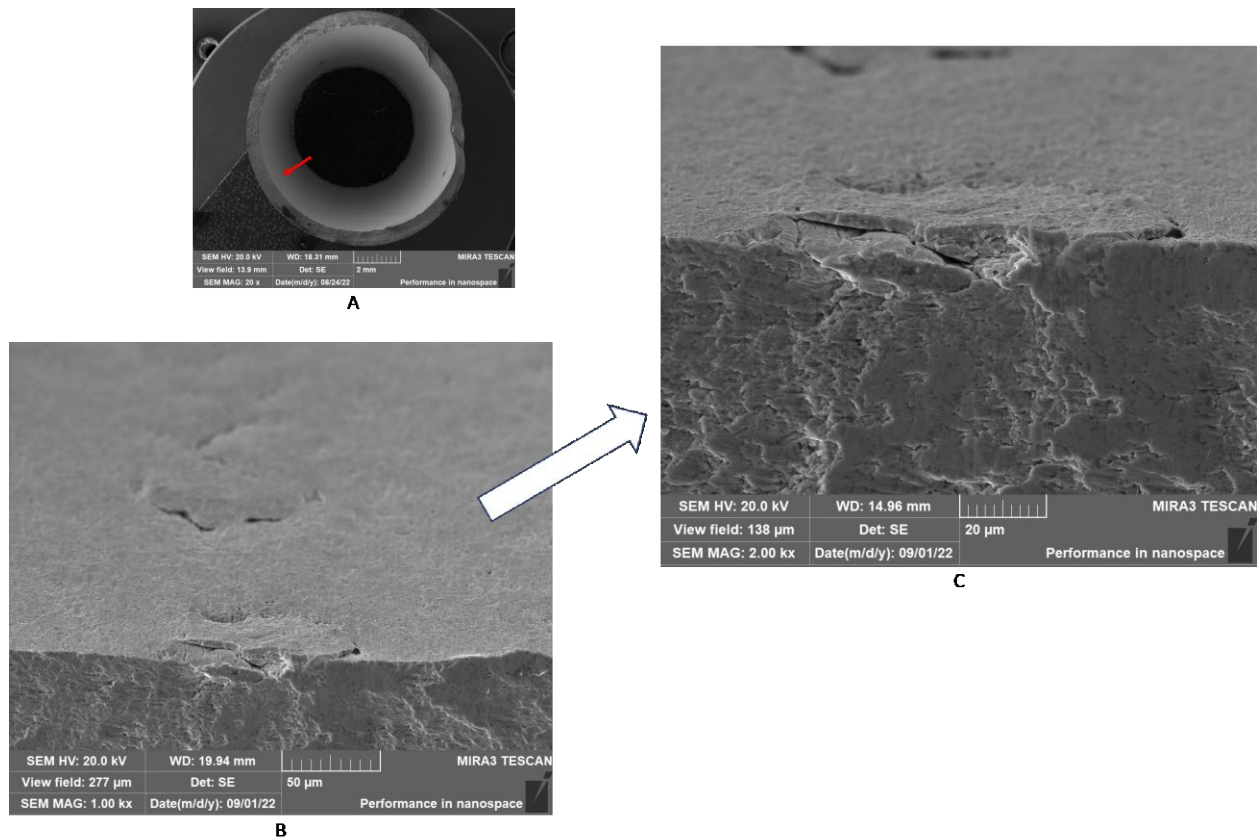


Figure F-56. Tilted image of Figure F-54 revealing the ID side of the fatigue failure initiation site on sample Zirc-4-W-4: (A) location of the region in a low-magnification image of the sample, (B) ID side of the fatigue failure initiation site, and (C) detailed view of the fatigue failure initiation fracture surface.

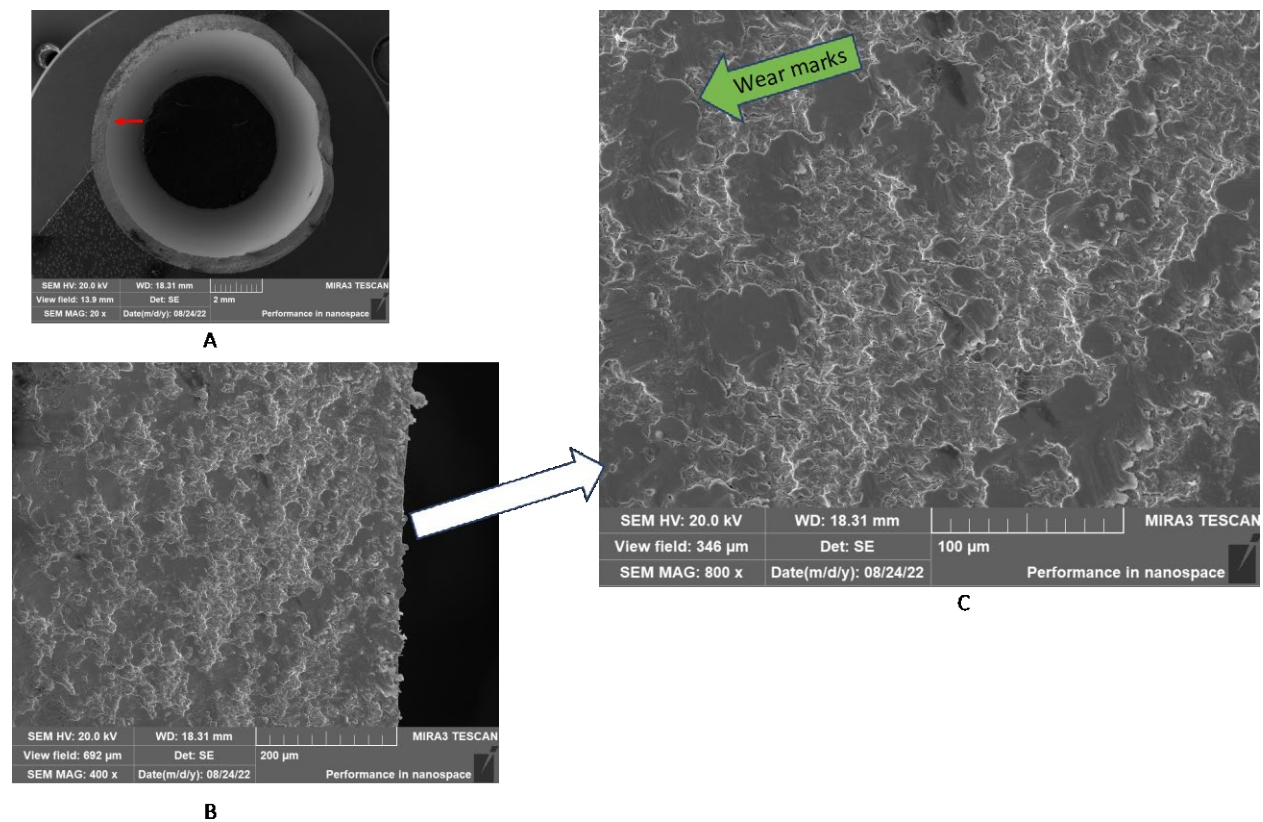


Figure F-57. Brittle fracture regions and potential wear marks of sample Zirc-4-W-4: (A) location of the region in a low-magnification image of the sample, (B) brittle or cleavage-like regions on Q1, and (C) potential wear marks observed between the brittle regions in Q1.

F-8.5.4.2 Zr4-W-3

Figure F-58 is a montage of images taken at 100× magnification around the fracture surface of sample Zirc-4-W-3. The montage is divided into four quadrants to make it easier to identify different regions of interest. As in sample Zirc-4-W-4, the planer region in Q4 in sample Zirc-4-W-3 is where the highest strains occurred, suggesting fatigue crack initiation in this area. In fact, a similar initiation feature is observed on the ID of this sample in Q4. The fatigue crack is thought to have propagated through Q1 and Q3, leading to the final failure features observed in Q2 and Q3. In Figure F-59, the final failure region is matched with the side view of the failed specimen in the CIRFT machine.

Figure F-60 shows the fatigue initiation region in sample Zirc-4-W-3. The initiation can be seen as long brittle cracks originating from the ID and radial beach marks propagating towards the OD, similar to that observed in sample Zirc-4-W-4. Furthermore, the sample periphery was analyzed to discern the relation of fatigue initiation to the maximum bending strain direction. As expected, the LVDT marks that correspond to the sample loading position in the CIRFT rig can be seen exactly opposite to the failure initiation site (Figure F-61). Figure F-62B shows the OD side of the fracture surface near the fatigue initiation site of sample Zirc-4-W-3. This region has some radial striations similar to those observed in sample Zirc-4-W-4 at the same location; the orientation of the straight striations indicates that the fatigue crack propagated in the circumferential direction in this region. Figure F-62D is a tilted image showing the ID side of the crack initiation region where surface cracks can be seen along the length of the ID. Although this feature is similar to that observed in sample Zirc-4-W-4, sample Zirc-4-W-3 had a higher density of localized surface damage extending well below the crack surface. In addition, the initiation site in sample Zr4-W-3 looks different than Zr4-W-4. Clear void-like features can be observed very near the surface in Figure F-62D, indicating ductile failure. The transition from void-like features to planar cleavage-like features is striking. Future work is proposed to probe this ductile region further by employing focused ion beam machining and characterizing the regions underneath and around the site to look for localized bulk effects contributing to the crack initiation process. Also, electron backscatter diffraction is proposed to obtain texture maps of the fracture surface to determine whether the propensity of crack propagation is inter- or intra-granular.

Figure F-63 shows the fatigue striations in Q1 amidst brittle or cleavage-like regions. The striations can be associated with the fatigue propagation process around this quadrant. There is also evidence of flat wear marks in between the brittle regions. This is thought to be caused by wear during the cycles after failure.

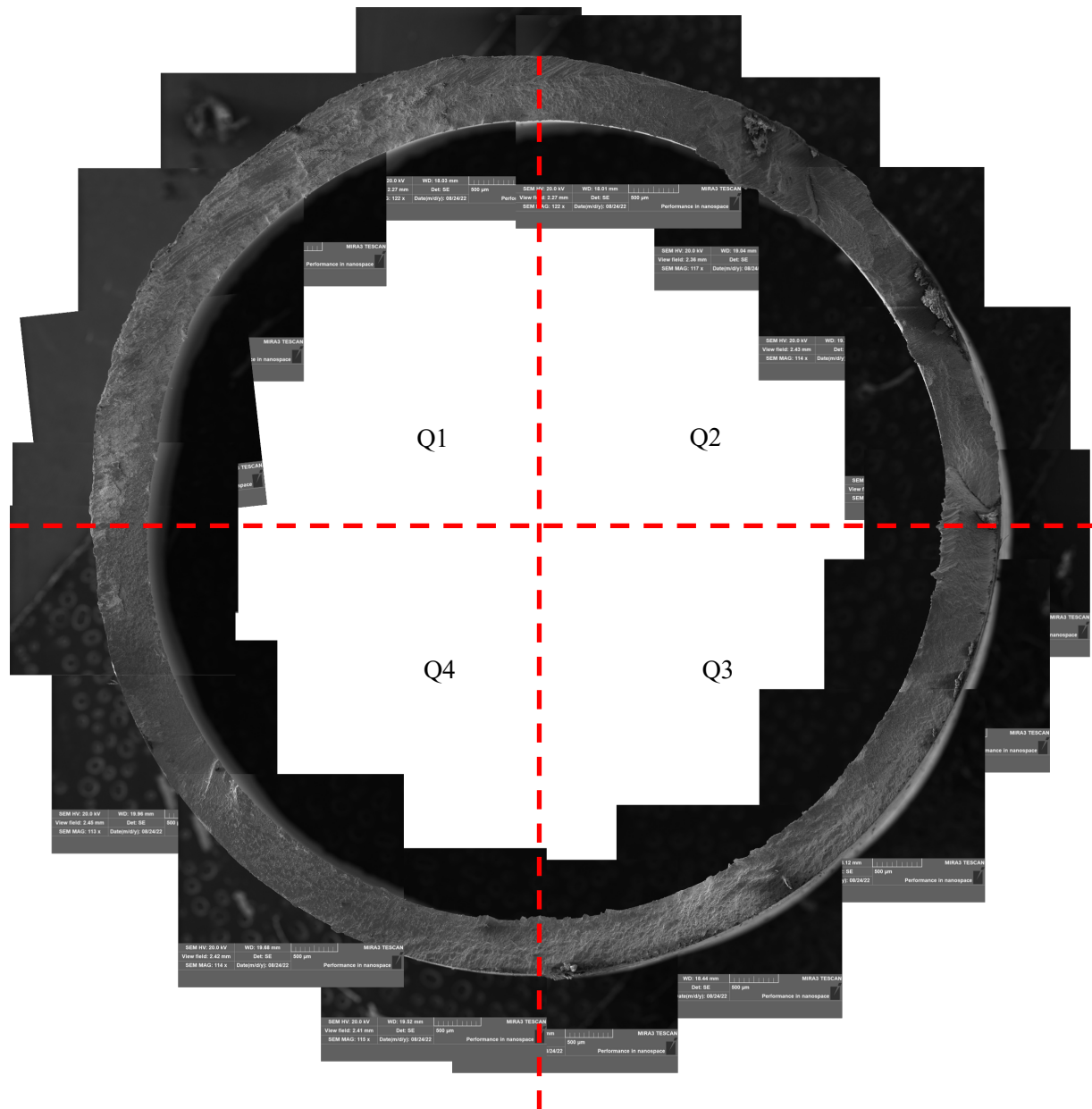


Figure F-58. Montage (100x) of the fatigue failure surface in dogbone sample Zirc-4-W-3.

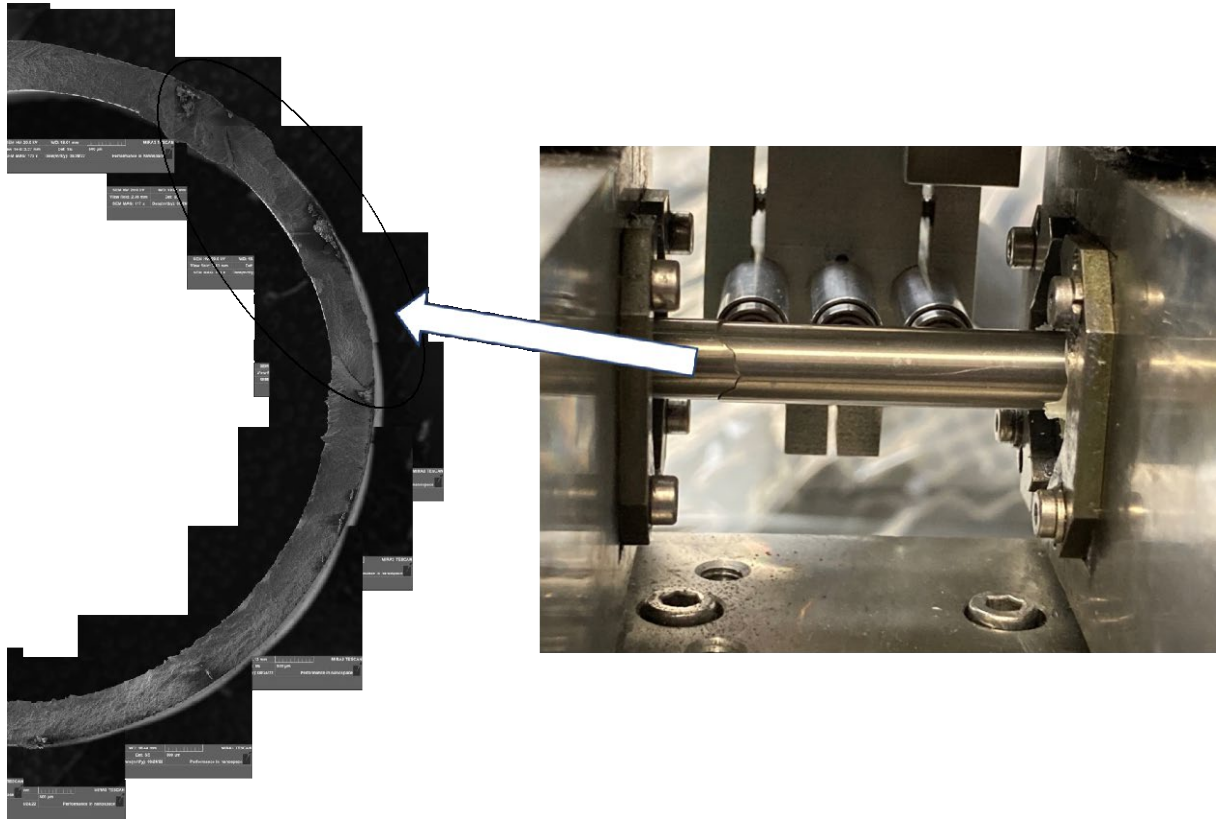


Figure F-59. The top (fracture) view and side view of the fatigue failure region in Q2 and Q3 of sample Zirc-4-W-3.

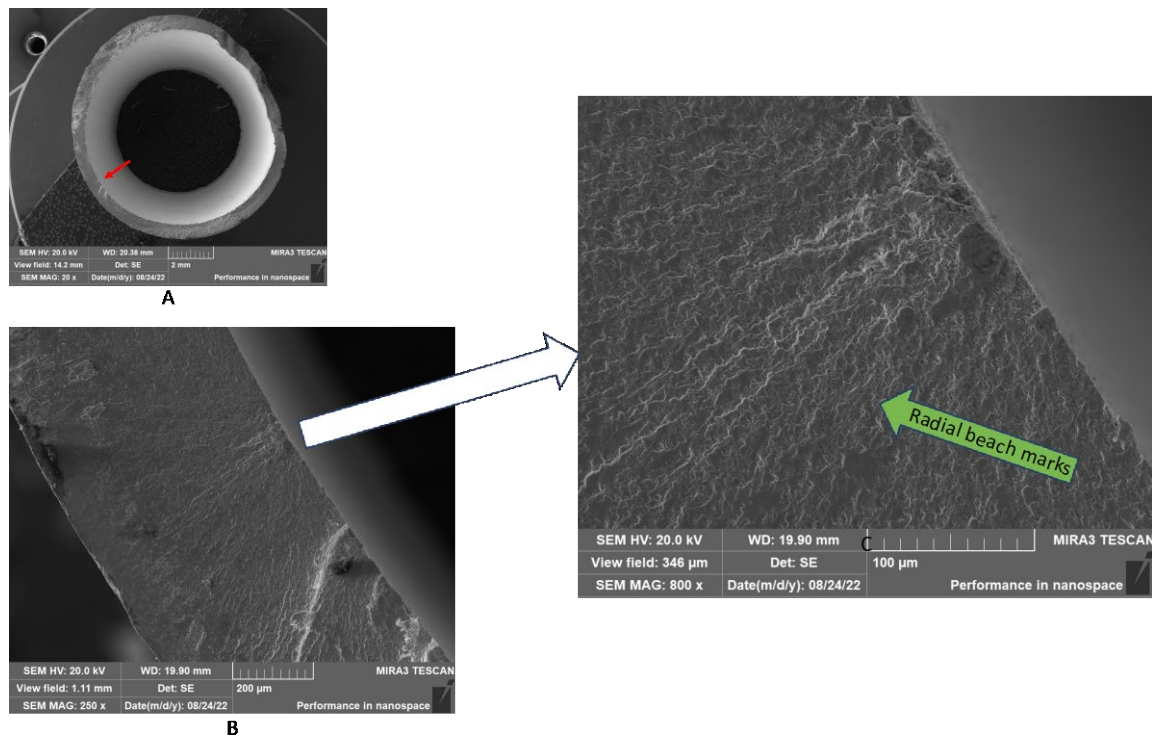


Figure F-60. Fatigue crack initiation region in Q4 of sample Zirc-4-W-3: (A) location of the region in a low-magnification image of the sample, (B) ID side of the fatigue crack initiation site, and (C) detailed view of B.

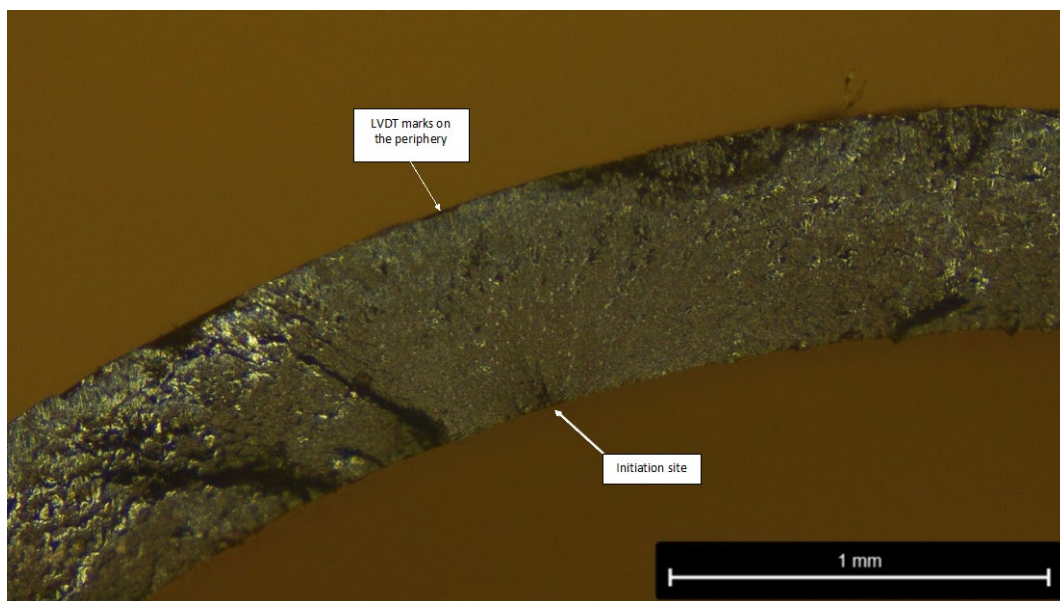


Figure F-61. Optical microscope image of sample Zirc-4-W-3 showing the fatigue failure initiation site; the peripheral region containing the LVDT marks is not visible.

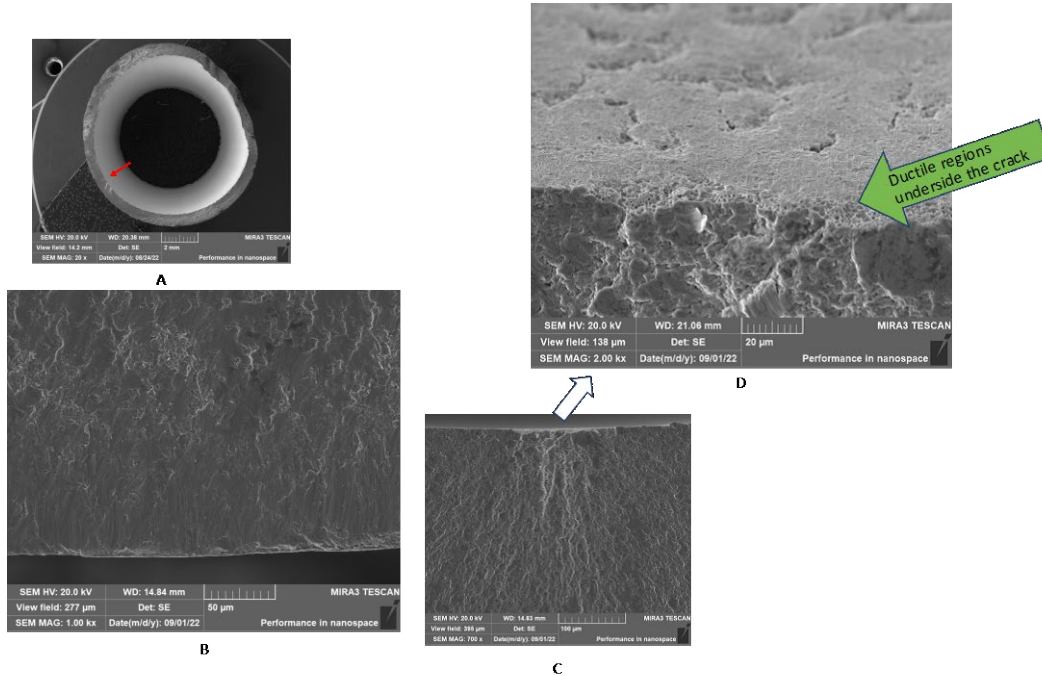


Figure F-62. Tilted SEM image of Figure F-60 revealing the ID side of the fatigue failure initiation site of sample Zirc-4-W-3: (A) location of the region in a low-magnification image of the sample, (B) OD side of the fatigue failure initiation site, (C) ID side of the fatigue initiation site, and (D) inside of the ID side of sample Zirc-4-W-3 at the fatigue initiation site.

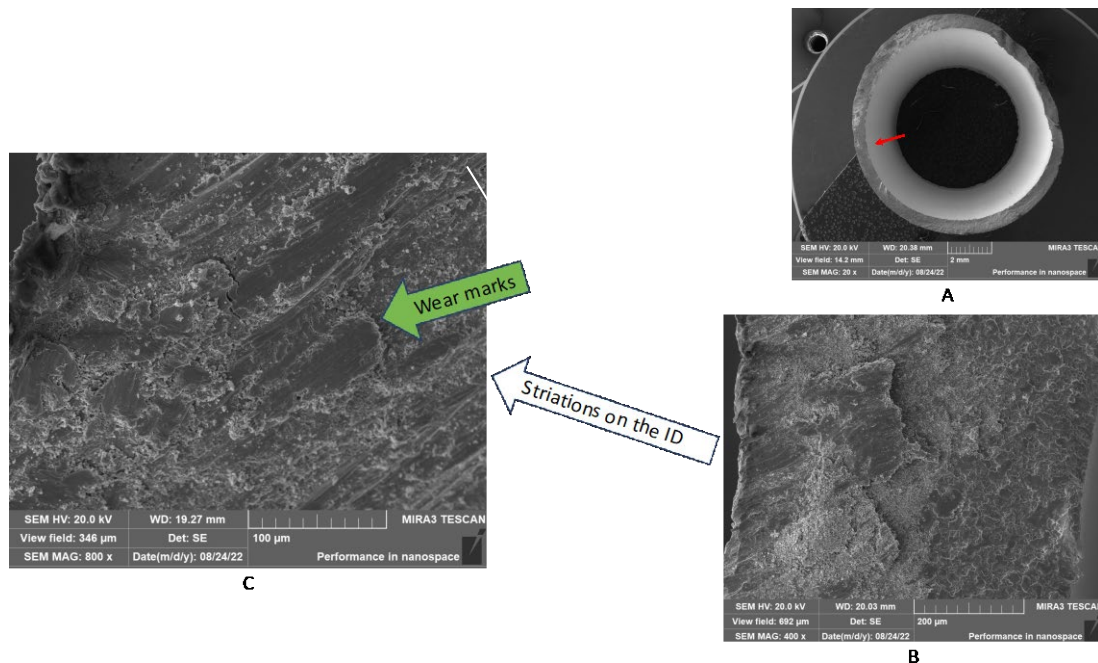


Figure F-63. Some striations visible amidst brittle or cleavage fracture-like regions and wear marks of sample Zirc-4-W-3: (A) location of the region in a wide field view of the sample, (B) wear marks observed on the ID with striations on the OD and brittle fracture regions in the middle of Q1, and (C) detailed view of the flat wear-like features between striations.

F-8.5.5 Future work

As part of understanding the fatigue failure mechanisms in SNF rods, ORNL plans to further characterize the brittle fracture regions (e.g., as described in Figure F-49 and Figure F-52).

Additionally, sample 6U3K09-2310-2463 presents a unique opportunity to probe the fatigue initiation and propagation sites from an underdeveloped failure, seen as a second crack on the sample (Figure F-64) and sectioned image (Figure F-65). This ZIRLO sample failed under a high load of 12.7 N-m at a pellet-pellet interface, near the grip of the CIRFT test gauge section, and its fatigue life (17,500 cycles) was consistent with previous test data. The fatigue initiation occurred in the last 1,000 cycles.

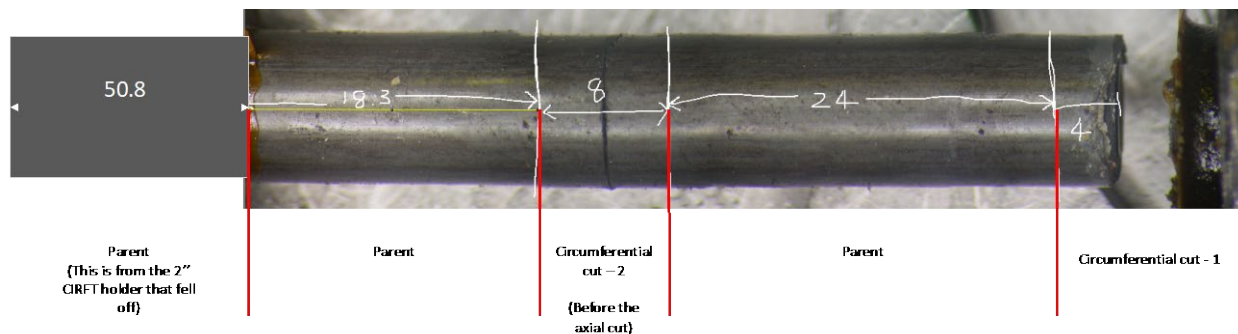


Figure F-64. Fatigue failure in sample 6U3K09-2310-2463 showing the second crack observed in the sample.

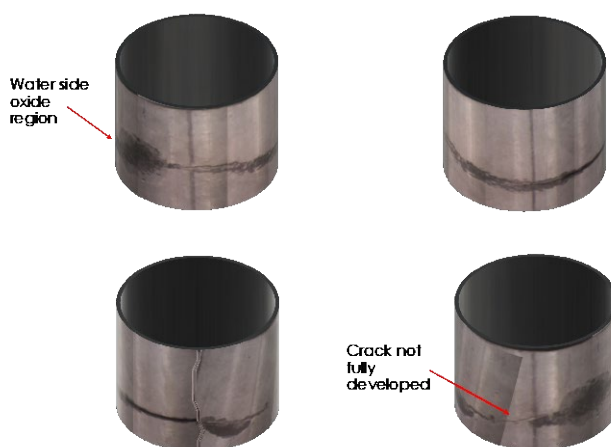


Figure F-65. Images of the circumferential cut-2 from sample 6U3K09-2310-2463 wrapped around a 3D cylinder to show a realistic image.

F-9. CIRFT Cumulative Effects Fixture Development

Equipment for performing the cumulative shock tests, as shown in Figure F-66, was developed and is currently being tested out of cell. The design incorporates an electromagnet and weight and uses gravity to deliver one or more impacts to the CIRFT specimen before fatigue testing. The parameters for the impact (e.g., impact load, number of impacts) have not yet been established. To help determine the necessary drop height, impactor weight, and impactor weight geometry for postulated normal condition impacts, a finite element model was developed for the impact system. The model and results are discussed in the following sections.

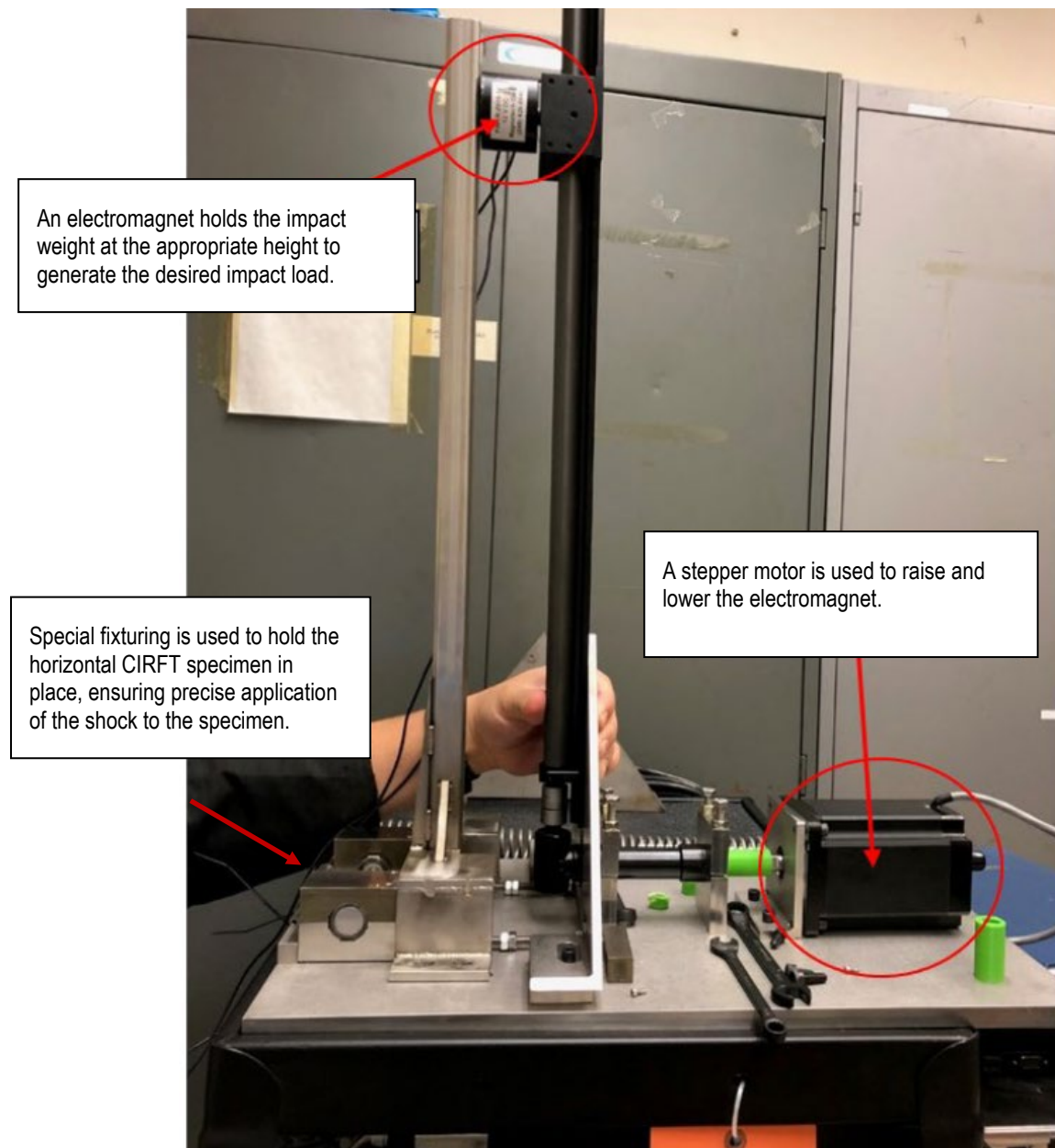


Figure F-66. Cumulative shock fixture developed to apply a normal transport condition shock before fatigue testing.

F-9.1 Finite Element Modeling of the Cumulative Impactor

An impact analysis of the cumulative impactor was performed using a nonlinear dynamic FEA. Solid eight-node elements and shell four-node elements are used for all the models in which structure failure modes can be simulated during the impact.

The cumulative impactor model includes the impactor weight, a fuel rod test segment, and supports/restraints representing the lower bed of the impactor, as shown in Figure F-67. The fuel rod is supported by guide blocks at both ends. The cumulative impactor weight was centered over the rod and at a variable height above the outer surface of the cladding. Several different impactor end geometries were evaluated, including:

- a. Grid strip wall with dimples (shown in Figure F-67)
- b. Grid strip wall without dimples
- c. Rectangular weight only (the brown feature shown in Figure F-67)
- d. Plate with dimples
- e. Plate without dimples

These studies are focused on determining the g-load on the rod segment for various cumulative impactor conditions to determine whether such conditions reflect expected normal conditions of transport. Per Kalina et al. [F-16], the normal condition g-loads experienced during transport of the SNF are less than 15 g and more typically less than 3 g.

F-9.1.1 Finite Element Modeling Software

A nonlinear finite element model was developed using ANSYS Workbench. The dynamic analysis with time integration and contact configuration is used to solve the transient impact problem.

LS-DYNA, developed by Livermore Software Technology Corporation (LSTC), is a multipurpose explicit and implicit finite element program used to analyze the nonlinear response of structures. Its fully automated contact analysis and wide range of material models enable users worldwide to solve complex real-world problems. It is used by the automobile, aerospace, construction, military, manufacturing, bioengineering, and nuclear industries. LS-DYNA is optimized for shared and distributed memory on Unix-, Linux-, and Windows-based platforms, and it is fully qualified by LSTC. The code's origins lie in highly nonlinear, transient dynamic FEA using explicit time integration [F-19].

LS-DYNA has an extensive material library that includes metals, plastics, glass, foams, fabrics, elastomers, honeycombs, concrete and soils, viscous fluids, and user-defined materials.

LS-DYNA has been widely used in various applications, including automotive crashworthiness and occupant safety, metal forming, aerospace (e.g., blade containment, bird strike, failure analysis), drop testing, nuclear shipping container design, metal cutting, earthquake engineering, offshore platform design, and sports equipment design.

Because impact is a transient structural dynamics problem that involves large deformation of solid structures and nonlinear material behavior, LS-DYNA was chosen to perform the impact analysis of the cumulative impactor.

F-9.1.2 Finite Element Model

Structurally insignificant features such as small curves and lines such as fillets and chamfers were omitted from the finite element model. The omitted features are small and are not expected to significantly influence the structural response. The mesh element size near the impact zone was 0.5 mm; all other element sizes ranged from 0.5 to 2 mm. The cladding was modeled using linear shell elements.

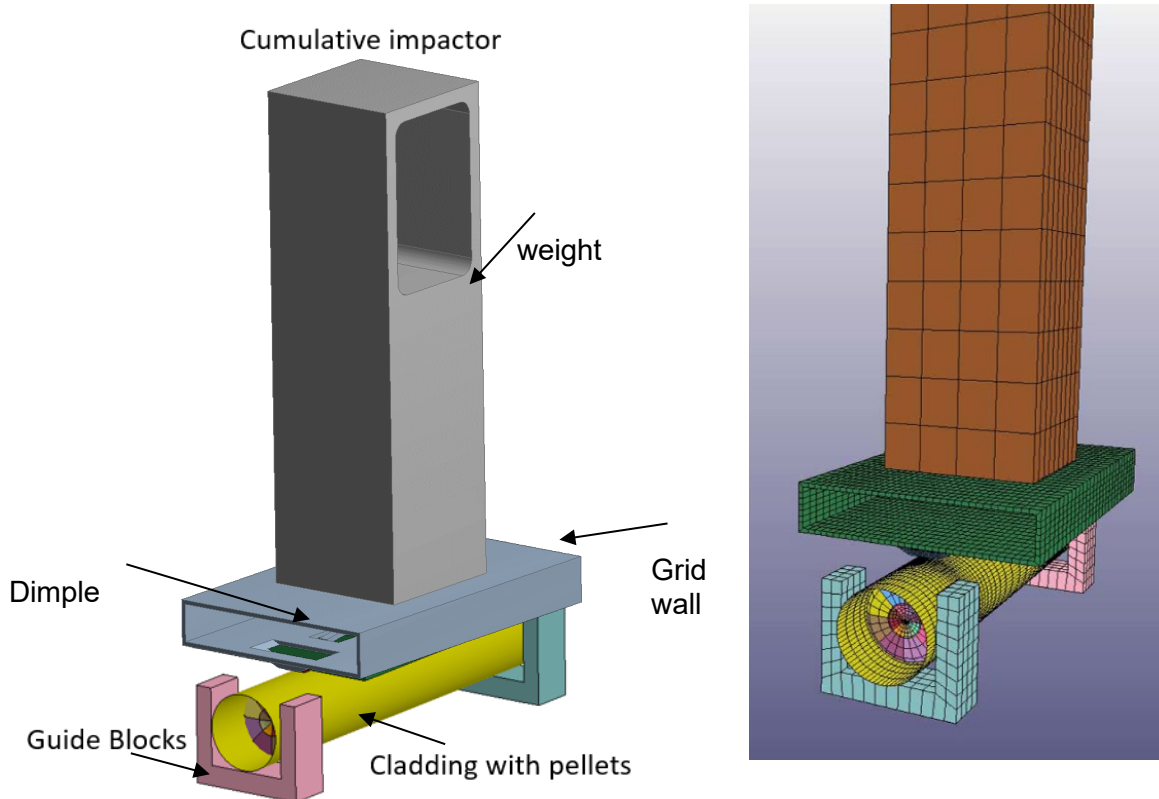


Figure F-67. The cumulative impactor CAD model (left) and finite element model (right) include a rod segment with discrete pellets, guide blocks, and a weight with impact geometry.

The units and values used for the simulations are:

- mass, kg
- length, m
- time, s
- force, N
- stress, Pa
- energy, Joule
- density, kg/m³
- elastic modulus, Pa

The cumulative impactor was modeled as separate parts, with the surface-to-surface interfaces modeled using the bonded surface-to-surface connection. The surface-to-surface connections in the finite element model cannot deform, but they can break in accordance with the user-input stress criteria. The model uses various contacts to model the interaction between the elements. Automatic single-to-surface contact is an all-purpose contact used to model component interaction. Friction in LS-DYNA is modeled through the classic Coulomb friction model. In the cumulative impactor fuel rod segment model, contacts between the pellet-to-pellet and pellet-to-cladding contacts were assigned a static friction coefficient of 0.95 and a

dynamic friction coefficient of 0.85 to simulate a relatively rigid system. The friction values are being investigated with other models; these values might not be entirely representative of the actual frictional contact, but they are considered acceptable for the purposes of this work.

F-9.1.3 Material Models

The cladding, spring, and dimples are modeled as Zirc-4; the pellets are modeled using a response profile similar to concrete, which is load-bearing in compression and has a lower strength in tension; and the cumulative impactor is modeled as stainless steel. The pellets are modeled with a concrete material property as a surrogate for UO₂. The compression strength of the pellets was 15 Mpa, with an aggregate grain size of 25.4 mm.

To model the plastic deformation of metal materials, the LS-DYNA code needs the true stress-strain curve of the material. Up to the maximum point on the engineering stress-strain curve, a uniform elongation and a uniform area reduction occur. The minimum true stress-strain curve used is based on the model provided in the American Society of Mechanical Engineers (ASME) Boiler and Pressure Vessel Code Section VIII, Div. 2, Annex 3-D [F-20], which uses the minimum yield stress, minimum ultimate tensile stress, and elastic modulus of the material at the specified temperature. The true stress-strain curves obtained with this model are valid up to the value of the true ultimate tensile stress at true ultimate tensile strain.

The LS-DYNA material model used in the analysis is the *MAT_PIECEWISE_LINEAR_PLASTICITY, also known as *MAT_024. This material model prompts the user to specify the elastic modulus, Poisson's ratio, yield stress, and failure strain of the material. When the calculated element's plastic strain reaches the specified failure strain, the material has failed, and the element is deleted from the analysis. Additionally, the effective stress vs. plastic strain curve must be entered as a *DEFINE_CURVE entry.

Following the ASME model, a true stress-strain curve was developed for stainless steel and Zirc-4 using the minimum yield strength, minimum ultimate tensile strength, and elastic modulus of the material in Table F-17 [F-21]; the curve is shown in Figure F-68. Before the true stress-strain curve was entered into LS-DYNA, the elastic portion of the strain was subtracted from the total strain to develop the effective plastic strain used by LS-DYNA.

Table F-17. Cumulative Impactor Model Minimum Material Properties.

Material properties				
Material	Minimum yield stress (MPa)	Minimum ultimate stress (MPa)	Elastic modulus (GPa)	Reference
304	106	392	172	[F-20],[F-21]
Zirc-4	241	413	99.3	[F-20],[F-21]

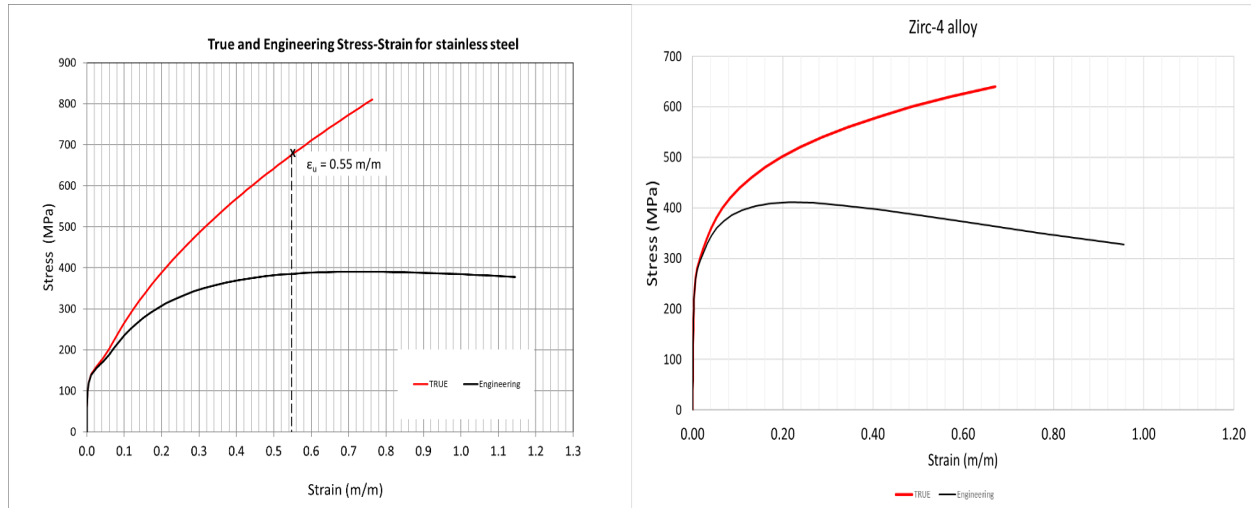


Figure F-68. 304 stainless steel (left) and Zirc-4 (right) true stress-strain curves used compared with corresponding engineering stress-strain curves.

F-9.1.4 Initial Conditions, Boundary Conditions, and Load Cases

All simulations were completed using room temperature material properties. A gravity load of 9.81 m/s^2 was applied to all components in the finite element model. The guide rods were constrained in all three directions using the *BOUNDARY_SPC_SET keyword. The fuel rod segment was placed on the guide blocks with full frictional contact.

F-9.1.5 Load Cases

The impact of the weight was studied using nine load cases, as listed in Table F-18, for each of the impactor end geometries. Load cases 1–4 correspond to a maximum cumulative impactor weight of 0.11 kg, with height increasing from 0.15 to 0.61 m (0.5 to 2.0 ft). Load cases 5–7 correspond to a 25% reduction in the cumulative impactor weight with increasing drop height. The cumulative impactor mass for load case 8 was reduced by 50% when compared with load case 1, and the drop height was 0.15 m (0.5 ft). Finally, for load case 9, the mass for the cumulative impactor was reduced by 75% when compared with load case 1, and the drop height was 0.15 m (0.5 ft).

Table F-18. Cumulative Tester FEA Load Case Summary.

Load case	Impactor mass (kg)	Impactor height (m)
1	0.107	0.15
2	0.107	0.30
3	0.107	0.46
4	0.107	0.61
5	0.080	0.15
6	0.080	0.30
7	0.080	0.46
8	0.053	0.15
9	0.027	0.15

F-9.2 Results, Discussion, and Conclusions from the Cumulative Effects Fixture Modeling

The analysis focused on determining the g-load applied to the cladding when subjected to an impact from the cumulative impactor. The cladding g-load for each load case was extracted from the analysis and was plotted as a function of time. The system can dissipate the impact energy in three ways: (1) rebound/deflection of the impactor, (2) bending deflection of the target rod segment, and (3) absorption into the rod cladding and pellets and supporting end blocks. End configurations (a) and (b), described in Section F-8.1, resulted in a significant amount of rebound and the lowest g-load impacts. The concentrated load application in end configuration (c) resulted in rod segment bending, but the g-loads on the rod segment were extremely high. The plate type end configuration, (d) and (e), resulted in high shear loads on the rod segment near the guide blocks that are not considered representative of the target g-load of <15 g.

None of the combinations resulted in a g-load below 20 g. For example, the results from impactor end configuration (d), the plate with dimples, are provided. The impactor-applied g-load as a function of time is provided in Figure F-69 for load cases 1–4 and in Figure F-70 for load cases 5–9. For this impactor geometry, the initial impact takes less than 0.3 ms, after which the weight is rebounded. The g-load on the rod during the impact ranges from 781 to 3,298 g, as listed in Table F-19. Load case 4 has the highest drop height and heaviest weight, and it resulted in the maximum g-load because it had the largest potential energy when compared with the other load cases. Load cases 1, 8, and 9 resulted in a cladding g-load less than 800. All load cases resulted in g-loads greater than 500, with multiple shock waves on the cladding and localized plastic strain on the impactor weight dimples, as shown in Figure F-71.

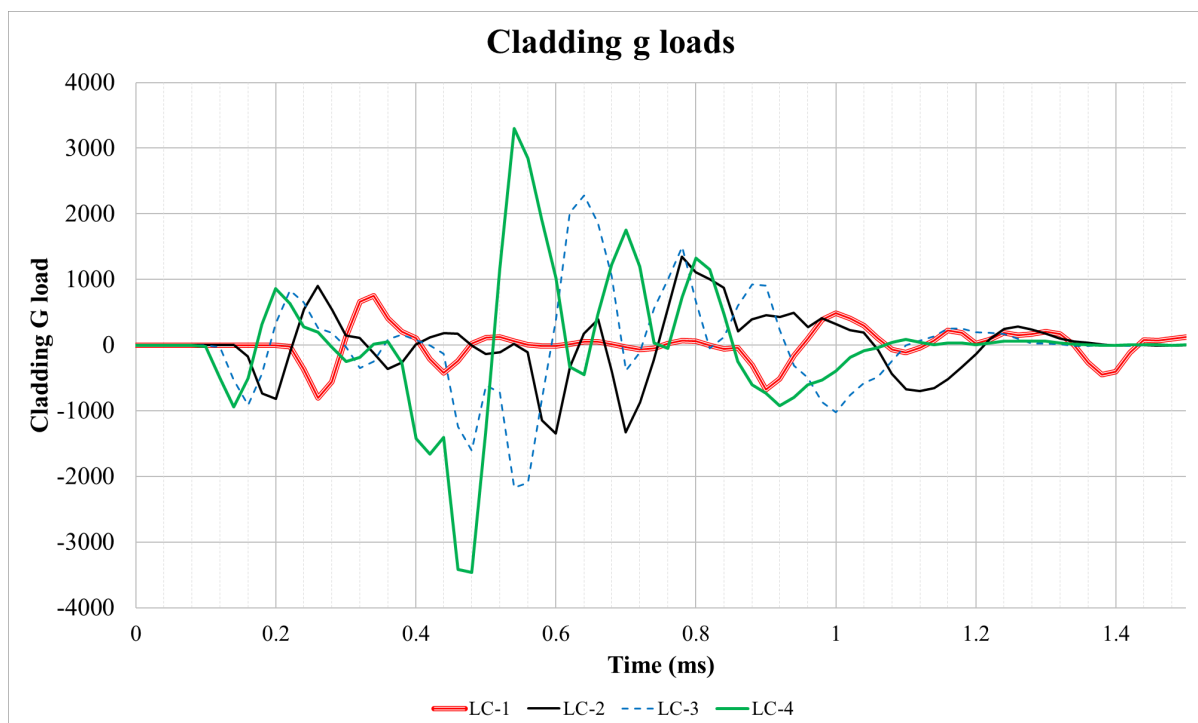


Figure F-69. Impactor end configuration (a) results for g-load cases 1–4.

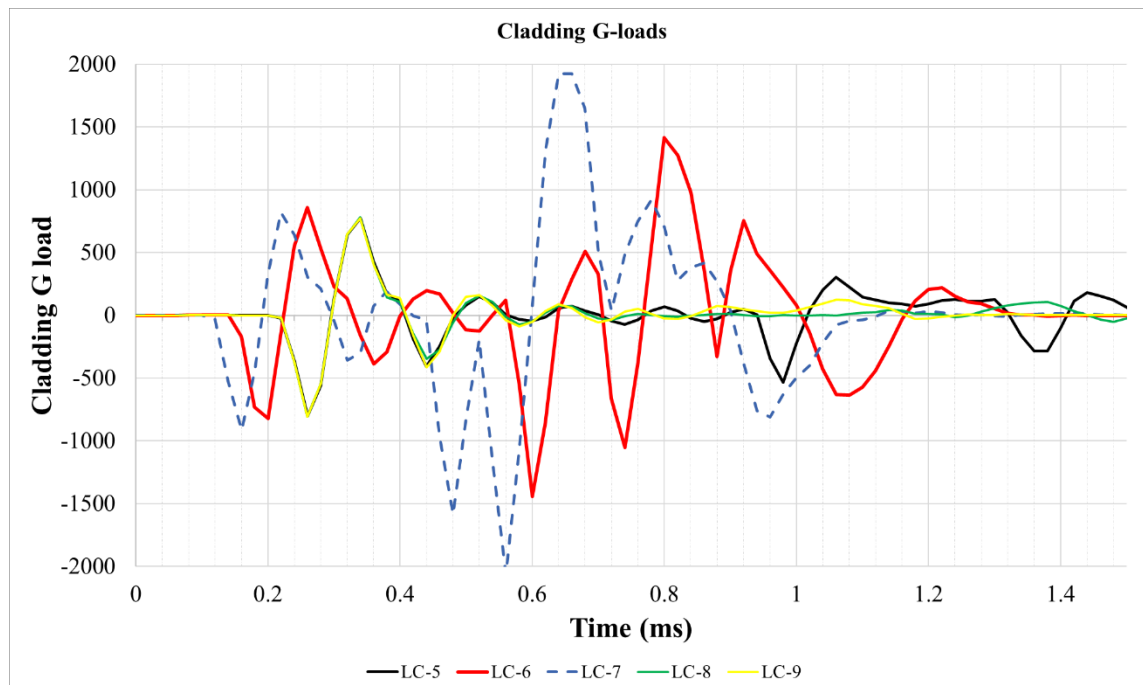


Figure F-70. Impactor end configuration (a) results for load cases 5–9.

**Table F-19. Summary of Fuel Rod Maximum g-Load
During Impact with End Configuration (a)**

Load case	Cladding maximum g-load
LC-1	754
LC-2	1,344
LC-3	2,279
LC-4	3,298
LC-5	774
LC-6	1,414
LC-7	1,925
LC-8	781
LC-9	773

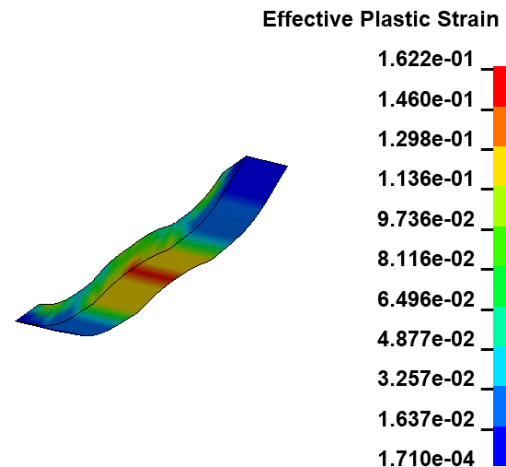


Figure F-71. Plastic strain on the dimples for impactor end configuration (a).

In addition to the permanent deformation of the impactor end dimples, configuration (a) also resulted in large rebound and fluttering of the grid wall portion of the impactor. Because these effects would produce uncontrolled variation in the impacts, this configuration was not appropriate for future cumulative shock testing before fatigue testing in CIRFT.

Based on the FEA, the main reason that the target g-load range cannot be achieved has nothing to do with the impactor itself. Rather, the problem is that the target rod segment is very stiff. To prepare the segment for CIRFT testing, it is necessary to install the heavy dogbone grips on each end. Only 50 mm of segment length is exposed for impact, as shown in Figure F-72. The dogbone provides a very stiff target that does not deflect in bending, so any impact will result in a high g-load, even with very low drop height, low impactor weight, and a soft impactor end configuration such as the dimples with a grid wall. With the dogbone as the target, low g-load impacts are not possible with the current fixture.



Figure F-72. CIRFT dogbone.

F-9.3 Verification of FEA Results Using the Cumulative Effects Fixture

Physical tests using the cumulative effect fixture were completed as a verification of the FEA. A CIRFT dogbone surrogate with stainless-steel cladding and ceramic pellets was constrained in the specimen holder, as shown in Figure F-73. Various impactors with masses ranging from 355 to 47 g were used for the tests. These impactors had end geometries designed to mimic grid dimples, but they were solid, as shown in Figure F-74.

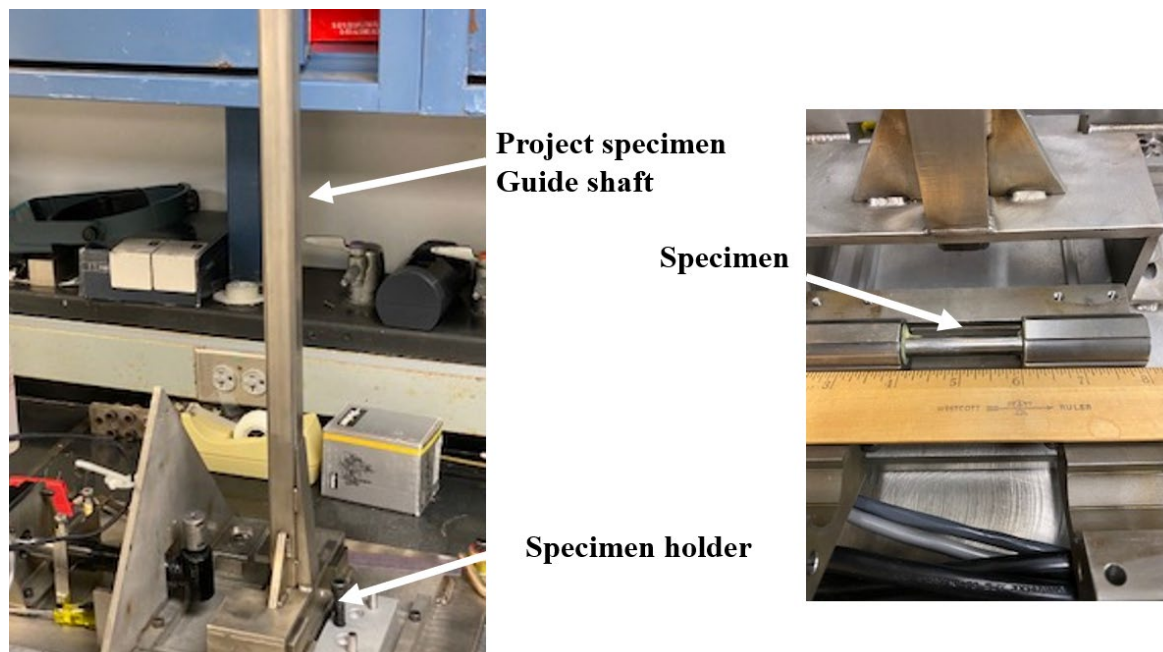


Figure F-73. Physical test configurations with the cumulative effects fixture.



Figure F-74. Impactors used in the physical tests.

To record the maximum g-load on the specimen, a single-axis accelerometer was mounted on the specimen with epoxy adhesive. The maximum recordable load for the accelerometer used is 1,100 g. The 85 g projectile was dropped from two different heights: 127 and 25 mm. The mounted accelerometer on the specimen recorded its maximum acceleration of 1,100 g for all tests, indicating a load greater than 1,100 g for all tests. Some attempts were made to reduce the impact load by adding compliant layers to the impact surfaces, but this was unsuccessful.

F-9.4 Implication of the Multimodal Transportation Test

In parallel to developing this test method, the expected cyclic history for transporting SNF was considered in a shipping test, referred to as the MMTT [F-16]. The MMTT is described in detail in Section F-2.7 [F-12]. The test event considered most relevant to this section is the coupling impact test performed at the Transportation Technology Center, Inc. In this test, an instrumentation car was coupled to the cask car at both standard and above standard speeds that ranged from 2 to 8 mph. The maximum accelerations recorded on the fuel rods in these tests is less than 20 g, and the maximum measured strain on the fuel rods was ~0.01% (or ~100 μ strain). This value is well below the ORNL Fuel Rod Design Fatigue Limit (Figure F-14), indicating that a typical impact should not result in fatigue damage, although the effect of non-zero mean strain has not been completely accounted for in the design limit. Once the effect of non-zero mean strain is fully understood, the effect of potential impacts can be reevaluated, but at this time, the evidence suggests that impacts during transportation will not cause fatigue damage.

F-9.5 Summary, Cumulative Effects Fixture Development

Both FEA and experimental evidence indicate that the current configuration of the drop test is not able to recreate the desired g-loads on the dogbone specimens used in CIRFT fatigue testing. It was concluded that the stiffness of the dogbone specimen results in very high g-loads. No further investigations were completed. In addition, after the FEA was completed, measurements during nearly prototypical transportation tests indicated that the maximum accelerations during a coupling impact event were less than 20 g and the maximum measured strain was ~0.01% (~100 μ strain). This level of strain is likely in the region where fatigue damage is not expected (see Figure F-14), although the effect of non-zero mean strain has not been completely accounted for in the ORNL Fuel Rod Design Fatigue Limit.

REFERENCES

- [F-1]. *High Burnup Dry Storage Cask Research and Development Project: Final Test Plan*, contract no. DE-NE-0000593, Electric Power Research Institute, Palo Alto, California (2014).
- [F-2]. S. Saltzstein et al., *Visualization of the High Burnup Spent Fuel Rod Phase 1 Test Plan*, SAND2018-8042-O (2018).
- [F-3]. R. A. Montgomery et al., *Post-Irradiation Examination Plan for High Burnup Demonstration Project Sister Rods*, SFWD-SFWST-2017-000090 ORNL/SR-2016/708, Oak Ridge National Laboratory (2016).
- [F-4]. J.-A. Wang and H. Wang, *FY 2017 Status Report: CIRFT Data Update and Data Analyses for Spent Nuclear Fuel Vibration Reliability Study, Revision 1*, ORNL/SPR-2017/521, SFWD-SFWST-2017-000030/R1 (2017).
- [F-5]. J.-A. Wang and H. Wang, *Mechanical Fatigue Testing of High Burnup Fuel for Transportation Applications*, NUREG/CR-7198/R1 (2017).
- [F-6]. J.-A. Wang and H. Wang, *Data Processing Package for Cyclic Integrated Reversible Bending Fatigue Testing*, ORNL/TM-2021/2114 (2021).
- [F-7]. J.-A. Wang, H. Wang, H. Jiang, B. Bevard, “High Burnup Spent Nuclear Fuel Transport Reliability Investigation,” *Nuclear Engineering and Design*, 330, 497-515 (2018).
- [F-8]. W. J. O’Donnell and B. F. Langer, “Fatigue Design Basis for Zircaloy Components,” *Nuclear Science and Engineering* 20 (1964): 1–12.
- [F-9]. X. Lin and G. Haicheng, “Low Cycle Fatigue Properties and Microscopic Deformation Structure of Zirc-4 in Recrystallized and Stress-relieved Conditions,” *J. Nucl. Mater.*, 265, 213-217 (1999).
- [F-10]. D. Mowbray, “Effects of 1.0% Superimposed Mean Strain on the Bending Fatigue Strength of Zirc-4,” *Nuclear Applications*, 1:1, 39-48 (1965)
- [F-11]. R. A. Montgomery et al., *Sister Rod Nondestructive Examination Final Report*, SFWD-SFWST-2017-000003 Rev. 1 (M2SF-17OR010201021) / ORNL/SPR-2017/484 Rev. 1 (ORNL/SPR-2018/801), Oak Ridge National Laboratory (2019).
- [F-12]. P. Cantonwine, R. Montgomery, and H. Wang, “Sister Rod Destructive Examinations (FY22) Appendix F2: Evaluation of Fuel Rod Fatigue During Spent Fuel Transportation Conditions,” ORNL/TM-2022/2736 (2022).
- [F-13]. NUREG-2224, “Dry Storage and Transportation of High Burnup Spent Nuclear Fuel,” US NRC, November 2020.
- [F-14]. R. A. Montgomery, “Sister Rod Destructive Examinations (FY21) Appendix G: CIRFT Uncertainty Calculations,” ORNL/SPR-2021/1840, March 31, 2022.
- [F-15]. P. Cantonwine, “Sister Rod Destructive Examinations (FY23) Appendix F3: Uncertainty and Conservative Bias in the Cyclic Integrated Reversible-Bending Fatigue Test,” ORNL/SPR-2023/3006, September 1, 2023.
- [F-16]. E. A. Kalinina et al., *Data Analysis of ENSA/DOE Rail Cask Tests*, SFWD-SFWST-2018-00049/ SAND2018-13258R (2018).
- [F-17]. N. A. Klymynshyn, P. Ivanusa, K. Kadooka, C. Spitz, P. Jensen, S. Ross, B. Hanson, D. Garcia, J. Smith, and S. Lewis. “Modeling and Analysis of the ENSA/DOE Multimodal Transportation Campaign,” PNNL-28088 (2018).

- [F-18]. J.-A. Wang and H. Wang, *Mechanical Fatigue Testing of High Burnup Fuel for Transportation Applications*, NUREG/CR-7198/R1 (2017).
- [F-19]. LS-DYNA. “LS-DYNA.” <http://www.lstc.com/products/ls-dyna>, (9/1/2020).
- [F-20]. ASME BPVC Sec VIII Div. 2 *Annex 3-D Rules for Construction of Nuclear Facility Components*, 2013
- [F-21]. ASME BPVC Sec II, Part D *Rules for Construction of Nuclear Facility Components*, 2013.